DESIGN AND PRODUCTION OF 3D PRINTED BOLUS FOR

ELECTRON RADIATION THERAPY

by

Shiqin Su

Submitted in partial fulfillment of the requirements

for the degree of Master of Science

at

Dalhousie University

Halifax, Nova Scotia

August 2014

Table of Contents

LIST OF TABLES

LIST OF FIGURES

ABSTRACT

This is a proof-of-concept study demonstrating the capacity for modulated electron radiation therapy (MERT) dose distributions using 3D printed bolus. Previous reports have involved bolus design using an electron pencil beam model and fabrication using a milling machine. In this study, an in-house algorithm is presented that optimizes the dose distribution with regard to dose coverage, conformity and homogeneity within the planning target volume (PTV). The algorithm takes advantage of a commercial electron Monte Carlo dose calculation and uses the calculated result as input. Distances along ray lines from the distal side of 90% isodose line to distal surface of the PTV are used to estimate the bolus thickness. Inhomogeneities within the calculation volume are accounted for using the coefficient of equivalent thickness method. Several regional modulation operators are applied to improve the dose coverage and uniformity. The process is iterated (usually twice) until an acceptable MERT plan is realized, and the final bolus is printed using solid polylactic acid. The method is evaluated with regular geometric phantoms, anthropomorphic phantoms and a clinical rhabdomyosarcoma pediatric case. In all cases the dose conformity is improved compared to that with uniform bolus. For geometric phantoms with air or bone inhomogeneities, the dose homogeneity is markedly improved. The actual printed boluses conform well to the surface of complex anthropomorphic phantoms. The correspondence of the dose distribution between the calculated synthetic bolus and the actual manufactured bolus is shown. For the rhabdomyosarcoma patient, the MERT plan yields a reduction of mean dose by 38.2% in left kidney relative to uniform bolus. MERT using 3D printed bolus appears to be a practical, low cost approach to generating optimized bolus for electron

therapy. The method is effective in improving conformity of the prescription isodose surface and in sparing immediately adjacent normal tissues.

LIST OF ABBREVIATIONS AND SYMBOLS USED

2D	Two-dimensional
3D	Three-dimensional
BCC	Basal cell carcinoma
CET	Coefficient of equivalent thickness
CI	Conformity index
CM	Component Module
CPE	Charged particle equilibrium
CSDA	Continuously slowing down approximation
CT	Computed tomography
CTV	Clinical target volume
D_{50}	50% of maximum dose
D_{90}	90% of maximum dose
DICOM	Digital imaging and communication in medicine
d_{max}	Depth of maximum PDD
D_{max}	Maximum dose
DVH	Dose-volume histogram
ECT	Electron conformal therapy
ECUT	Electron energy cut-off
EGS	Electron gamma shower
eMC	Electron Monte Carlo
eMLC	Electron multi-leaf collimator
FLEC	Few-leaf electron collimator

GTV	Gross tumour volume
HDR	High dose rate
HU	Hounsfield Unit
ICRU	International Commission on Radiation Units and Measurements
IMET	Intensity-modulated electron therapy
IMRT	Intensity modulation radiation therapy
IPS	Initial Phase Space model
ITV	Internal target volume
LDR	Low dose rate
LET	Linear energy transfer
linac	Linear accelerator
MC	Monte Carlo
MERT	Modulated electron radiation therapy
MeV	Mega electron volt
MLC	Multi-leaf collimator
MMC	Macro Monte Carlo
MOSFET	Metal–oxide–semiconductor field-effect transistor
MRI	Magnetic resonance imaging
MU	Monitor unit
MV	Megavoltage
NIST	National Institute of Standards and Technology
NTCP	Normal tissue complication probability
OAR	Organ at risk
PCUT	Photon energy cut-off parameters

PDD	Percentage depth dose
PDF	Probability distribution function
PDI	Percentage depth-ionization
PDR	Pulsed dose rate
PET	Positron emission tomography
PLA	Polylactic acid
pMLC	Photon multi-leaf collimator
PRV	Planning organ at risk volume
PTV	Planning target volume
QA	Quality assurance
R_{50}	Depth of 50% PDD
R_{90}	Depth of 90% PDD
RF	Radiofrequency
R_P	Practical range
RT	Radiotherapy
SBT	Shift of bolus thickness
SSD	Source-to-surface distance
SSD_{eff}	Effective SSD
STL	Stereolithography
TCP	Tumour control probability
TSET	Total skin electron therapy
Z	Atomic number
Z_{eff}	Effective atomic number

ACKNOWLEDGEMENTS

Chapter 1 INTRODUCTION

1.1 Cancer Treatment with Radiation

Cancer is a class of diseases characterized by unregulated cell growth, which harms the body when damaged cells divide uncontrollably to form masses of tissue called tumours. Tumours can grow and interfere with the digestive, nervous, and circulatory systems and they can release hormones that alter body function. Tumours that do not invade neighboring tissues and demonstrate limited growth are generally considered to be benign, while malignant cancer is any type of cancer that spreads to other parts of the body. There are over 200 different types of cancer, and each is classified by the type of cell that is initially affected. According to Canadian Cancer Statistics 2013, almost half of all Canadians (41% of females and 46% of males) will develop cancer in their lifetime and a quarter of all Canadians are expected to die of the disease[1].

Surgery, chemotherapy and radiation therapy have all been proven to effectively treat cancer, and thus extend life or improve quality of life. The type of treatment or the order of treatment will be different for individual patients, depending on the location of the tumour and the stage of the disease at diagnosis.

Among all the cancer treatment, 50% patient may receive radiation therapy before, during, or after surgery[2]. Radiation therapy uses high-energy radiation to kill cancer cells by damaging their DNA, thereby killing them or preventing their replication. X-rays, gamma rays and charged particles are types of radiation used for cancer treatment. However, radiation therapy can damage normal cells as well as cancer cells; therefore, treatment must be planned and delivered accurately with regard to both spatial

and dosimetric accuracy in order to minimize side effects. The principle of radiation therapy is usually illustrated by plotting two curves (Figure 1.1), one for the tumour control probability (TCP) (curve A) and the other for the normal tissue complication probability (NTCP) (curve B), where the optimum choice in the treatment of a given tumour is to maximize the TCP and simultaneously minimize the NTCP. The effectiveness of radiation damage to cancerous tissues is correlated to the amount of energy absorbed per unit mass of tissue or absorbed dose. The international standard unit for dose is the Gray (Gy), where 1 Gy = 1 J/kg. The tumour lethal dose required to achieve tumour control depends on the volume and localization of the target, radiosensitivity as well as type of tumour, which also determines the type of treatment chosen.
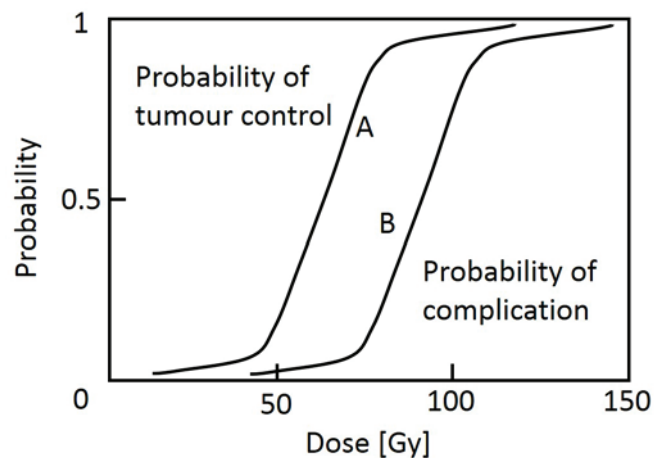
Figure 1.1 Representation of TCP (curve A) and NTCP (curve B)

1.1.1 Types of radiation therapies

The radiation used for cancer treatment may be produced by a machine outside the body (external beam radiation therapy), or it may be emitted by radioactive material placed in the body through body cavities, surgical implant, or injection into the bloodstream (brachytherapy).

2

In external beam radiation therapy, the patient lies on a couch and an external source of radiation is directed to the tumour volume from outside the body. Photon and electron beams are the most widely used sources for external beam radiotherapy, however a comparatively small number of cancer centers offer radiation therapy using proton sources. Photon and electron radiation therapy are normally delivered by a clinical linear accelerator (linac) producing beams in the range of 4-25 MeV[3] (discussed in section 1.1.2).

Radiation treatment using brachytherapy ('brachys' is the Greek for short-distance) is delivered from radiation sources placed inside or on the body. Several brachytherapy techniques are used in cancer treatment: interstitial brachytherapy uses a radiation source placed permanently within tumour tissue, such as within a prostate tumour; intracavitary brachytherapy uses a source placed temporarily within a surgical cavity or a body cavity, such as the chest cavity, near a tumour. While permanent implants generally emit low energy radiation, temporary implants are performed with a high dose rate, with which the treatments last only a few minutes. There are three distinct types of remote afterloading devices: low dose rate (LDR) (20-30 mCi), high dose rate (HDR) (3-10 Ci) and pulsed dose rate (PDR) (1-2 Ci). The three commonly used radioactive sources in remote afterloading devices are ^{60}Co, ^{137}Cs and ^{192}Ir.[3]

1.1.2 Beam generation in a linear accelerator

The most commonly used treatment machine for external beam therapy is the linac, which uses high-frequency electromagnetic waves to accelerate electrons through a waveguide. The high-energy electron beam itself can be used for treatment, usually of superficial tumours, or it can be made to strike a target to produce x-rays for treating

deep tumours. The main operating components of a medical linac are shown in Figure 1.2: (1) injection system; (2) microwave generator; (3) accelerating waveguide; (4) auxiliary system; (5) beam transport system and (6) beam collimation and monitoring system (treatment head). A typical modern high energy linac provides multiple photon energies (6 and 18 MV) and several electron energies (6, 9, 12 and 16 MeV) for clinical uses.

The injection system is the source of electrons, which includes a simple electrostatic accelerator referred as an electron gun. In a Varian linac system, a triode type electron gun is employed, containing a heated filament cathode, a perforated grounded anode and a grid. Electrons are thermionically emitted from the heated cathode, focused into a pencil beam by a curved focusing electrode and accelerated towards the perforated anode through which they drift to enter the accelerating waveguide. The timing of the injection of electrons into the accelerating waveguide is controlled by voltage pulses, which are applied to the grid and must be synchronized with the pulses applied to the microwave generator (i.e. radiofrequency (RF) system). The RF power generation system produces the microwave radiation used in the accelerating waveguide to accelerate electrons to the desired kinetic energy by either magnetron or klystron. While magnetron usually applied in lower energy linacs (4-8 MeV), the klystron acts as an RF power amplifier and is commonly used in higher energy linacs.
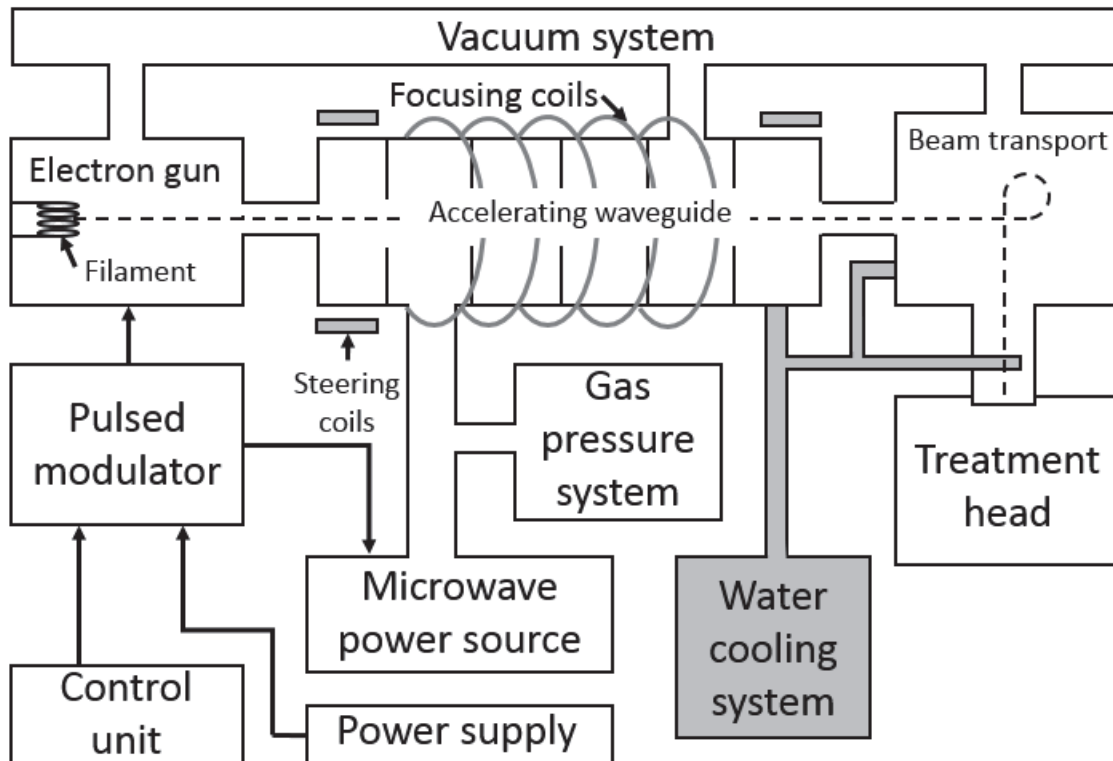
Figure 1.2 A diagram of typical medical linear accelerator adapted from *Radiation Oncology Physics: A Handbook for Teachers and Students*[3]

The waveguides are evacuated structures of rectangular or circular cross section used in transmission of microwaves. The propagation of microwaves through waveguides is governed by Maxwell's equations and boundary conditions at the metallic walls. The accelerating waveguide is evacuated to allow free propagation of electrons. A standing waveguide structure is used in the Varian linac, in which every second cavity carries no electric field and thus produces no energy gain for the electron. These cavities serve only as coupling cavities and can be moved out to the side of waveguide structure, effectively shortening the accelerating waveguide by 50%.

As the high-energy electrons emerge from the exit window of the waveguide, they are in the form of a pencil beam of about 3 mm in diameter. In high energy linac, the waveguide is usually long and therefore, is placed parallel to the gantry rotation axis,

which accelerates electrons in a direction perpendicular to that required for incidence on the patient. The electrons are therefore steered through the required angle, usually 270 degrees by an achromatic bending magnet.
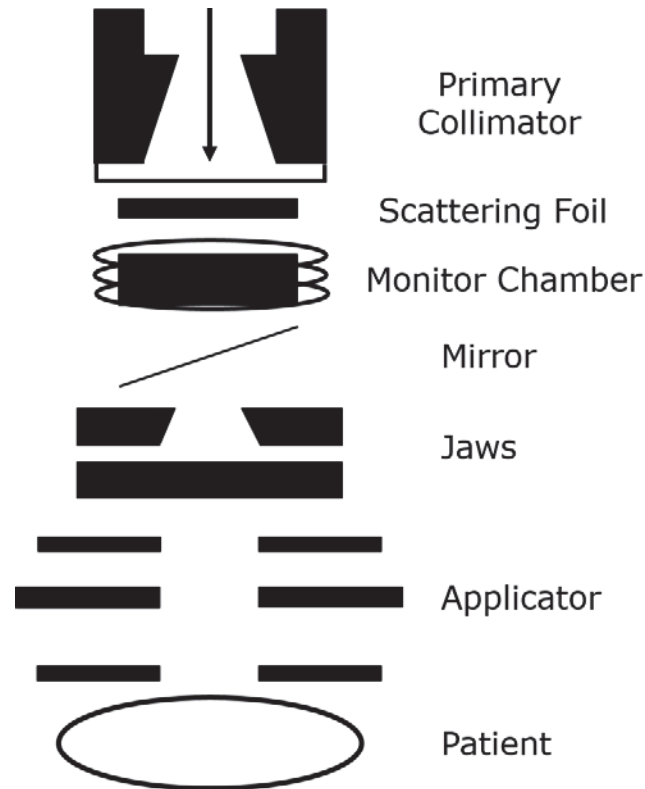
Figure 1.3 Illustration of treatment head in electron mode

The linac treatment head contains the required components for production, monitoring and shaping of the clinical photon and electron beams. The most important components in a treatment head are primary collimator, jaws, ionization chamber, multi-leaf collimator (MLC), x-ray target and flattening filter for photon mode, or scattering foil for electron mode. Special cones and applicators are also used to collimate the electron beams. The primary collimator defines a maximum field (40×40 cm^2 at isocenter), which is then further truncated by two pairs of movable collimators, i.e. jaws. The monitor chambers are included to monitor the beam output (monitor unit, MU)

during the treatment, where 1 MU corresponds to 1 cGy in a water phantom under the calibration setup.

In the photon beam mode, x-rays are produced when the electrons are incident on a target of a high-Z material such as tungsten and flattened with a flattening filter that attenuates the central part of the raw beams to levels equal to those on the periphery. In the electron beam mode, on the other hand, both the target and the flattening filter of the photon beam mode are removed. The beam exits the primary collimator, instead of striking the target, is made to strike an electron scattering foil to spread the beam as well as get uniform electron fluence across the treatment field. The scattering foil is usually made of high-Z material (copper or lead) and is sufficiently thick to produce the desired scattering, while as thin as possible to minimize the undesirable radiative losses. A typical energy fluence spectrum of clinical electron beam (6 MeV) is shown in Figure 1.4.
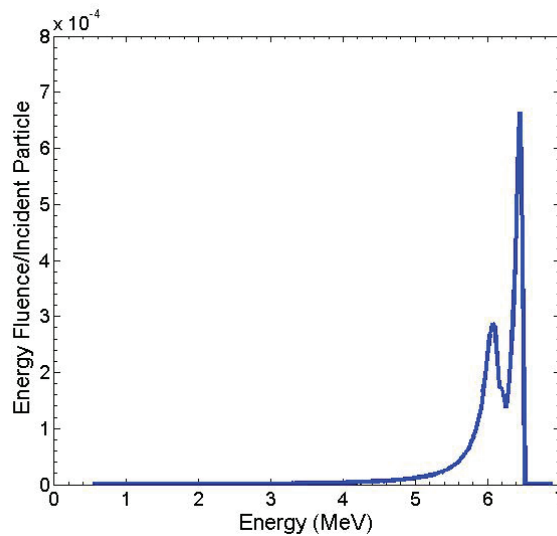
Figure 1.4 A typical energy fluence spectrum of clinical 6 MeV electron beam generated using EGSnrc.

1.1.3 Treatment Planning

In radiation therapy, treatment planning is the process in which a team consisting of radiation oncologists, medical physicists and medical dosimetrists plan the appropriate external beam radiotherapy or internal brachytherapy treatment technique for a patient with cancer, with the goal of delivering a sufficient and appropriate dose to the tumour volume while maximizing the sparing of surrounding and uninvolved organs and tissues. During the process, treatment simulations are used to plan the geometric, radiological, and dosimetric aspects of the therapy using treatment planning system, involving the delineation of the organ at risks (OARs) and PTV as well as the selection of the appropriate beam energy and arrangements. During simulation, multiple medical imaging modalities may be used in order to develop a detailed three-dimensional (3D) model of the patient, including the tumour volume and surrounding anatomy. Of all the modalities, computed tomography (CT) scans are most often used, but magnetic resonance imaging (MRI), positron emission tomography (PET) and ultrasound scans can also be included to provide soft tissue discrimination (MRI) or functional information, e.g., metabolism (PET).
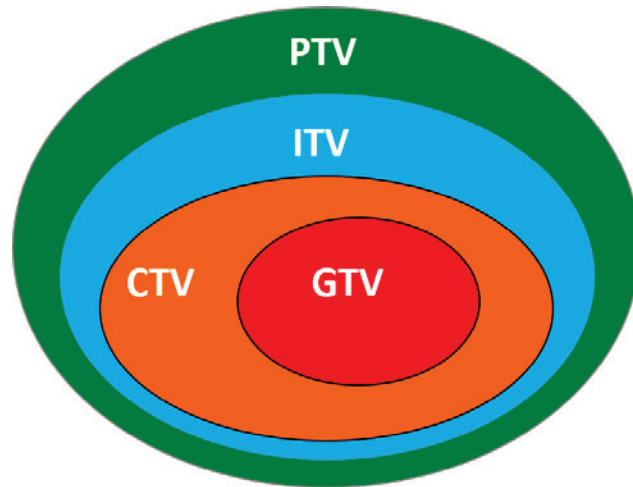
Figure 1.5 Graphical representation of the volumes of interest, as defined in ICRU Reports No. 50[4] and 62[5]

Medical imaging allows for the accurate identification and delineation of the target volumes and critical structures. The delineation is the prerequisite for 3D treatment planning. Several volumes related to 3D treatment planning have been defined according to ICRU Reports No. 50[4] and 62[5] and are summarized in Table 1.1:

Table 1.1 Definition of various volumes of interest

Gross tumour volume (GTV)	Gross palpable or visible extent and location of malignant growth
Clinical target volume (CTV)	Volume that contains a GTV and/or sub-clinical microscopic malignant disease
Internal target volume (ITV)	Volume that consists of the CTV plus an internal margin
Planning target volume (PTV)	Volume that involves setup margins to ensure adequate dose delivery to all part of CTV
Planning organ at risk volume (PRV)	Volume that compensates for setup errors to ensure the sparing of OARs

The radiation beam is shaped to fit the projection of the target from a beam's eye view (BEV) according to the prescribed dose given by the oncologists. For photon therapy, the shaping is accomplished using a MLC to control beam weighting, while for electron therapy, appropriate applicator and aperture are selected. The radiation dose is

9

calculated in three dimensions using a dose-calculation algorithm that accounts for the divergence of the beam and heterogeneity in all directions. The plans are usually assessed with the aid of dose-volume histograms (DVH), which is a graphical representation of the dose received by normal tissues and target volumes within a 3-D radiation therapy plan. A DVH provides quantitative information with regard to the dose absorbed in the volume and summarizes the entire dose distribution into a single curve for each anatomic structure of interest, thus allowing the clinician to evaluate the uniformity of the dose to the diseased tissue (tumour) and sparing of healthy structures.

Several metrics are used in the evaluation of dose distribution, including dose conformity (conformity index (CI)), dose homogeneity and dose fall-off. Conformity index is defined as the ratio of prescription isodose surface volume to the tumour volume:

$$Conformity\ index = \frac{Prescription\ isodose}{tumour\ volume} \qquad \text{Eq. 1.1}$$

Dose homogeneity describes the variation of dose across the target volume, which is given by D5%-D95%, i.e. the difference in dose values corresponding to 5% volume and 95% volume. The rate of fall-off of dose outside of the target volume is usually dictated by difference in 80% and 20% isodose.

1.2 Electron Beam Radiation Therapy

About 10% cancer patients receive electron radiation therapy in Nova Scotia Cancer Center. Megavoltage electron beams have been used in radiotherapy since the introduction of betatrons and linear accelerators in the 1950s. A typical two dimensional (2D) dose distribution of electron beam is shown in Figure 1.6, where the lateral constriction of the higher isodose levels (>80%) and the broadening of the low isodose levels (<20%) can be observed. Compared to photon beams, electron beams have the

following depth dose characteristics of these beams (Figure 1.7): (1) high surface dose compared to the maximum dose with depth; (2) increased dose homogeneity in the buildup region; (3) sharper dose fall-off beyond the depth of dose maximum d_{max}, and therefore they are most commonly used in the treatment of superficial tumours such as skin, lip, ear lesions, as well as for irradiation of the chest wall following radical mastectomy. Electron beam therapy is also used for head and neck tumours, boost treatment for breast and in total skin electron therapy (TSET).
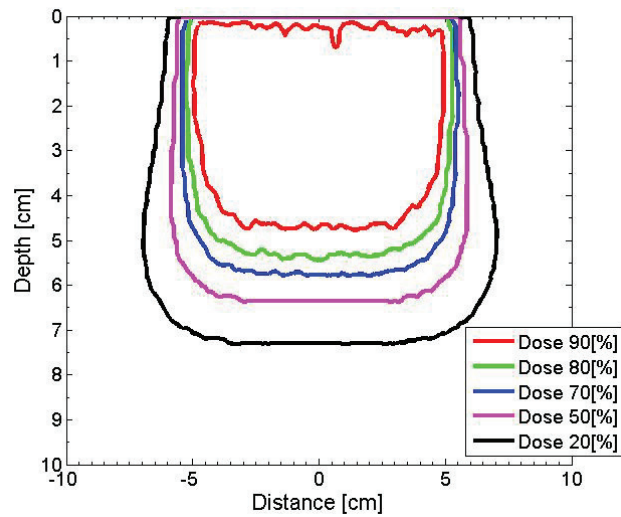
Figure 1.6 Isodose plot of 16 MeV (right) electron beam with 10×10 cm^2 field size in water generated using Eclipse eMC. Dose is normalized to $d_{max} = 3.00$ cm.

While photon beam therapy usually involves multiple intersecting beams, electron beam therapy normally requires a single treatment field with cross-sectional dimensions and energy selected to ensure that the PTV is covered by the prescribed dose level. In combination with a conformal cut-out size and a bolus of uniform thickness, a superficial tumour volume can be adequately covered with a dose typically within ±10%.
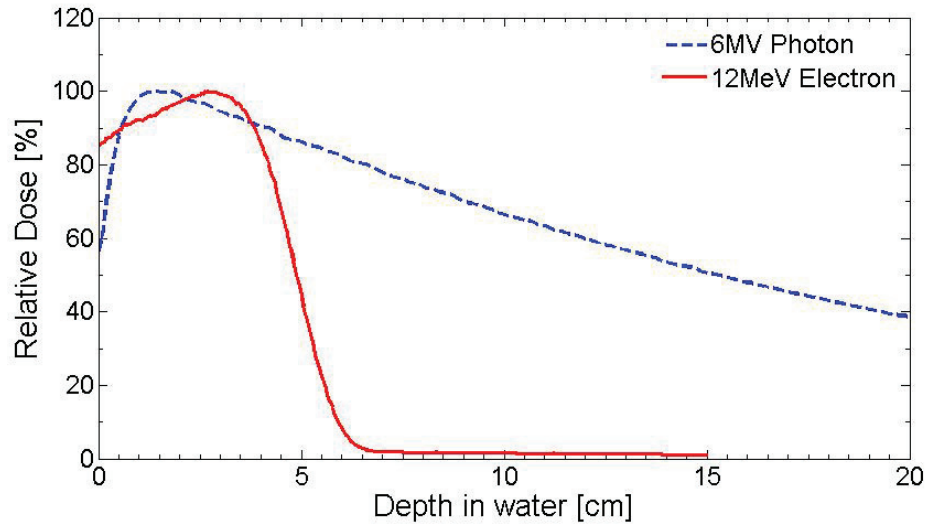
Figure 1.7 Central axis percentage depth dose curve of 6 MV photon beam and 12 MeV electron beam

1.2.1 Use of bolus in electron therapy

1.2.1.1 Functions of bolus

Bolus is an essential component in the delivery of optimal electron beam therapy and is used clinically for the following reason: i) to deliver sufficient surface dose without unduly increasing dose to more distal volumes (Figure 1.8); ii) to precisely control the depth of the prescription isodose surface for a given electron energy; or iii) to simplify complex patient surfaces in order to generate an more predictable dose distribution. Ideally, the bolus material should be equivalent to tissue in stopping power and scattering power so that the dose distribution will not be affected by the presence of bolus. In practice, bolus is formed from a nearly tissue equivalent material such as wax, wet gauze or thermoplastic sheets. It is normally placed in direct contact with the patient's skin and is manufactured to conform as closely as possible to the skin surface. Usually, the thickness of the bolus is made to be approximately uniform during manual fabrication, or is moulded to create a flat surface which will be normal to beam incidence

12

during treatment. While this produces a dose distribution similar to Figure 1.6, in concept it is possible to design the bolus to achieve dose conformity to even complex PTVs, which forms a major focus of this work (discussed further in section 1.4 below).
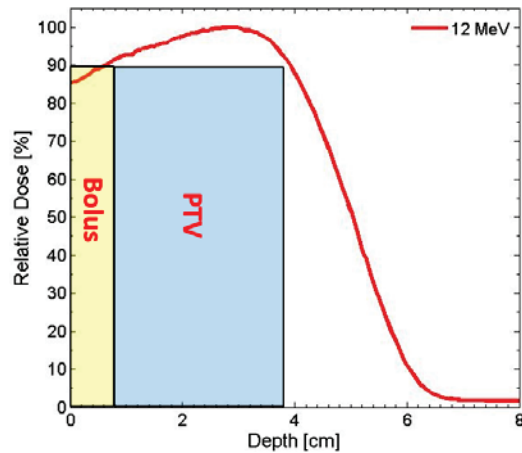
Figure 1.8 An example of bolus increasing the surface dose. With the bolus added, PTV can receive a higher dose (90% of prescribed dose).

1.2.1.2 Limitations of bolus

Current practice with regard to the use of bolus in electron therapy is limited in several respects. First, despite the fact that the 3D surface of the patient may be known with sub-millimeter precision, i.e., from pre-acquired CT image data, the precision and accuracy of bolus fabrication is limited by the manual process and the expertise of the practitioner. Secondly, the capacity of a prefabricated bolus sheet to conform to irregular surfaces is limited, resulting in air gaps between the bolus and patient surface (Figure 1.9). These air gaps, in turn, can result in substantial inaccuracies in delivered surface dose, for example, exceeding 10%[6] (discussed further in section 2.7.2 below) and thus care must be taken each day to apply the bolus for each treatment without air gaps, and maintaining consistency. In practice, this often prompts filling of air gaps with wet gauze,

however the variability in water-equivalence of the gauze causes day-to-day variation in the dose delivered to the patient.
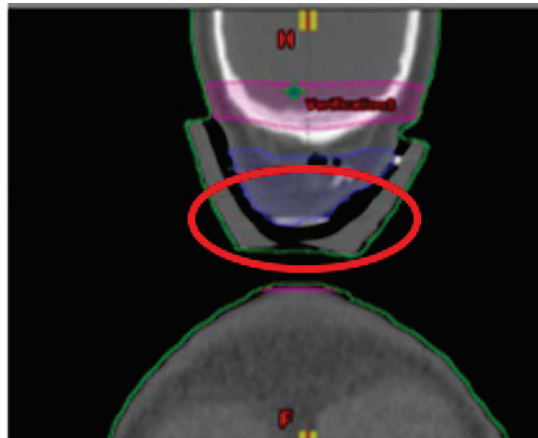
Figure 1.9 Illustration of air gaps (highlighted by red circle) between the bolus and patient surface

Thirdly, there often exist limitations with regard to the similarity of the bolus used in treatment planning, and that applied during treatment delivery, which may result in a significant and systematic error. Bolus is commonly pre-defined in the planning system, e.g., as a unit-density local expansion of the surface of the patient over a defined region, and fabricated thereafter. In this case, the similarity of the planned and fabricated bolus is often limited with regard to both thickness and curvature, particularly in the presence of steep, complex or curved surfaces. The wax or thermoplastic bolus fabrication can be time consuming and cumbersome. The patient must be present for the procedure, as well as multiple practitioners, e.g., radiation oncologists and radiation therapists and medical physicists which increases the overall cost of the procedure. Bolus fabrication is often performed in CT simulation suite, which increases the demand on this facility in the clinic.

1.3 Modulated Electron Radiation Therapy (MERT)

During the treatment planning process, the shape of the electron aperture, the beam angle relative to the surface, and the beam energy are selected to provide dose coverage at the surface as well as at the deep aspect of the PTV by a high isodose (typically 80%-90% of the maximum dose). However, the dose conformity at the distal surface of the target volume is often poor (Figure 1.10), since the planning and delivery process does not modulate the electron fluence or energy. Consequently, electron therapy often delivers an unnecessarily high dose to immediately underlying critical structures and tissues (e.g. left kidney in Figure 1.10). In addition, other than specifying the covering isodose surface as part of the prescription, the dose homogeneity in the target volume is not explicitly controlled during the planning process. Improved plan quality can be achieved using "modulated electron radiation therapy" (MERT) [7-30]. MERT can be accomplished by sophisticated techniques based on modulation of multiple electron energies and inverse treatment planning of electron beam weights or intensities, which is further classified into two categories: segmented-field electron conformal therapy (ECT) and intensity-modulated electron therapy (IMET). The strengths and weaknesses of each approach are concluded in Table 1.2.
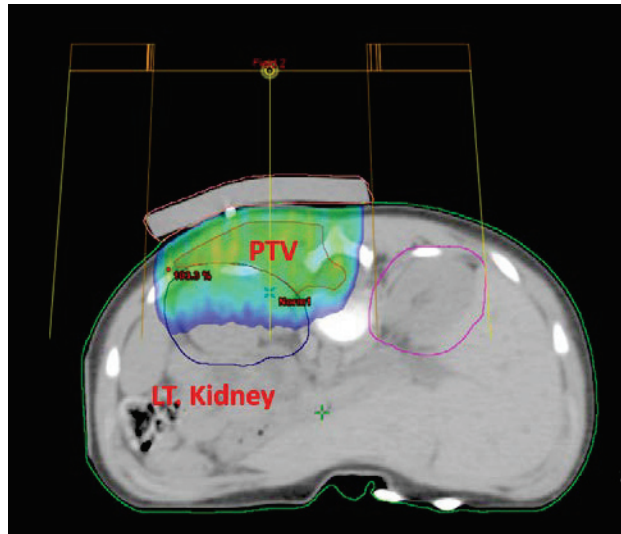
Figure 1.10 Illustration of poor conformity, where OAR (left kidney) receives a high dose (90% prescribed isodose)

Segmented-field ECT uses multiple electron treatment fields, each with its specific energy and beam weight, to achieve dose uniformity in the PTV[8]. The method gained the advantage of using the already existed photon MLC (pMLC) to modulate the intensity of electron beam and was able to improve the conformity for target close to the surface. The results, however, were dismal due to the wide penumbra associated with clinical electron beams scattered from foils[8]. The penumbra could be narrowed by filling the treatment head with helium[9, 10] or by decreasing the source-to-surface distance (SSD) to less than 100 cm (e.g. 70 cm). Despite the advantage gained by use of pMLC, this technique was limited by the delivery complexity and the number of segments (fields) required[8].

IMET is similar, in concept, to inverse treatment planning (or optimization) of intensity modulated radiotherapy (IMRT) and uses multiple, optimally-weighted beamlets of both photons and electrons[16] to deliver dose conformal to the PTV[13]. Beamlets are shaped by either a pMLC, specific add-on electron multi-leaf collimator (eMLC) with thin-leaves, or few-leaf electron collimator (FLEC). For IMET using

pMLC, in-house Monte Carlo (MC) based inverse treatment planning system was developed. The results of the MC simulation, which were verified through measurement, indicated that the use of existing pMLC to modulate electron beams was feasible[11-14] even though it had the same penumbra issue as segmented-field ECT. However, the collimators resulted in unnecessary bremsstrahlung dose for high energy beam and low output and degraded beam profile for low energy beam, and thus a minimum field size (2×2 cm^2) is recommanded[11].

Table 1.2 Comparison of different MERT approaches

Technique	Collimator	Strengths	Limitations
Segmented-field ECT	pMLC[8-12]	A	B, D, F, I
IMET	pMLC[11-16]	A, K	D, E, F, I
	eMLC[17-22]	A, L	B, C, J
	FLEC[23,24]	A, H, L	B, C
Bolus ECT	Bolus[25-30]	A, L	G

A. Improved dose conformity observed

B. Complex delivery

C. Add-on electron MLC

D. Reduced SSD required

E. Minimum field size required

F. Helium filled treatment head required

G. Transportation of bolus required

H. Scattering foils free beam available

I. Unnecessary bremsstrahlung dose

J. Restrained flexibility of variable field openings

K. Combination of photon and electron beam

L. Minimized electron scatter in air

Various prototypes of thin-leaf eMLC had been manufactured by different groups[17-22], which were usually mounted on the bottom scraper of the applicator. These add-on eMLCs were able to collimate the electron beam as well as minimize the electron scatter in air. However, this approach required the presence of a large number of motors at the bottom of the electron applicator, which restrained the flexibility of variable field openings[23]. In an attempt to facilitate automated collimation, another type of eMLC, i.e.

FLEC[23] was designed, which consisted of four blades. The method was further enhanced with scattering foil free beam to reduce the bremsstrahlung dose[24]. Nevertheless, though these MERT techniques with add-on eMLC show promising results in terms of PTV coverage and normal tissue sparing, they are complex in clinical implementation and dose delivery, thus compromising the efficiency of treatment.

An alternative approach involves a bolus with modulated thickness. For MERT using bolus (bolus ECT), bolus thickness is optimized by considering the shape of the PTV and the range of electron beam. As a result, a customized prescription isodose surface can be produced within the patient. Modulation of the bolus thickness improves the conformity of the dose to the PTV by depth and therefore minimizes the dose delivered to the normal tissues. Comparison between conventional uniform bolus and modulated bolus affecting the dose distribution is shown in Figure 1.11. An effective bolus design algorithm based on an electron pencil beam model was presented by Low *et al*[25], with which the proximal side of bolus was generated by several operators while the geometry of patient side of bolus was based on the CT images of the patient. Using this algorithm, excellent dose conformity was shown for several cases for bolus produced by a milling machine[26-30]. However, since the pencil beam calculation is limited in the presence of inhomogeneities or highly irregular patient surfaces, the resulting dose distributions may lack dosimetric accuracy (discussed further in section 2.7.1). Compared to other MERT approaches, the method gained the advantage of simplicity in beam delivery. As a result, bolus ECT had already been commercialized by Decimal[©] and been applied in the clinical treatment in several cancer centers. Better fitting of the bolus to the patients was proved, attributing to the high resolution (i.e. in the order of 0.1 mm) of milling machine used in the method. The process, nevertheless, involves the

transportation of the bolus from the external manufacturer to the hospital and therefore the use of bolus ECT is limited by the distance to the bolus manufacturer.
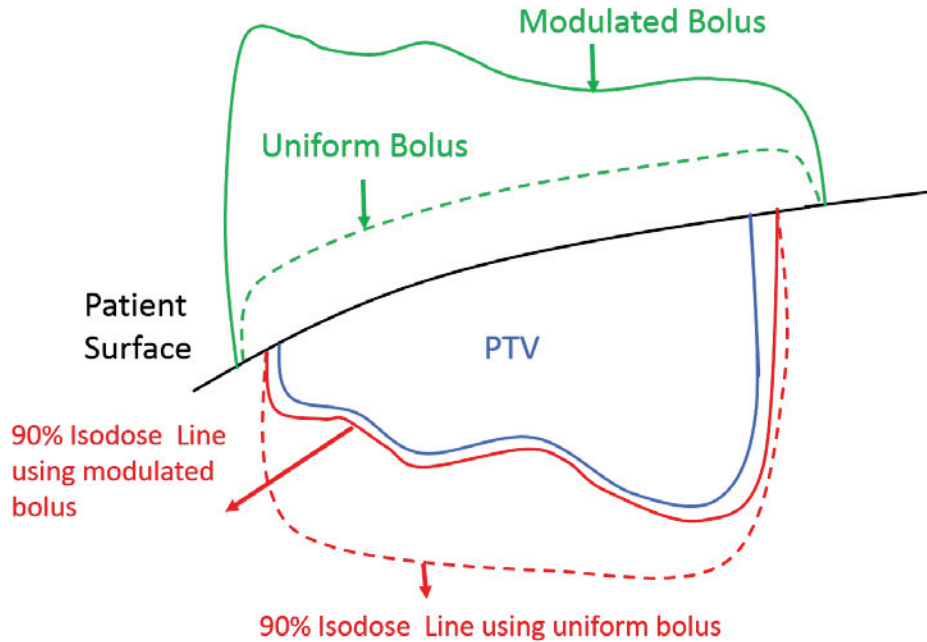
Figure 1.11 Effect of modulated bolus compared to uniform bolus

1.4 Research Goals

The main goal of this project is to develop a methodology that results in improved quality of delivered dose distributions, particularly with regard to dose conformity to the PTV. The approach should offer higher accuracy with regard to modeling of delivered dose compared to present techniques. Finally, the method should offer practical advantages with regard to efficient use of time and resources.

We present an algorithm for bolus design, starting with an initial dose distribution for uniform bolus calculated by electron Monte Carlo (eMC, Varian Medical Systems, Inc.). The bolus is fabricated using the 3D printing technique, which is a relatively new fabrication process that uses a stereolithography (STL) model as input to create a 3D physical model by applying many successive layers of a polylactic acid (PLA) material

at a typical resolution of 0.1 mm. Both physical and dosimetric characterizations of the PLA are performed through measurement. We examine the efficacy of the approach for regular, geometric phantoms as well as realistic patient cases. Finally, we assess the accuracy of corresponding dose distributions based on the idealized, calculated bolus and that resulting from the actual manufactured bolus with the assistance of planning system and the measurements.

Chapter 2 PHYSICS OF ELECTRON BEAM THERAPY

In this chapter, both physical and clinical aspects of electron beams will be discussed. Energy loss through inelastic collision and scattering through elastic collision will be introduced[31, 32]. The clinical aspects of electron beams will be highlighted, including the depth and lateral dose distribution, dose measurement and algorithm for dose calculation[3].

2.1 Interactions of Electrons with Matter

As an energetic electron traverses through matter, it interacts through Coulomb interactions with atomic orbital electrons and atomic nuclei. The collisions between the incident electron and an orbital electron or nucleus of an atom may be elastic or inelastic. In an inelastic collision the electron is deflected from its original path and some of its kinetic energy is transferred to an orbital electron (collisional losses) or emitted in the form of bremsstrahlung (radiative losses). In an elastic collision the electron is deflected from its original path but no energy loss occurs (scattering). The electron scattering will be discussed in section 2.4.

Energy loss mechanisms are of special interest to radiation therapy as the basis for calculation of absorbed dose or energy deposited in a medium irradiated by a high energy electron beam. The type of interaction that occurs, and the consequence with regard to energy loss, can be characterized in terms of the relative size of the atomic radius *a* compared to the impact parameter *b* of the interaction as illustrated in Figure 2.1. The impact parameter is defined as the perpendicular distance between the electron direction before the interaction and the atomic nucleus.

The typical energy loss for a therapy electron beam, averaged over its entire range, is about 2 MeV/cm in water and water-like tissues[3].
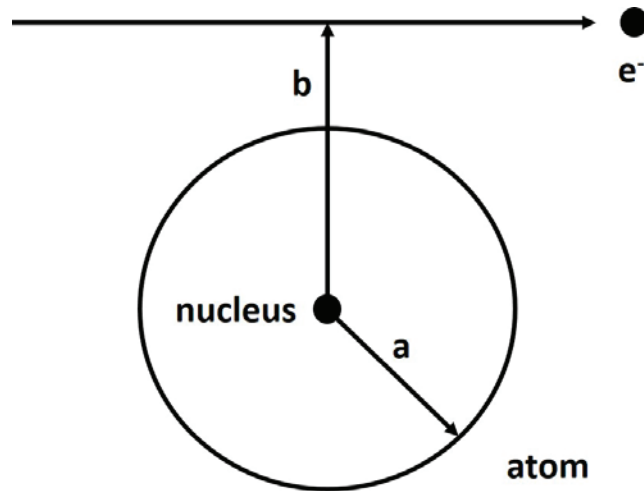
Figure 2.1 Interation of an electron with an atom, where *a* is classical atomic radius and *b* is the classical impact parameter

2.1.1 Soft interactions (*b* >> *a*)

When an electron passes an atom at a considerable distance (*b* >> *a*), the influence of the particle's Coulomb force field affects the atom as a whole. As a result of such collision, one or more orbital electrons experience a transition to an excited state or to an unbound state. The energy requirements for the occurrence of the two processes are determined by the binding energy of electron (in the order of eV) and hence only a small amount of energy is transferred from the incident electron to the medium. These atomic excitations and ionizations lead to collisional energy losses and are characterized by collision stopping powers. Because of larger probability than hitting on the individual atoms, soft collisions are the most frequent charged particle interactions, accounting for roughly half of the energy transferred to the absorber medium[31].

2.1.2 Hard interactions (*b ≈ a*)

When the impact parameter is of the order of the atomic radius ($b \approx a$), the incident electron will undergo a hard collision with an orbital electron which is then ejected from the atom. If the kinetic energy acquired by the ejected electron is large enough for it to cause further ionization (i.e. in the order of 1 keV or more[32]), the electron is called a secondary electron or a delta ray (δ-ray). These particles produce secondary ionization as they lose energy in the medium, and a δ-ray dissipates its kinetic energy along a separate track (called a "spur") from that of the primary charged particle. In hard collision processes with orbital electrons, an appreciable fraction of the electron's kinetic energy will be transferred to the orbital electrons. Although hard collisions are few in number compared to soft collisions, the total fraction of primary particles' energy lost through two processes are comparable.

2.1.3 Radiative interactions (*b << a*)

When the impact parameter of a charged particle is much smaller than the atomic radius, the Coulomb-force interaction takes place mainly with the nucleus. In all but 2-3% of electron interactions with nucleus, the electron is scattered elastically and does not emit an x-ray photon or excite the nucleus (elastic collision). Such interaction will be discussed in section 2.4.1.

In the other 2-3% of the cases in which the incident electron undergoes an interaction (collision) with the atomic nucleus, an inelastic radiative interaction occurs in which a bremsstrahlung (German for "braking rays") photon is emitted. The emitted photon will have a maximum energy equal to the kinetic energy of the incident electron. The energy of the emitted bremsstrahlung photon depends on the magnitude of the

impact parameter *b*, where the smaller the impact parameter, the higher the energy of the bremsstrahlung photon. The electron is not only deflected in this process, but gives a significant fraction (up to 100%) of its kinetic energy to the photon, slowing down in the process. Bremsstrahlung photons comprise the majority of the energy spectrum produced in the photon target of a linear accelerator and most x-ray tubes used in radiography.

Although bremsstrahlung production is an important means of energy dissipation by energetic electrons in high-*Z* media, such as lead, it is relatively insignificant in low-*Z* (tissue-equivalent) materials for electrons below 10 MeV. Not only is the production cross section low in that case, but the resulting photons are penetrating enough so that most of them can escape from objects several centimeters in size. Thus they usually carry away their quantum energy rather than expending it in the medium through a further interaction.

2.2 Stopping Power

The expectation value of the rate of energy loss per unit of path length *l* by a charged particle with energy *T* in a medium is called its linear stopping power. Dividing the linear stopping power by the density ρ of the absorbing medium results in the mass stopping power ($dT/\rho\,dl$), expressed with of MeV cm^2/g. Mass stopping power may be subdivided into 'collision stopping power' and 'radiative stopping power':

$$\left(\frac{dT}{\rho dl}\right)_{total} = \left(\frac{dT}{\rho dl}\right)_{col} + \left(\frac{dT}{\rho dl}\right)_{rad} \hspace{2cm} \text{Eq.2.1}$$

where subscripts *col* and *rad* indicate collisional and radiative interactions, respectively.

2.2.1 Collision Stopping Power

The mass collision stopping power $(dT/\rho dl)_{col}$ expresses the average rate of energy loss by a charged particle from the sum of hard and soft collisions. The energy spent in collisional interactions produces ionization and excitation which contributes to the dose near the track. The formula for the mass collision stopping power for electrons is given by[31]:

$$(\frac{dT}{\rho dl})_{col} = \frac{2\pi \, r_e^2 m_e c^2 N_A Z}{\beta^2 M_A} \left[\ln\left(\frac{r^2(r+2)}{2\left(\frac{I}{m_e c^2}\right)^2} \right) + F^-(\tau) - \delta \right] \qquad \text{Eq. 2.2}$$

where

$$F^-(\tau) = 1 - \beta^2 + [r^2/8 - (2r+1) \, ln2]/(r+1)^2 \qquad \text{Eq. 2.3}$$

and

δ is the density effect correction, which account for the polarization or density effect in condensed media

$m_e c^2$ is the rest energy of the electron

r is $E/m_e c^2$, the ratio of kinetic energy E of the electrons to the rest energy

β is v/c

v is the velocity of the electron

c is the velocity of light in vacuum

N_A is the Avogadro constant

r_e is the electron radius

Z is the atomic number

M_A is the molar mass of substance A

I   is the mean excitation energy

The density effect correction δ accounts for the fact that collision stopping power decreases as a result of the polarization of the medium caused by the charged particle passage. The mean excitation potential *I* is a mean value of all ionization and excitation potentials of an atom in absorbing medium. Since it depends on the imparting charged particle type, values of *I* are often determined from measurement of heavy particles.

The rate of energy loss for collisional interactions depends on the electron energy and on the electron density of the medium (Figure 2.2). The rate of energy loss per gram per square centimeter, $\text{MeV·g}^{-1}\text{·cm}^{-2}$ (called the mass stopping power), is greater for low atomic number materials than for high atomic number materials. This is because high atomic number materials have fewer electrons per gram than lower atomic number materials and, moreover, high atomic number materials have a larger number of tightly bound electrons that are not available for this type of interaction.

2.2.2 Restricted Stopping Power

The δ-rays resulting from hard collisions may be energetic enough to carry kinetic energy a significant distance away from the track of the primary particle. As a result, in calculating absorbed dose in a small object or thin foil traversed by charged particles, the use of the mass collision stopping power will overestimate the dose, unless for the δ-rays charged particle equilibrium (CPE) exists. Therefore, a modified quantity called the restricted collision stopping power is used to calculate locally absorbed dose.

Restricted collision stopping power refers to the rate of energy loss per unit path length in collisions in which energy is 'locally' absorbed, excluding energy carried away by energetic secondary electrons (δ-rays). Therefore, the restricted collision mass

stopping power $(L/\rho)_{col}$ of a material for charged particles is defined as the quotient of dT by $\rho\, dl$:

$$\left(\frac{L}{\rho}\right)_{col,\Delta} = \left(\frac{dT}{\rho dl}\right)_{col,\Delta} \qquad \text{Eq. 2.4}$$

where dT is the energy lost by a charged particle in traversing a distance dl as a result of all the soft collisions plus the hard collisions with atomic electrons in which the energy loss is less than the cutoff value Δ.

An important form of the restricted stopping power is linear energy transfer (LET), which is of great importance in radiobiology and microdosimetry. The usual units for LET are keV/µm.

2.2.3 Radiative Stopping Power

The radiative stopping power refers to the rate of energy loss owing to radiative interactions. The electrons that undergo such energy losses contribute to the low energy tail (bremsstrahlung photon) of the primary electron energy distribution shown in Figure 2.6. For light charged particle such as electrons, the mass radiative stopping power is expressed as the rate of bremsstrahlung production, which can be written as:

$$\left(\frac{dT}{\rho dx}\right)_{rad} = \sigma_0 \frac{N_A Z^2}{A}(T + m_0 c^2)\overline{B_r} \qquad \text{Eq. 2.5}$$

where

σ_0 is the constant equals to $(e^2/m_0 c^2)/137 = 5.802\times10^{-28}$ cm^2/atom

$\overline{B_r}$ is a slowly varying function of Z and T, which has a value of $\frac{16}{3}$ for $T \ll$ 0.5 MeV, and roughly 6 for $T = 1$ MeV, 12 for 10 MeV, and 15 for 100 MeV in water.

Energy dissipated in radiative collisions is carried away from the charged-particle track by bremsstrahlung photons. The rate of energy loss for radiative interactions is approximately proportional to the electron energy and to the square of the atomic number of the absorber. This means that photon production through radiative losses is more efficient for higher energy electrons and higher atomic number materials.

It is evident from Figure 2.2 that the mass radiative stopping power increases almost linearly with kinetic energy in the MeV region, whereas the mass collision stopping power has a weak logarithmic energy dependence in that region. This is of importance for interpolation between different energies and the determination of the mean total energy losses.
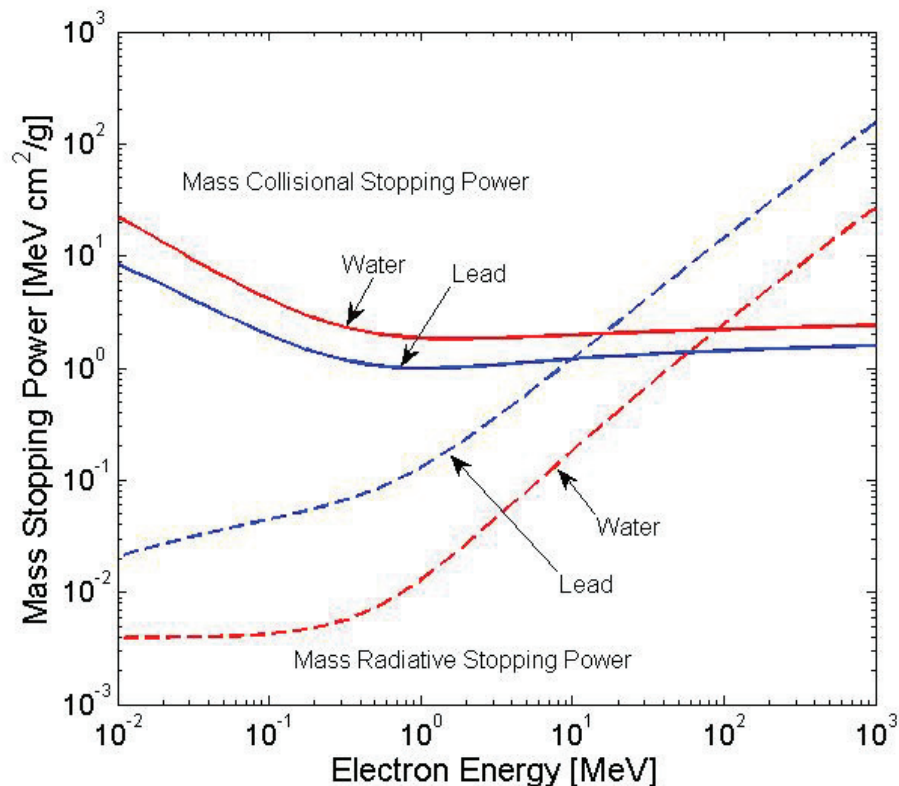
Figure 2.2 The mass radiative (solid lines) and collisional (dashed lines) stopping power plotted against electron kinetic energies for water and lead. Data was obtained from the National Institute of Standards and Technology (NIST)[33].

2.3 Electron range

The path length of a single electron is the total distance travelled along its actual trajectory to the point at which the electron comes to rest, regardless of the direction of movement. However, as electron passes through matter, it may suffer significant deflections, resulting in a tortuous path in the absorber medium, which is 1.2 to 4 times the linear thickness of the absorber traversed. The thickness of an absorber which the particle can just penetrate is called range R.

Since most of charged particle interactions individually transfer only minute fractions of the incident particle's kinetic energy, it is convenient to think of the particle as losing its kinetic energy gradually in a friction like process, often referred to as the "continuous slowing-down approximation (CSDA)". The CSDA range (or the mean path length) for an electron of initial energy T_0 can be defined by integrating the reciprocal of the total stopping power:

$$R_{CSDA} = \int_0^{T_0} (\frac{dT}{\rho dx})^{-1} dT \qquad\qquad \text{Eq. 2.6}$$

where T_0 is the starting energy of the particle.

CSDA range gives the path length which an electron would travel in the course of slowing down, in an unbounded uniform medium, if its rate of energy loss along the entire track was always equal to the mean rate of energy loss[34]. In reality, the rate of energy loss fluctuates, but this is neglected in CSDA. However, for practical purposes, CSDA range can be taken as identical to the range R.

When the CSDA range is known, the practical range R_p can be estimated by a scaling law. R_p is defined as the expectation value of the greatest depth of penetration of

the particle in its initial direction (Figure 2.6). It is most easily visualized in terms of flat layers of absorbing medium struck perpendicularly by a beam of charged particles.

The maximum range R_{max} (cm or g/cm^2) is defined as the depth at which extrapolation of the tail of the central axis depth dose curve meets the bremsstrahlung background (Figure 2.6). It is the largest penetration depth of electrons in the absorbing medium.

2.4 Electron Scattering

When a beam of electrons passes through an absorbing medium the electrons undergo multiple scattering, due to Coulomb force interactions between the incident electrons and predominantly the nuclei of the medium. The electrons will therefore acquire velocity components and displacements transverse to their original direction of motion. As the electron beam traverses the patient, its mean energy decreases and its angular spread increases. For most practical applications, the angular and spatial spread of a pencil electron beam can be approximated by a Gaussian distribution. The probability of a scattering event is quantified by the interaction cross-section σ. The unit for σ is cm^2/nucleus.

2.4.1 Single Scattering

Incident electrons have a high probability of experiencing nuclear elastic scattering, whereby the incident particle is deflected but does not radiate, nor does it excite the nucleus. The incident particle loses only an insignificant amount of kinetic energy required for conservation of momentum between the two particles. Though this is not a mechanism for energy-transfer to the absorbing medium, it is an important means of deflecting electrons. It is the principal reason that electrons follow very tortuous paths,

especially in high-Z media, and that electron backscattering increases with atomic number. In doing Monte Carlo calculations of electron transport (see section 2.7.3, below), it is often assumed for simplicity that the collisional energy-loss interactions may be treated separately from scattering (i.e., change-of-direction) interactions. The classical differential cross section $d\sigma$ for elastic nuclear scattering of electrons into a solid angle $d\Omega$ at a mean angle of θ is given by:

$$d\sigma = \frac{Z^2}{4}\left(\frac{e^2}{m_0 c^2}\right)^2 \left(\frac{1-\beta^2}{\beta^4}\right)\frac{1}{\sin^4(\theta/2)} d\Omega \qquad \text{Eq. 2.7}$$

where e is electric charge.

Equation 2.7 indicates that the differential elastic-scattering cross section per atom is proportional to Z^2. This means that a thin foil of high-Z material may be used to spread out an electron beam while minimizing the energy lost by the transmitted electrons in traversing a given mass thickness of foil.

For the scattering resulting from the inelastic collision, it can be treated as a collision between two free particles if the energy transfer is assumed to be much larger than the binding energy of the struck electron. Thus, the differential cross section $d\sigma$ for elastic nuclear scattering of electrons into a solid angle $d\Omega$ at a mean angle of θ is given by:

$$d\sigma = \left(\frac{e^2}{m_0 v^2}\right)^2 \left(\frac{1}{\sin^4\theta} + \frac{1}{\cos^4\theta}\right) 4\cos\theta \, d\Omega \qquad \text{Eq. 2.8}$$

It is evident that the electronic scattering only increases with the number of electrons per atom.

2.4.2 Multiple Scattering

More than one scattering of an electron is referred to as *plural scattering* and more than 20 scattering events is termed *multiple scattering*. The mean square scattering angle and the mass scattering power are used to describe multiple scattering events. The mean square angle for a single scattering event $\overline{\theta^2}$ is defined as follows:

$$\overline{\theta^2} = \frac{\int_0^{\theta max} \theta^2 \frac{d\sigma}{d\Omega} d\Omega}{\int_0^{\theta max} \frac{d\sigma}{d\Omega} d\Omega} = \frac{2\pi}{\sigma} \int_0^{\theta max} \theta^2 \frac{d\sigma}{d\Omega} sin\theta \, d\theta \qquad \text{Eq. 2.9}$$

where θ_{max} is the maximum scattering angle for the given interaction. The minimum and maximum scattering angles θ_{min} and θ_{max}, respectively, are angles where the deviation from point Coulomb nuclear field becomes significant. These departures from the point Coulomb field approximation appear at very small and very large angles θ, corresponding to very large and very small impact parameters b, respectively[35].

The mean square multiple scattering angle $\overline{\Theta^2}$ is characterized by a succession of small angle deflections symmetrically distributed about the incident particle direction. Since the successive single scattering collisions in the medium are independent events, it can be calculated from the mean square angle for single scattering $\overline{\theta^2}$ using:

$$\overline{\Theta^2} = n\overline{\theta^2} \qquad \text{Eq. 2.10}$$

According to the ICRU report 35[34], the multiple scattering of electrons traversing a path length l through an absorbing medium is commonly described by the mean square angle of scattering $\overline{\Theta^2}$ that is proportional to the mass thickness ρl of the absorber:

$$\frac{\overline{\Theta^2}}{\rho l} = 16\pi N_A \frac{Z^2}{M_a} r_e^2 (\frac{m_0 c^2}{\beta pc})^2 log \, [196Z^{-1/3}(\frac{Z}{A_r})^{1/6}] \qquad \text{Eq. 2.11}$$

2.4.3 Scattering Power

Analogous to the definition of stopping power, the mass scattering power T/ρ for an electron is defined by ICRU as the increase in mean square angle for multiple scattering $\overline{\Theta^2}$ per mass thickness[34]:

$$\frac{T}{\rho} = \frac{1}{\rho}\frac{d\overline{\Theta^2}}{dl} \qquad \text{Eq. 2.12}$$

or

$$\frac{T}{\rho} = \pi\left(\frac{2r_e Z}{(r+1)\beta^2}\right)^2 \frac{N_A}{M_A}\left\{\ln\left[1+\left(\frac{\theta_{max}}{\theta_{min}}\right)^2\right] - 1 + [1+\left(\frac{\theta_{max}}{\theta_{min}}\right)^2]^{-1}\right\} \qquad \text{Eq. 2.13}$$

where θ_{min} is the minimum scattering angle.

The scattering power varies approximately as the square of the absorber atomic number and inversely as the square of the electron kinetic energy (Figure 2.3). For this reason, high Z materials are used in the construction of scattering foil. Scattering foils spread out the electron beam that emerges from the accelerator treatment head and are thin to minimize photon contamination of the electron beam.

Due to multiple scattering, the electron paths become more oblique with depth regarding the original direction, which results in an increase in electron fluence along the beam central axis, i.e. the build-up region. The scattering power variations in heterogeneous tissues are also responsible for the production of local hot and cold spots in the underlying medium. Electrons are predominantly scattered outward by steep projections and inward by steep depressions (Figure 2.4). In practice, such sharp edges may be smoothed with an appropriately shaped bolus. Also, if a bolus is used to reduce beam penetration in a selected part of field, its edges should be tapered to minimize the effect.
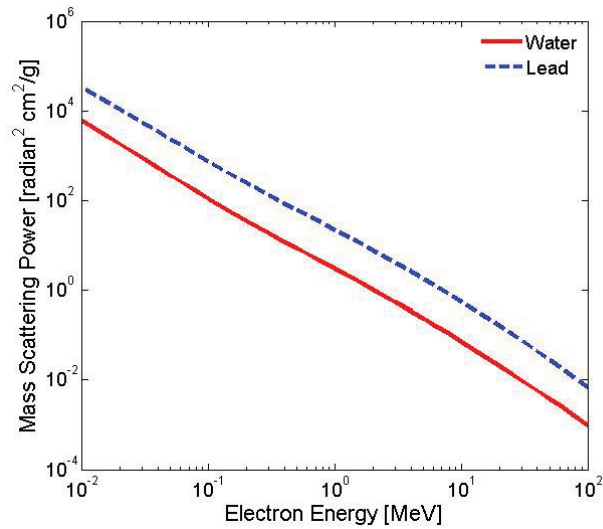
Figure 2.3 The mass scattering power plotted against electron kinetic energies for water and lead. Data was obtained from the ICRU-35[34].
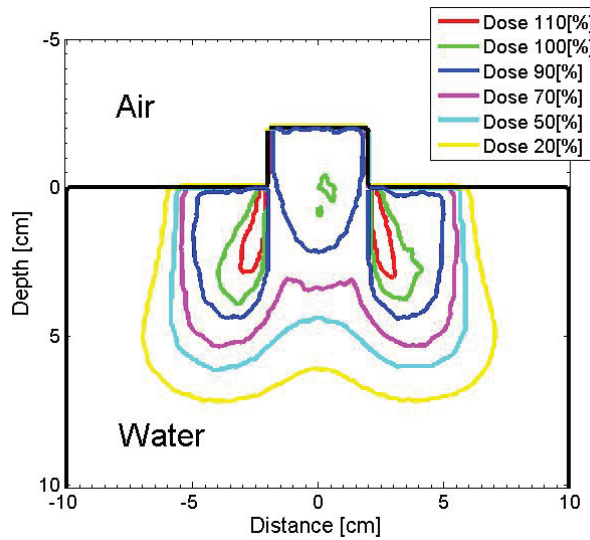
Figure 2.4 Effect of sharp edge affecting the dose distribution generated using Eclipse eMC

2.4.4 Backscattering

Although electron scattering occurs most likely in forward direction, there exists a small chance for backscattering. For electrons, backscattering due to nuclear elastic interactions can be an important cause of dose reduction in the absorbed medium, especially for high Z, low initial energy and thick target layers. However, electrons

incident on a thin foil, in which a backscattering event is equally likely to occur in the first or the last infinitesimal layer of the foil, require no backscattering correction to the absorbed dose.

2.5 Characteristics of Clinical Electron Beam[3]

2.5.1 Electron Source Position

In contrast to a photon beam which has a distinct focus located at the accelerator x-ray target, an electron beam appears to originate from a point in space that does not coincide with the physical plane of the scattering foil or the accelerator exit window. The term 'virtual source position' was introduced to indicate the virtual location of the electron source.

The effective source to surface distance (SSD_{eff}) for electron beams is defined as the distance from the virtual source position to the point of the nominal SSD (usually the surface of phantom or patient) (Figure 2.5). The inverse square law may be used for small SSD differences from the nominal SSD to make corrections to the absorbed dose for variations in air gaps between the patient surface and the applicator.

One commonly used method to determine the SSD_{eff} consists of measuring the dose at various distances from the electron applicator by varying the gap between the phantom surface and the applicator (with gaps ranging from 0 to 15 cm). In this method, doses are measured in a phantom at the depth of maximum dose d_{max}, with the phantom first in contact with the applicator (zero gap) and then at various distances g from the applicator. Suppose D_0 is the dose with zero gap ($g = 0$) and D_g is the dose with gap distance g. It follows then from the inverse square law that:

$$\frac{D_0}{D_g} = \left(\frac{SSD_{eff}+d_{max}+g}{SSD_{eff}+d_{max}}\right)^2$$

Eq. 2.14

Although SSD_{eff} is obtained from measurements at d_{max}, its value does not change appreciably with the depth of measurement. However, SSD_{eff} changes with beam energy, and has to be measured for all energies available in the clinic.
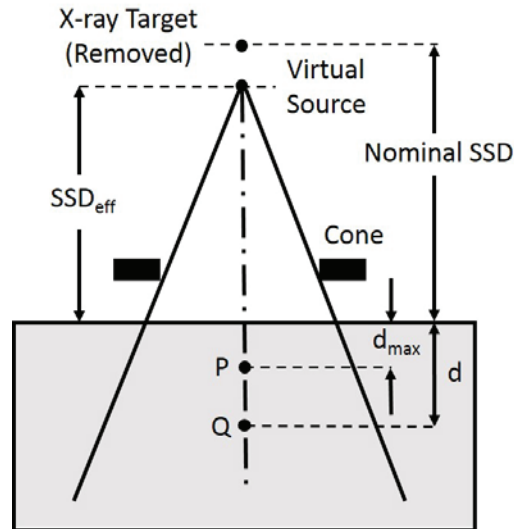
Figure 2.5 Definition of virtual point source of an electron beam: the intersection point of the backprojections along the most probable directions of motion of electrons at the patient surface.

2.5.2 Electron Beam Energy Specification

An electron beam is almost mono-energetic before striking the accelerator exit window, typically the kinetic energies ranging from 4 to 25 MeV[3.] The energy of this pencil beam is referred as nominal energy and is specified by the manufacturer. However, after the beam passes through the exit window, scattering foil, monitor chamber and air, the energy distribution becomes more complex and therefore need several parameters to describe the electron beam energy spectrum. In general, the most probable energy $E_{p,0}$ (the position of spectral peak) on the phantom surface, the mean energy $\overline{E_0}$ on the phantom surface, and R_{50} (the depth at which the absorbed dose falls to 50% of the maximum dose) are specified.

The most probable energy $E_{p,0}$ on the phantom surface is empirically related to the practical range Rp in water as follows:

$$E_{p,0} = 0.22 + 1.09R_P + 0.0025R_P{}^2 \qquad \text{Eq. 2.15}$$

where R_P is the practical range in centimeters.

The mean electron energy $\overline{E_0}$ at the phantom surface is related to the R_{50} as follows:

$$\overline{E_0} = C \cdot R_{50} \qquad \text{Eq. 2.16}$$

where $C = 2.33$ MeV cm^{-1} for water.

The mean electron energy $\overline{E_z}$ at the depth z is related to R_P as follows:

$$\overline{E_z} = \overline{E_0}\left(1 - \frac{z}{R_P}\right) \qquad \text{Eq. 2.17}$$

This parameter is important in dosimetry because it is necessary to know the mean electron energy at the location of the chamber for absorbed dose measurements.

2.5.3 Central Axis Depth-Dose Curves

As mentioned above, multiple scattering of electrons is predominant in media such as tissue due to their small mass. As a result, they do not give rise to a Bragg peak near the end of their projected range as heavy particles do. Typically, the electron beam central axis depth dose curve exhibits a high surface dose, in the range from 75% to 95%. The rate at which the dose increases from the surface to d_{max} is therefore less pronounced for electron beams than for photon beams. The dose then builds up to a maximum at a certain depth referred to as the electron beam depth of dose maximum D_{max}. Beyond D_{max} the dose drops off rapidly and levels off at a small low level dose component referred to as the bremsstrahlung tail. These features introduce a distinct clinical advantage over the photon modalities in the treatment of superficial tumours. The most useful treatment

depth of electrons is given by the depth of the 90% depth dose, which is referred as therapeutic range, and commonly a dose prescription is stated by indicating the absolute dose that should be delivered to that depth.
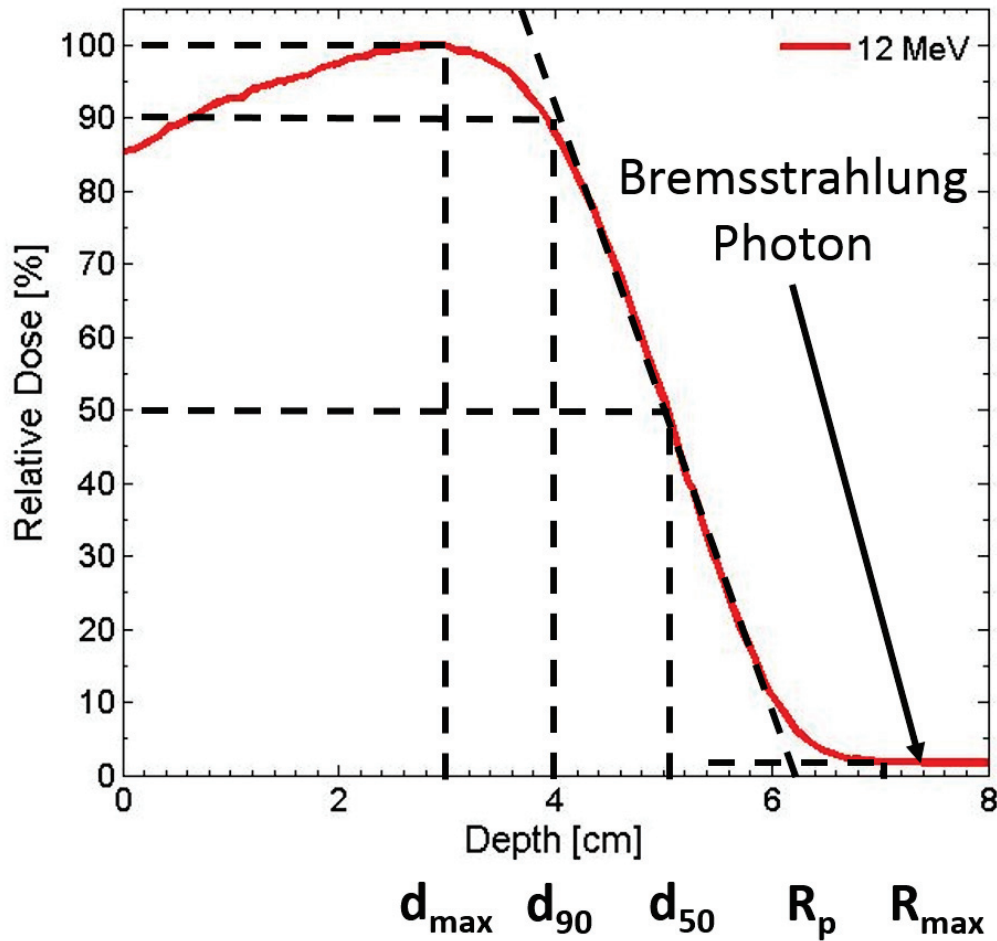
Figure 2.6 A typical 12 MeV electron beam PDD curve generated by Monte Carlo simulation to illustrate the build-up region, fall-off region and the defintion of d_{max}, d_{90}, d_{50}, R_P and R_{max}

The surface dose for electron beams increases with electron energy (Figure 2.7). As a rule of thumb, surface dose can be predicted by 70% + electron energy expressed in MeV. This can be explained by the nature of electron scatter. At lower energies, electrons are scattered more easily and through larger angles (see Figure 2.3). This

causes the dose to build up more rapidly and over a shorter distance. The ratio of surface dose to maximum dose is therefore lower for lower energy electrons than for higher energy electrons. Additionally, in the collision process between electrons and atomic electrons, it is possible that the kinetic energy acquired by the ejected electron is large enough (hard collision) to cause further ionization. In such a case, these secondary electrons also contribute to the buildup of dose.
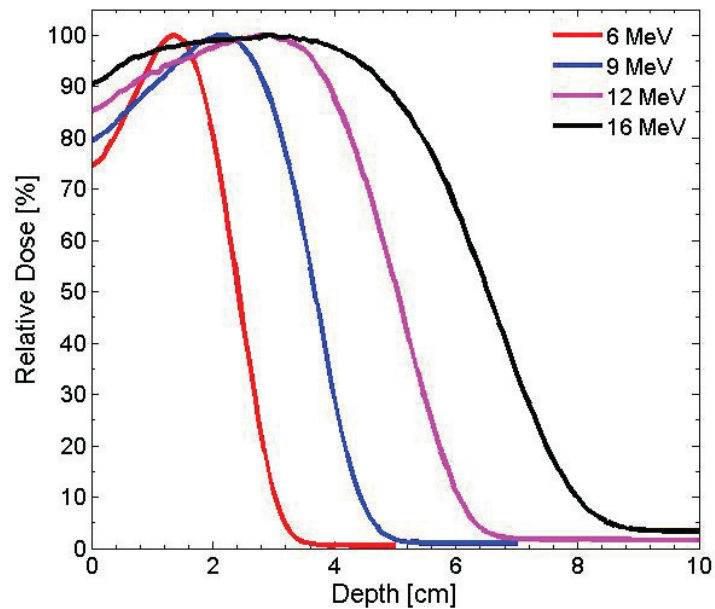
Figure 2.7 Energy dependence of PDD curves generated by Monte Carlo simulation. The PDD curves are normalized to 100% at d_{max} of each energy.

Scattering and continuous energy losses by electrons are the two processes responsible for the sharp drop-off in the electron dose at depths beyond d_{max}. The range of electrons increases with increasing electron energy. The gradient of fall-off region for lower electron energies is steeper than that for higher electron energies, since the lower energy electrons are scattered more easily and through larger angles. The stopping powers at low and high energy also affect the dose gradient. The bremsstrahlung

contamination depends on electron beam energy and is typically ~1% for 6 MeV and ~5% for 25 MeV electron beams[35].

2.5.4 Profile and Penumbra

A plot of the off-axis ratio against the distance from the central axis is referred to as a lateral dose profile. A typical dose profile for a 12 MeV electron beam and a 10×10 cm^2 field at d_{max} is shown in Figure 2.8. The profile relates the dose at any point in a plane perpendicular to the beam axis to the dose on the central axis in that plane. The lateral falloff of the beam is determined by the geometric penumbra (Figure 2.9) and reduced side scatter, while the region outside the geometric limits of the beam is the result of leakage and scatter from the collimation system.
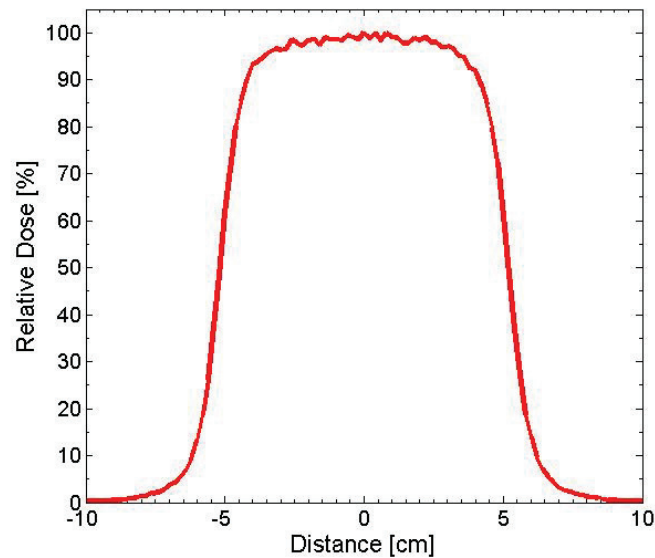
Figure 2.8 Monte Carlo simulated dose profile at depth d_{max} for a 12 MeV electron beam and 10×10 cm^2 field.

The physical penumbra of an electron beam is a rapidly varying function of depth and is defined as the distance between two specified dose levels at a specified depth, usually 80% and 20% isodose level.
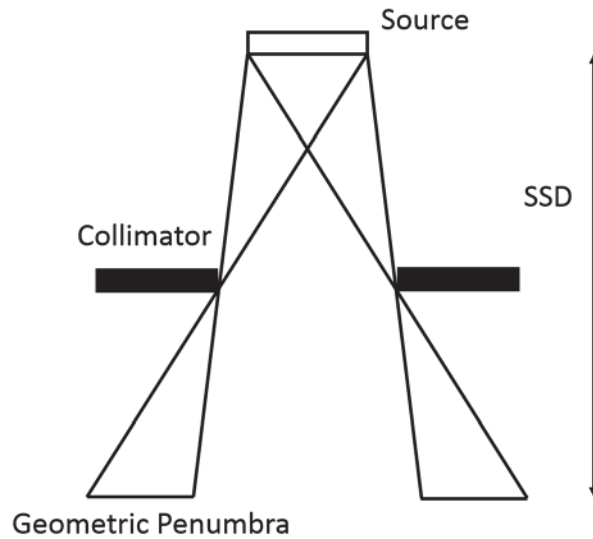
Figure 2.9 Definition of geometric penumbra

2.5.5 Isodose Lines

Isodose lines are 2D representations of points of equal dose. Isodose lines are usually drawn at regular increments of absorbed dose and are expressed as a percentage of the dose at a reference point, which is normally taken at the d_{max} point on the beam central axis. As an electron beam penetrates a medium, the beam expands rapidly below the surface due to scattering. However, the individual spread of the isodose curves varies depending on the isodose level, energy of the beam, field size and beam collimation.
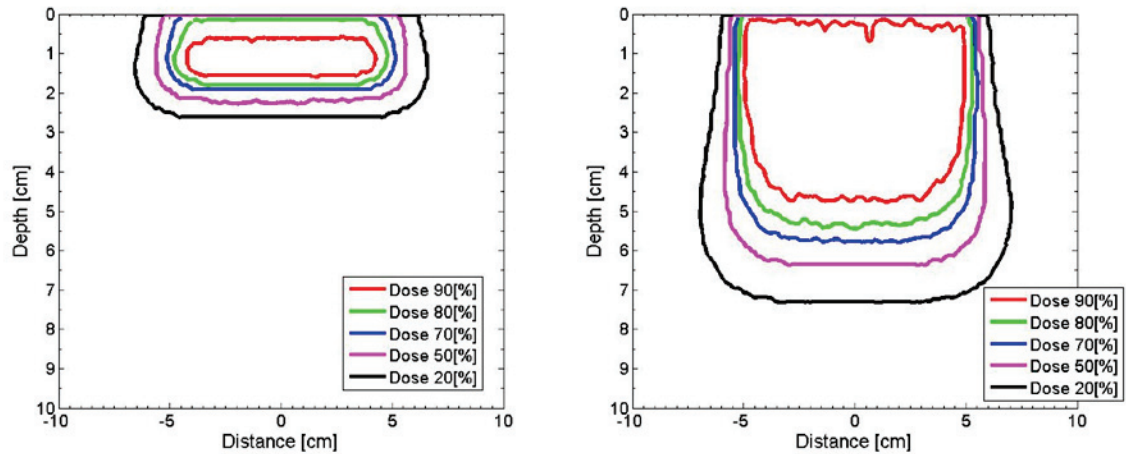
Figure 2.10 Isodose plot for 6 MeV (left) and 16 MeV (right) electron beam with 10×10 cm^2 field size in water generated using Eclipse eMC. Dose is normalized to $d_{max,\ 6MeV} =$ 1.2 cm for 6 MeV beam and $d_{max,\ 16MeV} = 3.0$ cm for 16 MeV beam.

A particular characteristic of electron beam isodose curves is the bulging of the low value isodose lines (<20%), which is a result of the increase in electron scattering angle with decreasing electron energy. Whereas for the low energy beams all the isodose lines show some expansion, for the higher energies only the low isodose levels bulge out. However, the higher isodose levels tend to show lateral constriction though becomes worse with decreasing field size. At energies above 15 MeV, electron beams exhibit a lateral constriction of the higher value isodose lines (>80%).

2.5.6 Field Size Dependence

An electron beam is defined as broad if its radius at the phantom surface is at least equal to its CSDA range[31]. When the distance between the central axis and the field edge is more than the lateral range of scattered electrons, lateral scatter equilibrium exists at the central axis and the depth dose for specific electron energy will be essentially independent of the field dimensions. For such large field sizes, the PDD curve

remains constant with increasing field size, since the electrons from the periphery of the field are not scattered sufficiently to contribute to the central axis depth dose.

However, with decreasing field size the decreasing degree of lateral electronic equilibrium will be present at the central axis, and the depth dose and output factors will show large sensitivity to field shape and size. In addition, d_{max} moves closer to the surface and the PDD curve becomes less steep as the field size is reduced because of the lack of side scatter equilibrium in air and phantom. This leads to a reduction in the output factor.

2.6 Dosimetry of Clinical Electron Beam

2.6.1 Calculation of absorbed dose

The absorbed dose is defined as the mean energy $\bar{E}$ imparted by ionizing radiation to matter of mass m in a finite volume V by[3]:

$$D = \frac{\bar{E}}{m}$$ Eq. 2.18

where the energy imparted $\bar{E}$ is the sum of all the energy entering the volume of interest minus all the energy leaving the volume, taking into account any mass energy conversion within the volume.

The absorbed dose to medium D_{med} is related to the electron fluence Φ_{med} in the medium and the stopping power of the medium under the conditions that i) radiative photons escape the volume of interest and ii) secondary electrons are absorbed on the spot or CPE of secondary electrons exists.

$$D_{med} = \Phi_{med} (\frac{\overline{S_{col}}}{\rho})_{med}$$ Eq. 2.19

where $\left(\frac{S_{col}}{\rho}\right)_{med}$ is the average unrestricted mass collision stopping power of the medium

at the energy of the electron.

The reading of a dosimeter placed in a medium is related to the dose absorbed by the detector's own medium, which may differ from the surrounding medium. Bragg-Gray cavity theory relates the dose absorbed by the detector placed in the medium and the dose that would have been absorbed in the medium that has a volume equal to that of the detector's effective volume. According to the Bragg-Gray theory, for electron beams under the condition of CPE, if the electron fluences are the same in water and the medium, the absorbed dose in water is related to the dose in medium by

$$D_{water} = D_{med} (\frac{\overline{S_{col}}}{\rho})_{med}^{water}$$
<div align="right">Eq. 2.20</div>

where $(\frac{\overline{S_{col}}}{\rho})_{med}^{water}$ is the ratio of the average unrestricted mass stopping power of water to that of the medium.

2.6.2 Cylindrical Chamber

Ionization chambers are the most widely used dosimeters for dose measurement in radiotherapy. An ionization chamber is a gas filled cavity surrounded by a conductive outer wall with a collecting electrode (Figure 2.11). The wall and the collecting electrode are separated with a high quality insulator to reduce the leakage current when a polarizing voltage is applied to the chamber.
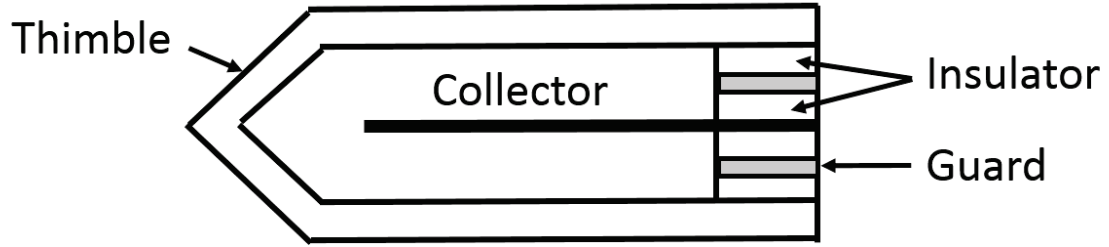
Figure 2.11 Basic design of a cylindrical ionization chamber

An ionization chamber measures the charge from the number of ion pairs created within a gas caused by incident radiation. The number of primary ions of either sign collected is proportional to the energy deposited by the charged particle tracks in the detector volume. Buildup caps are required to improve detection efficiency when measuring high energy photon radiation, but they should be removed when measuring lower energy photons (10–100 keV).

Cylindrical ionization chambers are more widely used for the measurement of central-axis depth-dose distributions. The use of cylindrical ionization chamber used for electron beam (especially low energy) dosimetry is recommended in TG-25[36], TG-51[37] and TG-70[38]. For electron beam measurements, the effective point of measurement of a cylindrical chamber is located at a point 0.5 times the radius of the air cavity in a cylindrical ion chamber (r_{cav}) upstream of the chamber axis where r_{cav} is the radius of the air cavity of a cylindrical ionization. This correction, i.e. chamber replacement correction factor P_{repl}, accounts for changes in the primary electron fluence spectrum, due to the presence of the chamber air cavity[37]. Thus, the calculation of depth-ionization curve can be given by the following equation:

$$PDI = 100 \times \frac{M(d)}{M(I_{max})}$$

Eq. 2.21

where $M(d)$ is the fully corrected ion chamber reading and I_{max} is the depth of the maximum ionization reading.

With the PDI curve, the beam quality specifier for the electron beam, R_{50}, can be determined from the measured value of the depth of 50% ionization curve (I_{50}) using:

$$R_{50} = 1.029 I_{50} - 0.06 \ (for \ 2 \ll I_{50} \ll 10 \ cm) \hspace{2cm} \text{Eq. 2.22}$$

or

$$R_{50} = 1.029 I_{50} - 0.37 \ (for \ I_{50} > 10 \ cm) \hspace{2cm} \text{Eq. 2.23}$$

which corrects the variations in mass collision stopping power ratios of water to medium with different electron energy.
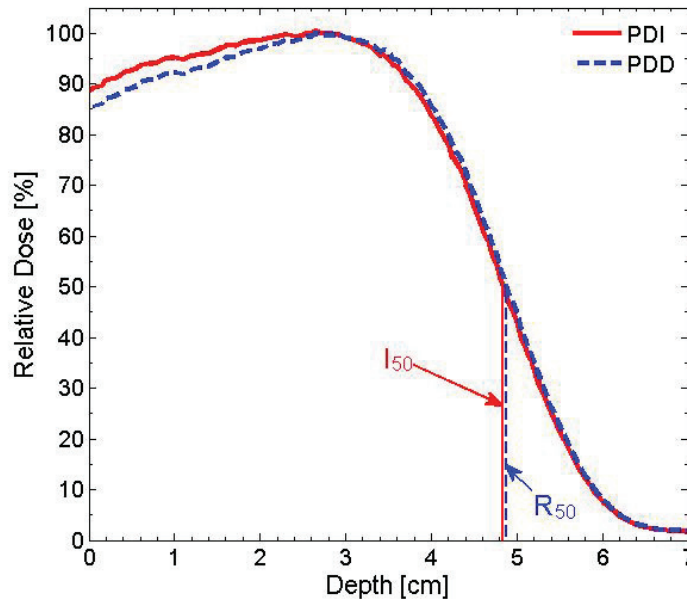
Figure 2.12 Illustration of shifting the PDI curve (solid line) into PDD curve (dashed line). The value of R_{50} is determined using I_{50}.

Depth ionization curves obtained with ionization chambers can be converted into depth-dose curves by making corrections for changes in stopping power ratio of water to

air with depth. In addition, perturbation and displacement corrections are required for cylindrical chambers:

$$PDD = PDI \times \frac{(\bar{L}/\rho)_{air}^{w}(R_{50},d) \cdot P_{fl}(E_d)}{(\bar{L}/\rho)_{air}^{w}(R_{50},d_{max}) \cdot P_{fl}(E_{d_{max}})}$$ Eq. 2.24

where $(\bar{L}/\rho)_{air}^{w}(R_{50},d)$ is water-to-air stopping-power ratios for realistic electron beams as a function of R_{50} (in cm) and depth d[37].

Compared to plane-parallel chambers, cylindrical chambers provide dosimetry data as accurate as plane-parallel chambers at depths greater than 0.5 r_{cav} but measurements in the buildup region have to be carefully evaluated.

2.6.3 Parallel Plate Chamber

Well-guarded thin-walled plane-parallel chambers are acceptable for the measurement of percentage depth-dose curves in water. The parallel-plate chamber is recommended for dosimetry of electron beams with energies below 10 MeV[38, 39]. A parallel-plate ionization chamber consists of two plane walls, one serving as an entry window and polarizing electrode and the other as the back wall and collecting electrode, as well as a guard ring system (Figure 2.13). The back wall is usually a block of conducting plastic or a non-conducting material with a thin conducting layer of graphite forming the collecting electrode and the guard ring system on top. When measurements are performed using a plane-parallel ionization chamber, the inner surface of the front window is to be selected as the measurement point of interest. The thickness of the front window of plane parallel chambers must be taken into account during the measurement setup.
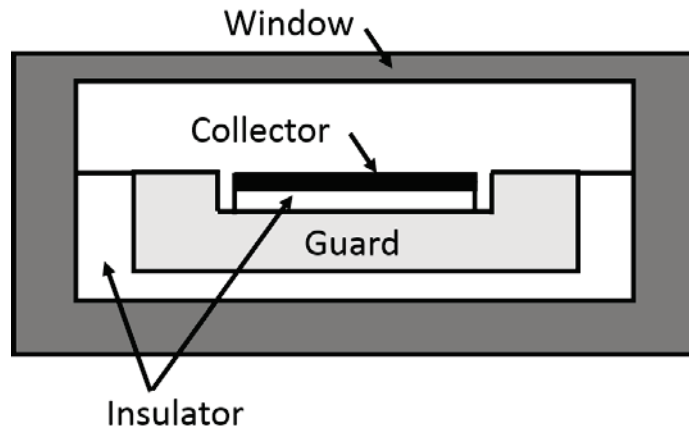
Figure 2.13 Basic design of a parallel plate ionization chamber

The response characteristics of plane-parallel ionization chambers differ from those of cylindrical chambers and offer certain advantages in comparison to cylindrical ionization chambers. Well-guarded plane-parallel ionization chambers are designed to minimize scattering perturbation effects, and the replacement perturbation correction factor P_{repl} can be taken as unity for some chambers. Additionally, the effective point of measurement of the chamber is the inner surface of the entrance window, at the center of the window for all beam qualities and depths. Thus the 'effective point of measurement' is the same as the point of measurement. These advantages of plane-parallel ionization chambers make them well suited for measurements of percentage depth dose and output factors. However, the polarity effect (i.e. difference between the charges collected when positive versus negative voltage is applied[39]) can lead to inaccuracies in the measurement of percentage depth dose when using plane-parallel chambers and therefore the true reading must be taken as the mean of the absolute values of readings taken at the two polarities.

2.6.4 Diode Dosimetry

Silicon diode detectors can also be used for the collection of relative electron dosimetric measurements. A diode dosimeter is a p–n junction diode. When being radiated, electron–hole pairs will be produced in the body of the dosimeter and diffuse into the depleted region (Figure 2.14). Under the action of the electric field resulted from the intrinsic potential, these pairs are swept across the depletion region. In this way a current is generated in the reverse direction in the diode.
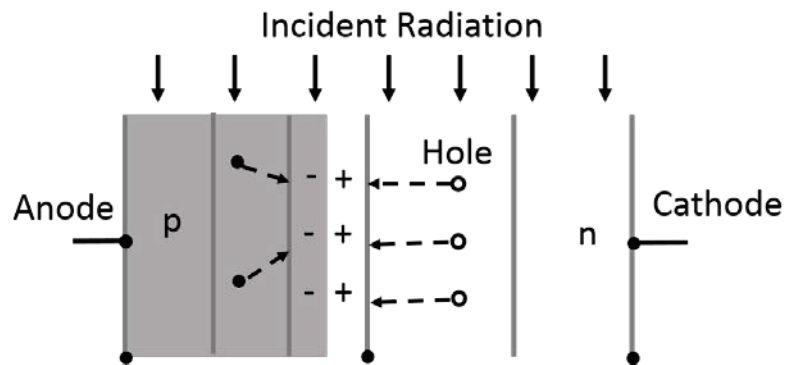
Figure 2.14 Schematic of silicon p–n junction diode dosimeter

Diodes offer an advantage with regard to small size and high sensitivity (i.e. thousands of times that of an air ionization chamber). A typical value of radiation sensitivity of a diode with external dimensions of $2.5 \times 2.5 \times 0.4$ mm^3 (sensitive volume of 0.3 mm^3) is 220 nC/Gy. This large signal makes the electrometer design much simpler than that required for ionization chambers. These characteristics plus an instantaneous electronic response make them ideally suited for scanning devices.

Since the variation of silicon-to-water stopping power ratio with electron energy is quite minimal for electron energies ranging from 5 to 25 MeV, measurements of dose distributions for electron beams made with a diode are used directly to give depth-dose distributions without depth-dependent corrections. Accuracy has been verified by

comparison with ionization chamber measurements of depth dose[40]. However, the dose rate dependence of diodes can change with exposure due to radiation damage, and hence calibration has to be repeated periodically.

Diodes can exhibit a directional dependence, with, for example, 10% lower response when the direction of the radiation beam is along the axis of the diode (perpendicular to the p-n junction) [40]. This directional response is caused partly by the detector construction and partly by back scattering from the patient or phantom. In addition, the user must be careful to use diode detectors specifically designed for electron beams and not ones designed for use in photon beams. The latter diodes are not suitable for electron beam measurements since they have high atomic number material added close to the sensitive volume to block photon backscatter, thus improving their photon energy sensitivity[38].

2.6.5 MOSFET Dosimetry System

A metal-oxide semiconductor field effect transistor (MOSFET) is a miniature silicon transistor that possesses excellent spatial resolution and offers very little attenuation of the beam due to its small size. MOSFETs have been in use in a variety of radiotherapy applications particularly for in vivo and phantom dose measurements, including routine patient dose verification, brachytherapy, total body irradiation (TBI), IMRT, intraoperative radiotherapy and radiosurgery[3]. Though MOSFET dosimeters have a limited lifespan, they retain adequate linearity during their specified lifespan.

MOSFET dosimeters are based on the measurement of the threshold voltage shift ΔV_{TH} (Figure 2.15), which is a linear function of absorbed dose. Ionizing radiation penetrating the oxide generates charge that is permanently trapped, thus causing a change

in threshold voltage. The difference in voltage before and after exposure can be measured, and is proportional to integrated dose. MOSFETs require a connection to a bias voltage during irradiation, and thus the dosimeter should be calibrated before use. For megavoltage beams, however, MOSFETs do not require energy correction for each energy, and a single calibration factor can be used[3].

However, MOSFETs are sensitive to changes in the bias voltage during irradiation, and their response drifts slightly after the irradiation which means the reading must be taken in a specified time after exposure.
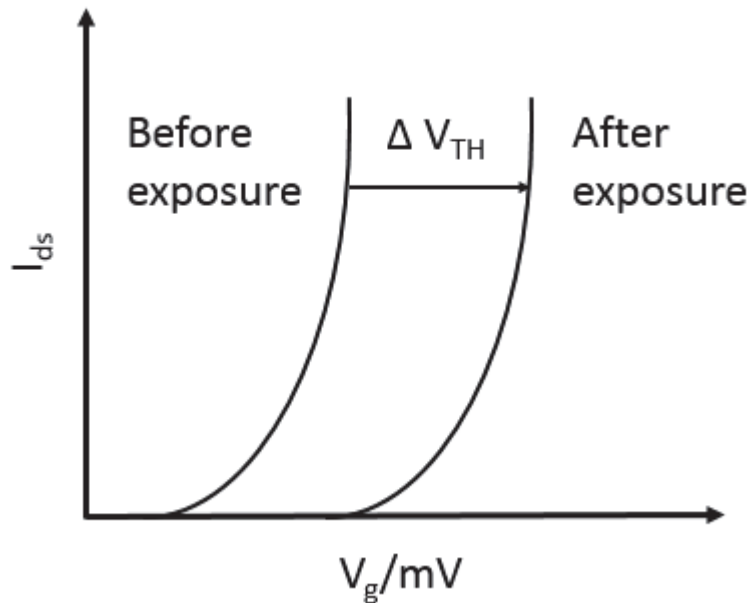
Figure 2.15 Schematic illustration of threshold voltage shift, where I_{ds} is the current between source and drain of the MSOFET

2.7 Dose calculation algorithms for electron beams

In order to perform radiation dose distribution calculations in phantom or in the human body, calculation algorithms are required to accurately model the beam behavior during its transport through matter. The fundamental requirement for the model is that it should be capable of reproducing the dose distribution obtained experimentally under the

range of conditions encountered in clinical application. With Monte Carlo algorithm, accuracy within 3% dose or 3 mm distance to agreement is achievable[38].

2.7.1 Pencil Beam Algorithm (PBA)

Pencil beam algorithms were developed based on Gaussian pencil beam distributions calculated with the application of Fermi-Eyges multiple scattering theory[41].

As summarized by Khan[42], the dose distribution resulting from an infinitesimally narrow electron beam, or pencil beam, incident on a uniform phantom assumes a teardrop shape in water, with its axis along the beam axis (Figure 2.16). Broad electron beams can be considered as a collection of pencil beams passing through the electron collimator aperture. Assuming a small angle multiple scattering approximation, an elementary pencil beam penetrating a scattering medium is nearly Gaussian in its lateral spread at all depths[43]. The spatial dose d_p to a point deposited by a Gaussian pencil beam can be represented as:

$$d_p(x,y,z) = D_\infty(0,0,z) \frac{e^{-\frac{(x-x')^2+(y-y')^2}{2\pi\sigma^2(x',y',z)}}}{2\pi\sigma^2(x',y',z)} \qquad \text{Eq. 2.25}$$

where $d_p(x,y,z)$ is the dose contributed to point *(x, y, z)* by a pencil beam whose central axis passes through *(x', y', z)* and σ^2 is the mean square radial displacement of electrons as a result of multiple Coulomb scattering. $D_\infty(0,0,z)$ is the dose at depth z in an infinitely broad field with the same incident fluence at the surface as the pencil beam. The Gaussian distribution function in equation 2.25 is normalized so that the area integral of this function over a transverse plane at depth z is unity.
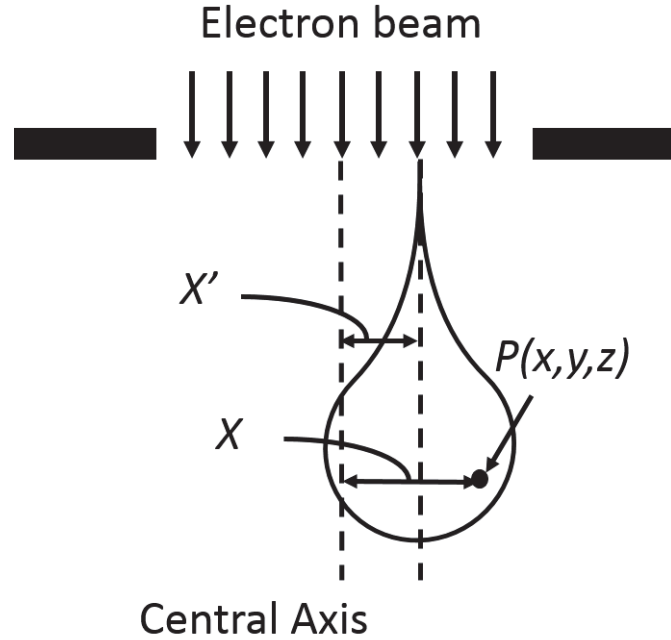
Figure 2.16 Schematic representation pencil beam algorithm for determination of dose distribution in a patient's cross-section in the *x-z* plane of a clinical electron beam.

The total dose distribution in a field of any size and shape can be calculated by integrating all the pencil beams:

$$D(x, y, z) = \iint d_p(x - x', y - y', z) dx' dy' \qquad \text{Eq. 2.26}$$

where $d_p(x'-x, y'-y, z)$ is the dose contribution at *x, y, z* from the pencil beam at *x', y'*.

The integration of a Gaussian function within finite limits cannot be performed analytically, and thus to evacuate this function it is necessary to use error function (*erf*). The convolution calculus shows that for an electron beam of a rectangular cross section (*2a×2b*), the spatial dose distribution is given by:

$$D(x, y, z) = D_\infty(0,0,z) \cdot \frac{1}{4} \left(erf \frac{a+x}{\sigma_r(z)} + erf \frac{a-x}{\sigma_r(z)} \right) \left(erf \frac{b+y}{\sigma_r(z)} + erf \frac{b-y}{\sigma_r(z)} \right) \qquad \text{Eq. 2.27}$$

where the error function is defined as:

$$erf(x) = \frac{2}{\sqrt{\pi}} \int_0^x e^{-t^2} dt \qquad \text{Eq. 2.28}$$

54

The error function is normalized so that *erf* (∞) = 1. The quantity $D_\infty(0,0,z)$ is determined from the measured central axis depth-dose of a broad electron field.

The lateral spread σ increases with depth until a maximum spread is achieved. Beyond this depth there is a precipitous loss of electrons as their larger lateral excursion causes them to run out of energy. Eyges predicted σ theoretically by extending the small-angle multiple scattering theory of Fermi to slab geometry of any composition. Considering $\sigma_x(z)$ in the *x-z* plane:

$$\sigma_x^2(z) = \frac{1}{2}\int\left(\left(\frac{\theta^2}{\rho l}\right)(z')\right)\rho(z')(z-z')^2 dz'$$ Eq. 2.29

where $\sigma_x^2(z)$ is the square of the projection on the *x-z* plane of the lateral spread at depth z, $\theta^2/\rho l$ is the mass angular scattering power and ρ is the density of the slab phantom. Equation 2.29 takes account into secondary particles, energy straggling, loss of electrons whose range is smaller than the lateral excursion and large angle scatter. However, this expression has several limitations: (1) since this model is based on small angel scatter only, it underestimates large angle scattering; (2) the lateral spread σ increases indefinitely, which is contrary to the experimental results; (3) the model does not consider the loss of electrons when lateral distances exceed the range of electrons.

Practical implementation of the above algorithm was carried out by Hogstrom *et al.*[43] and was subsequently adopted by several commercial treatment planning systems. The electron linear collision stopping and linear angular scattering power relative to that of water (or CT numbers), effective depth and σ are calculated for inhomogeneous media. Thus the method allows pixel-by-pixel calculation of inhomogeneity correction.

However, due to the limitation in Fermi–Eyges theory, PBA has limited accuracy in predicting the dose distribution in geometries that account for the internal inhomogeneity[43, 44]. For each pencil beam traversing the medium, the electron energy changes with depth only and the heterogeneities intersecting the central ray are extended temporarily into a semi-infinite slab. Due to this semi-infinite slab approximation, the pencil beam algorithm has been shown to fail when the pencil beam spread exceeds the cross-section of the heterogeneity or when parts of the pencil beam traverse distinct heterogeneities at interfaces. Though improved algorithms were designed and could accurately calculate dose in patients, there was a trend of using more accurate approach towards Monte Carlo simulation.

2.7.2 Tissue inhomogeneities in electron beam dose calculation

The dose distribution produced by an electron beam can be greatly affected by the presence of tissue inhomogeneities such as lung, bone or air cavities. The dose within or around these inhomogeneities is challenging to calculate or measure through analytic means, e.g., the Pencil Beam approach discussed in section 2.7.1 above, because of complex scattering effects. Tissue heterogeneities affect the penetration of the beam because of differences in stopping power, which are a result of different electron densities and tissue compositions. However, in most clinical situations, differences in scattering power have a much larger effect. Localized heterogeneities disrupt lateral scatter equilibrium, causing local hot and cold spots.

The simplest correction for tissue inhomogeneities involves the scaling of the inhomogeneity thickness by its density relative to water and the determination of a coefficient of equivalent thickness (CET). It is assumed that the attenuation by a given

thickness z of the inhomogeneity is equivalent to the attenuation ($z \times CET$) of water. The CET of a material is given by its electron density relative to the electron density of water and is essentially equivalent to the mass density of the inhomogeneity. The CET can be used to determine an effective depth in water equivalent tissue z_{eff} through the following expression:

$$z_{eff} = z - t(1 - CET)$$
<div align="right">Eq. 2.30</div>

where z is the actual depth of the point in the patient and t is the physical thickness of the inhomogeneity.
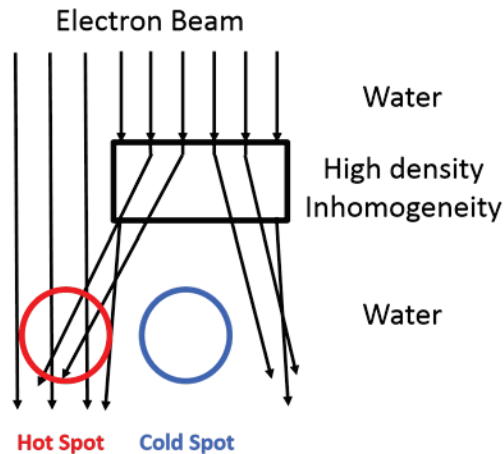
Figure 2.17 Schematic representation of electron scatter behind small high density inhomogeneity

The CET method is useful for a first-order estimate of penetration of electrons for simple, e.g., slab-type geometries. However, as indicated in the TG-70[38], it is approximate even in slab geometry and cannot handle more complex inhomogeneities. For example, for a small (compared to field size) high-density heterogeneity, electrons are more likely to be scattered away from the high-density region than to be scattered toward it. Behind the heterogeneity, the fluence perturbation creates hot spots lateral to

the heterogeneity and corresponding cold spots directly under the heterogeneity (Figure 2.17). A small low-density heterogeneity has the opposite effect.

2.7.3 Monte Carlo (MC) Simulation

Monte Carlo simulations are a broad class of computational algorithms that rely on repeated random sampling to obtain numerical results, typically running simulations many times over in order to obtain the distribution of an unknown probabilistic entity. The name Monte Carlo comes from the use of random numbers, i.e., similar to outcomes produced by rolling of dice or spinning of a Roulette wheel. Monte Carlo techniques are often used in physical and mathematical problems, particularly when they are intractable by analytic methods. Monte Carlo simulation is often computationally intensive.

In radiation therapy, Monte Carlo methods can model the physical processes of radiation transport, simulating the extensive random trajectories of individual particles by using a random number generator. With Monte Carlo method, the known probability distributions that govern the physical interaction processes of photons, positrons and electrons in matter can be sampled. The technique is accepted as the most accurate and versatile method for radiation dose calculation. A Monte Carlo radiation transport algorithm simulates the transport of individual incident particles in a modeled beam as well as all secondary particles that receive kinetic energy during the transport process. Discrete photon interactions, such photoelectric absorption, coherent or incoherent scatter, pair production, as well as collisional and radiative losses by charged particles are modeled by sampling well-known probability distributions using random numbers. Along the path of the particle, selected physical quantities of interest, e.g., such as energy absorbed, are stored (or, in Monte Carlo terminology, "scored"). After transport of a

large number of particles, the average and the standard deviation of these quantities may be calculated. A single particle's history is defined from the beginning of its transport until both the original particle and all progeny are absorbed (or have energies below a specified threshold), or exit the volume of interest.

2.7.3.1 Electron-Gamma Shower (EGS) computer code

The Electron-Gamma Shower (EGS) computer code system[45] is a general purpose package for the Monte Carlo simulation of the coupled transport of electrons and photons in an arbitrary geometry for particles with energies from a few keV up to several TeV. EGS is written to simulate three-dimensional electromagnetic showers in any media. Showers are developed by simulating in as much detail as possible the various electromagnetic shower processes. The probability distributions of the processes are used, so an EGS simulation mimics in detail real showers with real fluctuations. EGS itself is geometry independent; the geometry is communicated to EGS through a user-written subroutine which EGS calls.

In radiation dosimetry, particles transported are stored on a stack with their parameters such as the charge, energy, position and direction. A particle's history is defined from the beginning of its transport until both the original particle and its progeny are absorbed or exit the volume of interest.

Unlike the transport of photons which can be simulated on a per-interaction basis, it is impractical to simulate each collision of electrons individually. Therefore, a "condensed history technique" [46] is required to simulate the large number of electron interactions, including secondary knock-on electrons and excitation of atoms. This relies on the fact that most electron interactions involve little direction change or energy

transfer. In the condensed history technique, the path of an electron is partitioned into short, linear steps to approximate the curve (Figure 2.18). For each step, the effects of the numerous electron interactions occurring are grouped together so that each step can result in the aggregate effect of many interactions. The overall deflection angle sampled from multiple scattering distributions is applied at the end of each step.
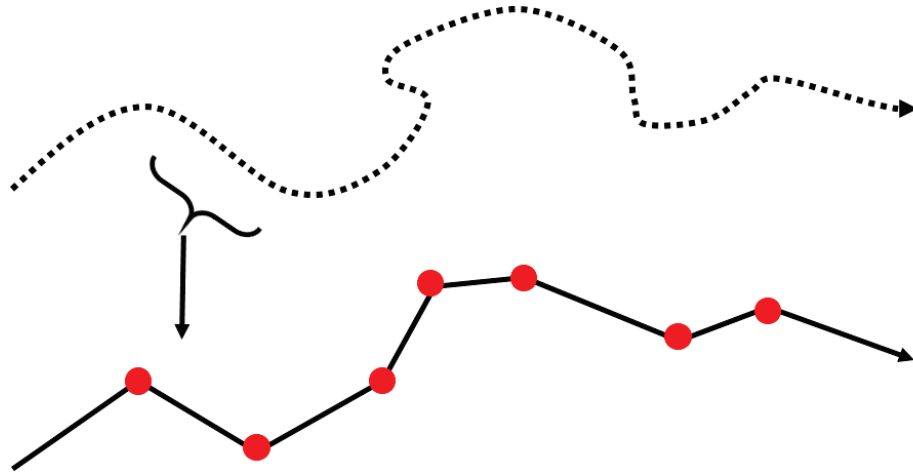
Figure 2.18 In the condense history technique, a continuous electron path is divided into small steps, whereby each step represents the aggregate effect of many interactions.

In EGS, the electron transport algorithm starts by reading the energy, position and direction of the electron on the top of the stack. If the electron energy is lower than the electron energy cut-off (ECUT) or if the electron is outside the geometry, it is discarded. Otherwise, the distance to the next discrete interaction site is sampled with the random number generator. An upper limit to the multiple scatter step size and a transport algorithm for a given position (usually varies with proximity to a region boundary) are specified by the user. The net deflection angle is sampled depending on the electron energy and applied to the trajectory. An energy corresponding to the step length times the restricted collisional stopping power for creation of knock-on electrons is lost during the step. During this transport, discrete interactions are possible, such as the emission of

a bremsstrahlung photon or δ-ray. At this point, the interaction type is sampled as well as its energy and direction. The parameters of the secondary particle are stored on the particles's stack and the primary particle's energy and direction are modified accordingly.

2.7.3.2 Clinical Implementation of Monte Carlo Dose Calculation

To improve the speed of traditional eMC calculation without loss in accuracy, the macro Monte Carlo (MMC) method was developed[47]. The MMC algorithm uses pre-calculated data to track electrons through the patient geometry. The pre-calculated data arises from EGSnrc Monte Carlo calculations (described in section 2.7.3.1) for a spherical geometry. These calculation results are performed to determine the probability distribution functions (PDF) for exit position, direction and energy of the primary electron emerging from the sphere dependent on its density and material as well as the initial energy of the electron. The electron transport in the MMC is based on sampling values from the PDF database. An electron's trajectory through matter is transformed into a chain of spheres, where the location of each sphere is dependent on the position and direction of the primary electron exciting the previous sphere (Figure 2.19). A simplified scattering model is used to account for energy deposited by secondary particles, in which only the average energy transferred to these particles is stored as a function of incident primary electron energy.

The density value of a sphere in the patient geometry is determined by the average density of the voxels covered by sphere, it covers in the CT data. Each voxel is assigned to an index corresponding to the maximum radius of sphere that can still be used from the current voxel center without reaching into other materials. Two voxels of the density value are considered to lie on different sides of an interface if the ratio of

densities of the two voxels exceeds a user controlled limit. This method allows the MMC algorithm to reduce the computing time required for MC simulation.

Energy deposited from primary electrons is along a straight line from the point where the electron enters the sphere to the point where it leaves (dotted lines inside the spheres, Figure 2.19). The energy deposition due to secondary particles (electrons and photons) released in a sphere in each MMC step is not transported, but stored in those voxels where secondary energy deposition has been released. Transport and deposition of these dose contributions are handled by post processing of the secondary energy deposition volumes after the actual simulation.
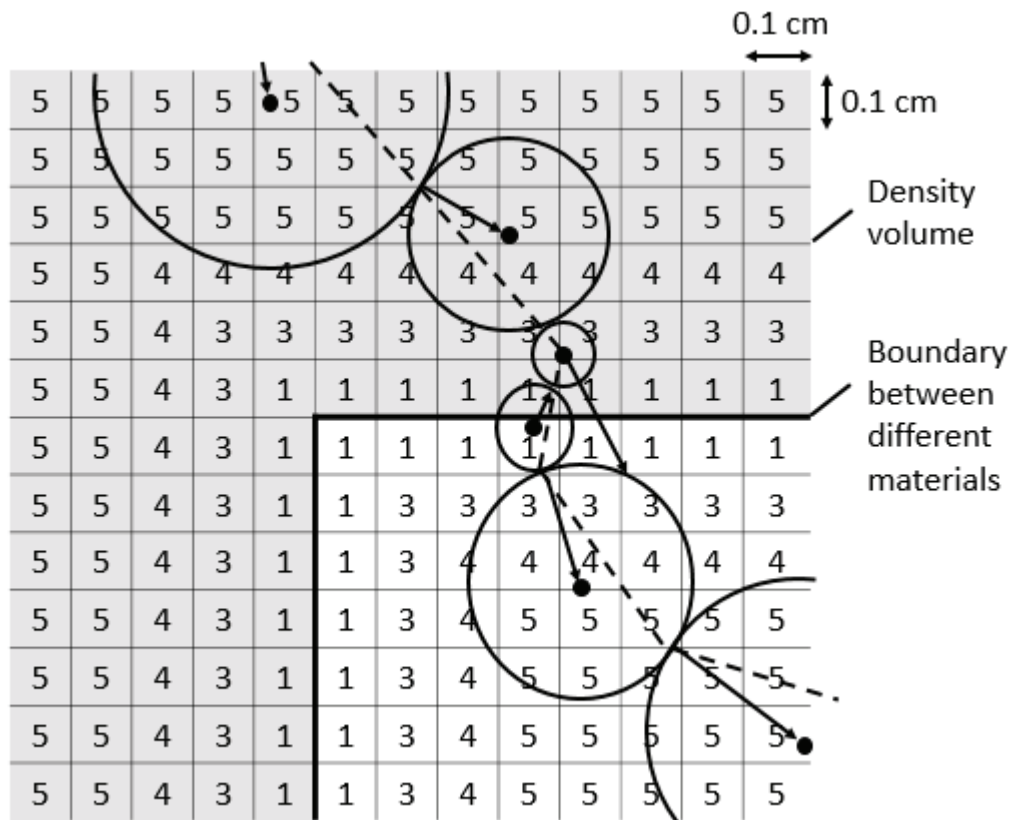
Figure 2.19 2D illustration of MMC algorithm which has a density volume of 0.1 cm^2 resolution

Chapter 3 MATERIAL AND METHODS

3.1 Dose Calculation Algorithm

3.1.1 Eclipse Electron Monte Carlo

For the convenience of applying the methodology in this work into clinical treatment, dose calculation is implemented using Varian Eclipse treatment planning system (Eclipse version 10.0), where a commercial Monte Carlo-based dose calculation algorithm is available for electron beam treatment planning. Varian Eclipse electron Monte Carlo (eMC) algorithm is a fast implementation of the Monte Carlo method for dose distribution calculation from high energy electron beams in radiotherapy treatment planning. The algorithm consists of an electron transport/dose deposition model (i.e. Macro Monte Carlo), performing the transport and dose deposition caused by the electrons in the patient and electron beam phase-space model (Initial Phase Space model, IPS), describing the electrons that emerge from the treatment head of the linear accelerator. The accuracy of implementation of this algorithm in Eclipse has been demonstrated by several groups[47-49].

The IPS model acts as the particle source for the MMC. Electrons and photons are generated according to a mathematical model of the beam, which is adapted to measured electron beam data. The IPS plane is located at a distance of 95 cm from the beam source, just below the applicator, thus taking into account the field shape of applied cutout. Four beam components are used to describe the properties of the electron beam in the plane, including main diverging beam, applicator scatter, applicator transmission and second diverging beam. The last component models the electrons and photons that have interacted with various other parts of the linac head before passing

through applicator diaphragm, and are not modeled by the first three components. With the appropriate weights of these components an accurate input for electron beam calculation can be generated. For configuration, open beam and applicator-specific depth-dose curves have to be supplied for each energy, including absolute dose in cGy/MU at a defined point on the depth dose curve, as well as the profiles in air measured in an open beam without applicator.

In the eMC implementation, the user is able to adjust several parameters that affect calculation duration and accuracy, including calculation grid size, target statistical accuracy, maximum number of particle histories, smoothing method, and smoothing level. The target statistical accuracy is defined as the average statistical uncertainty of all voxels with doses larger than 50% of d_{max}. Smoothing is optional and can be performed by means of a 3D Gaussian filter or a 2D median filter. Both can be applied with three different smoothing strengths. Furthermore, the maximum amount of particle histories and the random generator or seed can be chosen, as well as an accuracy limit for the monitor unit calculation.

3.1.2 EGSnrc

Although the Eclipse treatment planning system, incorporating electron Monte Carlo planning, can accurately predict isodose distributions and monitor units (within an accuracy of approximately 2.5%[50]) for field sizes as small as 3.0 cm diameter and for energies in the 6 to 20 MeV range at 100 cm SSD, its capability is limited for smaller field sizes[49, 50]. Therefore, for the study of small electron field sizes in this work, EGSnrc code is used.

EGSnrc, developed by National Research Council Canada, is used to address a broad range of problems involving the propagation of radiation in media. It is particularly well-suited for medical physics purposes, such as the research and development of devices that allow medical professionals to generate or detect radiation, e.g., radiographic imaging of a patient's anatomy[51, 52] or delivery of a prescribed radiation dose to a tumour[53]. The software is also employed directly by medical physicists in cancer clinics for research and for verifying radiation treatment plans[54]. The main components of EGSnrc code consist of the cross-section data for all the interaction processes considered in the simulation, the transport algorithm, the methods for geometry specification and determination of quantities of interest and the data analysis tools.

BEAMnrc[55] and DOSXYZnrc[56] are specific codes that call EGSnrc transport routines and allow, respectively, modeling of external beam treatment units and deposition of radiation dose within a Cartesian geometry. BEAMnrc allows simulation the production of radiation beams from any radiotherapy source, in particular electron or photon beams generated by a clinical linear accelerator. The accelerator model is built by arranging individual component modules (CMs) perpendicularly to the central axis of the beam. The dimensions and material of each CM are specified in an input file. In modeling a linear accelerator, various characteristics of the electron source are configurable, including the energy spectrum and spatial distribution. The input file also contains transport parameters such as the electron and photon energy cut-off parameters (ECUT and PCUT) below which the particle is discarded, the threshold energy for creation of knock-on electrons and bremsstrahlung photons (AE and AP), the value of which usually equal to the corresponding energy cut-off. The BEAMnrc code then

produces a phase space output of the beam at any specified plane in the simulation geometry, which contains for each emergent particle, the energy, charge, position, direction and weight, as well as a record of the regions with in which the particle interacted or travelled en route to the plane. Various characteristics of the phase space may be read from the phase space file using the utility script BEAM data processor (BEAMdp).

The DOSXYZnrc user code is useful for calculating dose distributions in a rectilinear voxelized phantom. A variety of beams may be specified as incident on the phantom, including full phase-space files from BEAMnrc. A phantom can be created either directly in DOSXYZnrc by specifying the dimensions and materials of an arrangement of voxels, or by converting a CT data set by converting Hounsfield Units into specified materials with appropriate densities. The DOSXYZnrc code includes a restart facility and can be run on parallel computing platforms. The statistical analysis is based on a history by history method[57].

3.2 Radiation detectors

To validate the accuracy of eMC calculation with PLA involved phantom as well as the CET value determined by eMC, measurement of PDD curves is required. While the cylindrical chamber is selected as the main detector for the measurement, a parallel plate chamber is used to enhance the measurement of surface dose. The Semiflex Ionization Chamber (model 31010, PTW, Freiburg, DE) has a vented sensitive volume of 0.125 cm^3 with a flat energy response within a wide energy range from 6 MeV to 50 MeV. The chambers are shaped cylindrically and have an inner diameter of 5.5 mm. The Exradin A11 parallel plate chamber (Standard Imaging, Inc., Middleton, WI) has a

collecting volume of 0.62 cm^3. The collector has a diameter of 20 mm with the window collector gap of 2.0 mm.

3.3 Bolus Design for Electron Therapy

A novel in-house algorithm for bolus design is developed to achieve specific dosimetric goals that currently lack practical solutions. The bolus design workflow is presented in Figure 3.1. The workflow starts with creating a conventional electron plan in the planning system, following the same prototype as the current procedure with regard to field definition, dose calculation, dose normalization and generation of required output. In this initial plan, the energy and aperture are specified such that the distal part of 90% isodose will cover all portions of the distal PTV while a bolus can be specified in two ways: i) in the case that PTV coverage is achieved without the bolus, by adding 1.0 cm thick bolus to define the surface that will be occupied by the bolus, without linking the bolus to the electron field such that it is omitted from the dose calculation; or ii) a bolus linked to the electron field and therefore taken into account by the dose calculation, thus helping the attainment of PTV coverage, i.e. increasing surface dose or creating flat surface. The dose distribution is calculated using the electron Monte Carlo (eMC) algorithm, with 0.1 cm grid size, accuracy of 2% and medium smoothing level. Following calculation, the user must convert the covering isodose surface (e.g., 90%) and nominal hot-spot isodose surface (e.g., 110%) into a structure for subsequent use by the bolus design algorithm. All the digital imaging and communication in medicine (DICOM, which is a standard protocol for transmitting information in medical imaging) objects (images, structures, dose and plan) are then exported to the bolus design algorithm. This algorithm, implemented in Matlab, optimizes the bolus design for the

same energy, field size and SSD. The new bolus object is then exported to Eclipse for accurate eMC calculation using the same MU as the original calculation. If required, this cycle is iterated until an acceptable design is realized. The final bolus is fabricated using a 3D Printer (Replicator 2, MakerBot Industries, LLC, Brooklyn, NY) using PLA as a material. The fabricated bolus is then checked for proper fitting on the patient and imaged in place using CT (LightSpeed 16, GE Healthcare Ltd) for final dose calculation to be used for the treatment delivery. The final step allows the practitioner to assess the fit based on imaging, and also takes into account the actual dimensions and density, as well as any imperfections (e.g. air gaps) for the final dose calculation.
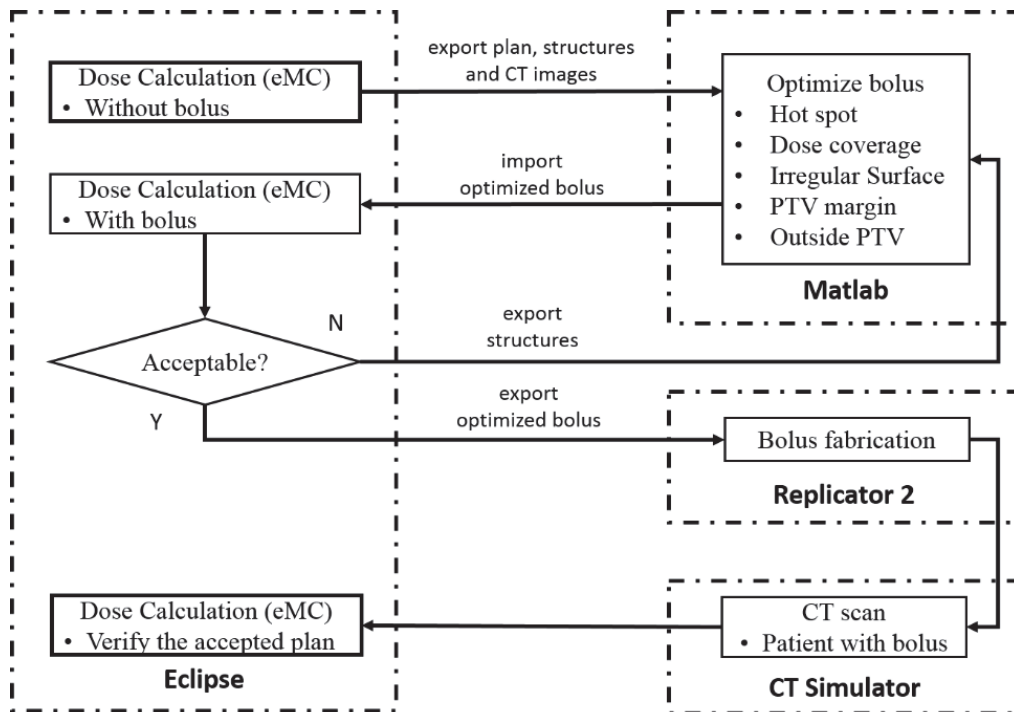
Figure 3.1 Bolus design workflow

A graphic user interface accompanies the bolus design algorithm (Figure 3.2). In the 'Dicom Info', the user specifies the file paths for the DICOM CT image data of the patient, the DICOM radiotherapy (RT) structure as well as the DICOM RT plan file. The structure information are selected from menus according to the DICOM RT structure file,

68

and should include those for the PTV, the covering (e.g., 90%) isodose structure, the bolus itself, and the hot-spot structure (where required). The default bolus material and the grid size are PLA and 2.5 mm, respectively. Once this information is specified, an optimized bolus is designed without further user intervention. The bolus is exported in both DICOM RT format for import into Eclipse and STL format for import by the 3D printer software.
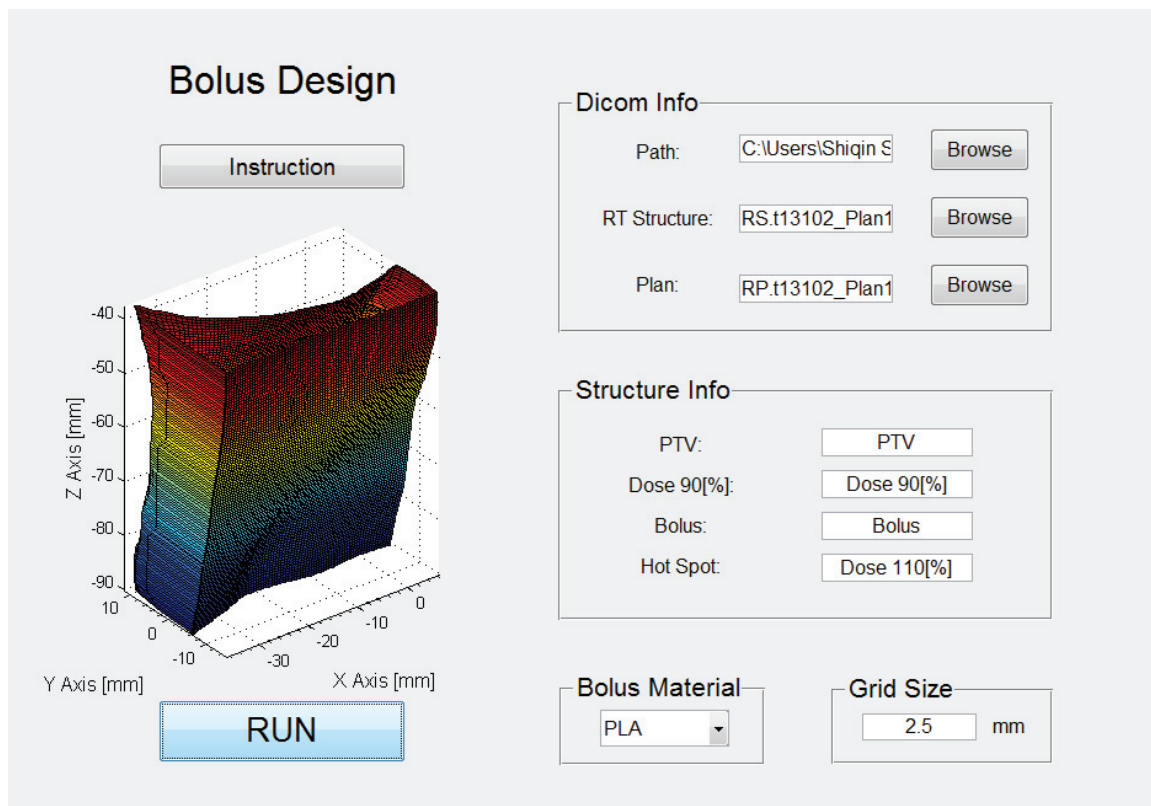
Figure 3.2 Graphic user interface for bolus design

3.3.2 Calculation for Bolus Thickness
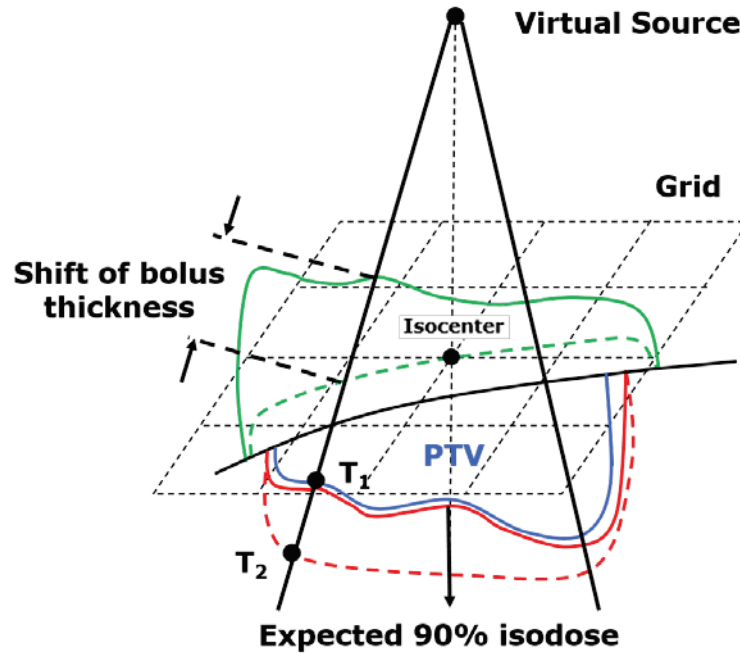
Figure 3.3 Schematic representation of shift of bolus thickness along each ray line. The ray line from the virtual source intersects with distal side of PTV (T_1) and distal part of 90% isodose (T_2). The dashed green line indicates the previous iteration's bolus and the dash red line is the corresponding 90% isodose line which does not yet conform well to the PTV (blue) in this example. The solid green line shows the bolus shape modified according to the change in thickness by shift of thickness (SBT) values and the solid red line represents the expected effect of this change on the dose distribution.

Bolus design (Figure 3.3) is calculated on a grid containing the isocenter and perpendicular to central axis. Bolus thickness is calculated using a grid size of 2.5 mm as a default; however a finer grid can be used for improved precision. Structures are exported from Eclipse, i.e. 'bolus', 'PTV', 'Dose 90%' and 'Hot Spot' (if required), are segmented into distal (i.e. deeper) and proximal (i.e. shallower) surfaces according to the maximum and minimum lateral coordinates. The raw structures are then converted into a triangulated surface which is described by the faces and vertices of the triangles. The 3D-area of consideration is divided into cubes and then the intersections of the surface with the edges of the cubes are determined such that the polygons on the surface that need to

be triangulated thereafter can be acquired. An example of triangulated sphere is shown in Figure 3.4. Ray lines are traced from the virtual source to each point on the grid and extended to the distal side of PTV and 90% isodose surfaces. For ray lines intersecting the PTV, the distance $z_{real} = T_1T_2$ is calculated. The intersections are determined using a fast, minimum storage required ray/triangle intersection method implemented by Tomas Moller and Ben Trumbone[58]. The algorithm is able to determine whether a ray is intersecting a triangulated surface and calculates the intersection of a ray and a triangle in three dimensions, including the 3D coordinates of the intersection and the distance from the origin of the ray to that intersection. Bolus design for ray lines outside of the PTV is addressed by a subsequent operator (see section 3.3.8 below). For water-equivalent materials, the shift of bolus thickness (SBT) at point p is equal to z_{real} due to the homogeneity of the phantom. Note that because the initial plan is calculated with no bolus and the requirement is complete coverage of the PTV by the 90% dose surface, all SBT_p values will be positive in the first iteration. In subsequent iterations, SBT_p values are used to adjust the design of the bolus resulting from the previous iteration (Figure 3.5a).
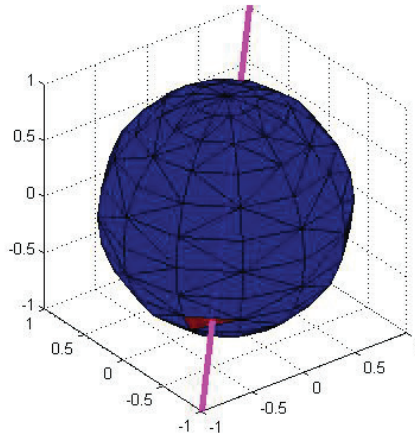
Figure 3.4 Schematic illustration of ray line intersection algorithm shows a line segment intersecting a sphere. For references, the sphere with triangulated surface is in blue, the line segment is in magenta and the intersected triangle is in red.

3.3.3 Inhomogeneity correction with the incorporation of CT data

Patients typically contain tissue inhomogeneities, e.g., lung or bone, necessitating correction of SBT_p values, which can be obtained with the ratio of linear collision stopping power relative to that of water and the ratio of linear scattering power at each point in the patient[43]. Such information is adequately supplied by CT data of the patient. Since linear collision stopping power of the medium to that of water is assumed to be independent of electron energy and related to the CT number, z_{real} can be converted to an effective distance z_{eff} using the coefficient of equivalent thickness (CET) method[59]. The effective shift of bolus thickness (SBT) of a certain point p on the grid is given by

$$SBT_p = \frac{1}{CET(Bolus)} \int_{T2}^{T1} CET(z) \, dz \qquad \text{Eq. 3.1}$$

where CET(z) is the density at point z relative to that of water. The density is obtained from the CT Hounsfield Unit (HU) to density look up table in the planning system which in turn was obtained during eMC commissioning from a HU calibration phantom (Catphan, the Phantom Laboratory, Salem, NY). The accuracy of the CET method has

been discussed in section 2.7.2; the approach is useful for simple geometries but the accuracy is compromised in the presence of complex inhomogeneities[38]. Each iteration of the algorithm includes calculation by the eMC algorithm such that subsequent modifications are based on an accurate dose distribution.

3.3.4 Smoothing for Hot Spots

While the calculation of SBT_p values largely improves conformity of the 90% isodose surface, it does not address secondary effects caused by lateral electron scatter, such as regional hot or cold spots or the effect of irregular bolus surface. Separate regional modulation operators were developed to address i) hot spots in the PTV, ii) under coverage, iii) irregular bolus surface, iv) coverage at the PTV margin and v) extension of the bolus beyond the PTV. These operators are applied sequentially; however, we reiterate that the dose calculation is performed only by the eMC algorithm in the planning system. Three of the operators (i-iii) involve regional smoothing. In these cases, the SBT matrix is segmented into region of interest containing points p where modulation is required, neighboring points q that are used to smooth p, and points outside of the region of interest (Figure 3.6). Three smoothing operators are used according to the application:

$$SB_p = \begin{cases} RM(p,q,SF,Mode1) = \dfrac{0+\Sigma_{r_{pq}<SF}\ SBT_q exp\ (-r_{pq}^2/2SF^2)}{1+\Sigma_{r_{pq}<SF}\ exp\ (-r_{pq}^2/2SF^2)} \\[4mm] RM(p,q,SF,Mode2) = \dfrac{SBT_p+\Sigma_{r_{pq}<SF}\ SBT_q exp\ (-r_{pq}^2/2SF^2)}{1+\Sigma_{r_{pq}<SF}\ exp\ (-r_{pq}^2/2SF^2)} \end{cases} \text{Eq. 3.2}$$

where r_{pq} is the distance between p and q, and SF(mm) is the smoothing factor, controlling the width of smoothing region and smooth level (i.e. 5, 10, 20 mm for low, medium and high).
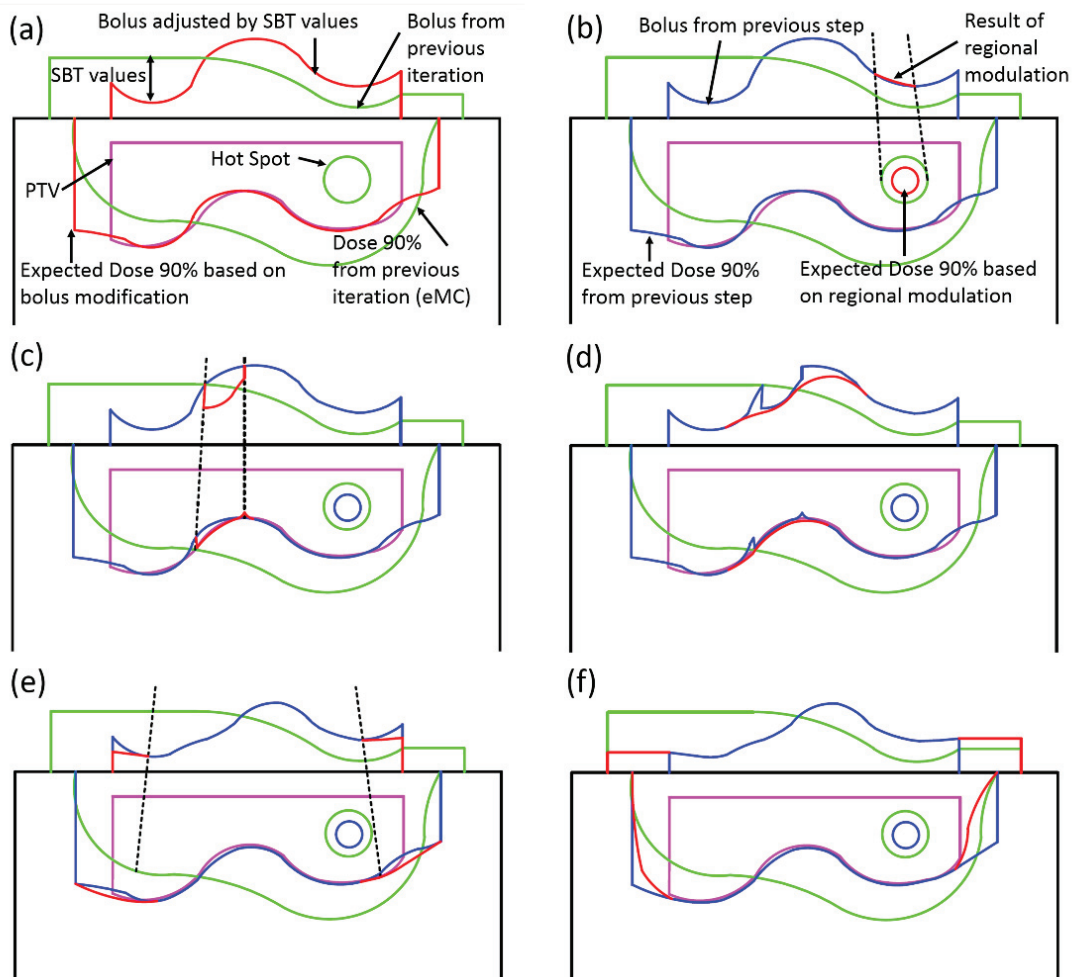
Figure 3.5 Schematic representation of bolus design algorithm after first iteration. The green lines indicate the previous iteration's bolus and corresponding 90% isodose line which does not yet conform well to the PTV (magenta) in this example. The red lines show the bolus shape modified by the current step (a-f), i.e., change in thickness by SBT value or a regional modulation operator as well as the effect of this change on the dose distribution. For reference, blue lines denote the bolus shape and 90% isodose line from the previous step. Hot spots are indicated as circles. The individual steps are: (a) estimation of the bolus thickness based on SBT values, (b) smoothing for hot spots, (c) smoothing for dose coverage, (d) smoothing for surface irregularity, (e) adjustment at PTV margin and (f) extension outside PTV.
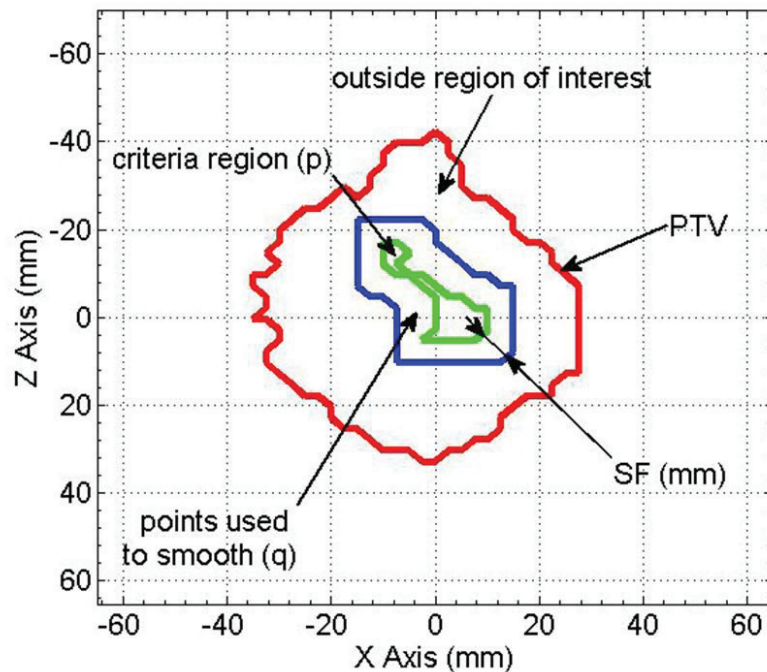
Figure 3.6 Schematic representation of regions involved in smoothing, e.g. to alleviate a hot spot. The red line shows the projection of the PTV onto the calculation plane. The green line denotes the region of interest satisfying the hot spot criterion and containing points p that will be adjusted. Points q between the blue and green lines are included in the smoothing operation but are not adjusted

The first modulation operator aims to alleviate the hot spots that exist within the distribution after the previous iteration of eMC dose calculation (Figure 3.5b). No smoothing is required if maximum dose is less than 110% of the prescription dose, otherwise the hot spot region is projected to the SBT plane and smoothed. RM(Mode 1) is chosen here since the original SBT value in this criteria region may differ appreciably compared to the surroundings.

3.3.5 Smoothing for Coverage

Although the calculation of SBT values aims to provide full coverage by the 90% isodose surface, accurate eMC calculation following bolus design may reveal under coverage in certain regions of the PTV. In these regions, SBT values will be negative, i.e.

to decrease bolus thickness. However testing of the effect of SBT adjustment alone revealed that the bolus thinning must be extended somewhat beyond the region defined by the projection of the under dosed area, otherwise there will be a gradient at the intersection of positive and negative SBT and thus result in local hot spots. Accordingly, negative SBT values in the region of interest are retained while surrounding values are smoothed (see Figure 3.5c). RM(Mode 2) is invoked here, which will always increase target coverage since all affected points will assume negative values following the operation. Due to practical considerations, during this operation the thickness of the bolus will not be reduced below a minimum value of 5 mm, to prevent discontinuity of the printed bolus, or failure during fabrication.

3.3.6 Smoothing for Irregular Surface

Following the previous operations, discontinuities may be present at the boundaries of regions of interest, causing dose inhomogeneity similar to that shown in the example of Figure 2.4. Surface irregularities are identified by using a gradient threshold criterion equal to two times of the mean value of gradient magnitude over the whole calculation grid, and smoothed using RM(Mode 2) (Figure 3.5d).

3.3.7 Adjustment at PTV margin

Relative to more central regions, the edge of the PTV receives less scattered radiation dose simply due to collimation by the electron applicator. To remedy underdosing in this region, a region of interest is defined as a 10 mm wide border inside of the projection of the PTV onto the SBT matrix (Figure 3.5e). A function, which provided continuous change of the SBT value based on the shape of Gaussian distribution, is applied to reduce bolus thickness according to:

$$SBT_p = \begin{cases} SBT_p \times \left(1 - KerfMA\left(\max\left(K1 - r_{pm}, 0\right)\right)\right), if\ SBT_p > 0 \\ SBT_p \times \left(1 + KerfMA\left(\max\left(K1 - r_{pm}, 0\right)\right)\right), if\ SBT_p < 0 \end{cases} \qquad \text{Eq. 3.3}$$

where values are adjusted along radial lines from the central axis. The point m exists on

the inner boundary of the region of interest, p exists within the region of interest, r_{pm} is

the distance between p and m, $KerfMA(x) = \exp\left(-\dfrac{x^2}{2\ sigma^2}\right)$ and

$K1 = \sqrt{-2\ln(0.01)\ sigma^2}$, i.e., the distance over which KerfMA(x) increases from

0.01 to 1 (Figure 3.7). Both positive and negative SBT values are decreased with the

operation of the function, while its effect to the point is related to the distance to the

margin r_{pm}. In practice we determined that effective values of sigma must be related to

beam profile, increasing with both energy and applicator dimension.

In this work and for coding simplicity, an approximation of $sigma =$

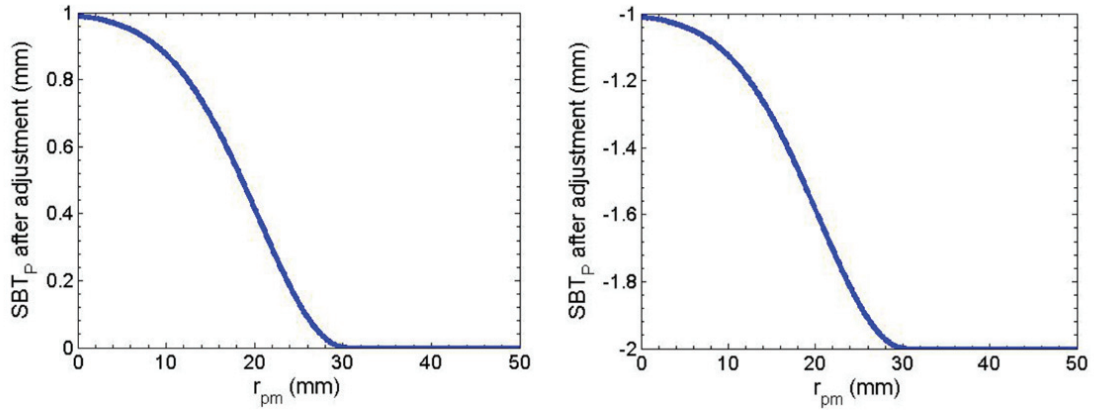$\sqrt{Energy\ (MeV) \times Applicator(cm)}$ is employed.

Figure 3.7 Diagrammatic representation of equation 3.3 using $sigma = 10$ when SBT_p before the adjustment is assigned to 1 (left) and -1 (right)

3.3.8 Shift outside the PTV

The area corresponding to all ray lines between the edge of the PTV and a distance 1.0 cm beyond the electron aperture are subject to this operator. In this region bolus thicknesses are simply extruded, i.e.:

$$SBT_p = SBT_n \qquad\qquad \text{Eq. 3.4}$$

where n is the intersection of PTV contour and line from p to the projection of central axis (Figure 3.5f).

3.4 Bolus Fabrication

The final modulated bolus is converted into a STL file, which can be provided as input to the 3D printer for fabrication of the bolus using PLA. Cross-hairs are added to the bolus surface for the convenience of alignment on the patient (Figure 3.8). A set of parameters selectable within the 3D printer software (Makerware, MakerBot Industries) are relevant to the printing quality and method and define a print profile. The 'sparseInfillPattern' option is set to 'linear', which determines the infill pattern. The layer height controls the thickness of deposited PLA in each layer of printing and largely determines printing speed; low, standard and high quality print profiles correspond to 0.3, 0.2 and 0.1 mm heights, respectively, while the standard profile is recommended in most cases. The bolus model is placed such that a flat surface is in contact with the build plate (Figure 3.9). '100% infill' is used to make the bolus completely solid (otherwise the bolus will be filled with, e.g., a honeycomb structure). The CT value of manufactured bolus was measured to be 130 ± 20 HU, which corresponds to a density of 1.119 ± 0.012 g/cm^3.
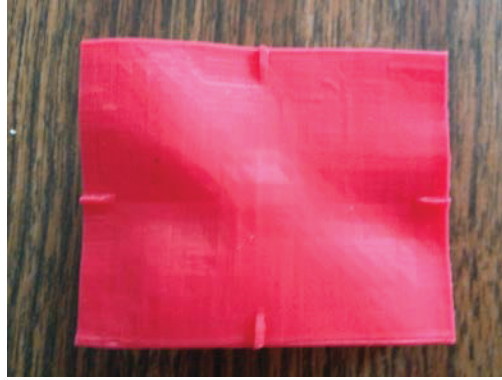
Figure 3.8 Photo showing cross-hairs on the bolus surface
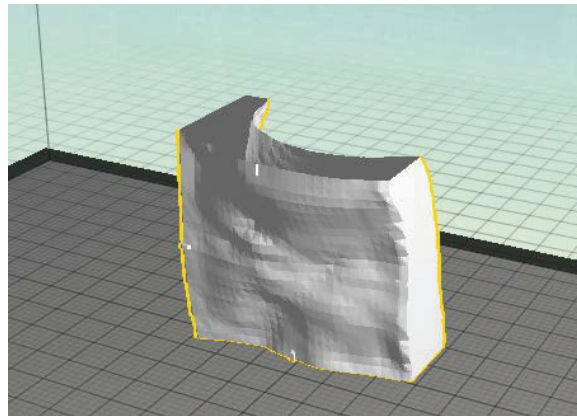
Figure 3.9 Schematic representation of placement for bolus printing, where a flat surface is in contact with the build plate.

Several challenges were addressed in developing a methodology for 3D printing of electron bolus. In initial attempts, the printed bolus had an uneven bottom such that the edges contracted, losing contact with the build plate, apparently caused by rapid cooling of initial layers of printed PLA. Based on this, we changed the "fanLayer" parameter to 2 such that the first two layers were put down without the active cooling fan being turned on, thus improving the adhesion of the first printed layers to the build plate and decreasing the possibility of warping. Alternate measures that were explored (which failed) included:

- Printing the model with the widest surface against the build plate instead of printing with the model on its edge. However, this exacerbated the warp issue.

- Re-leveling the build platform, and adjusting the distance between the build plate and the nozzle. This has the effect of 'pressing' the printed PLA into narrower traces (with decreased distance), or creating printed patterns that are thicker and less consistent (increased distance). Neither adjustment ameliorated the warping issue at the edges of the printed bolus.

- A hypothesis regarding the cause of the warping was inconsistency of the botsteps, i.e., distance travelled by the nozzle per pulse to the stepper motors, which control the jog of nozzle in each axis. However, following calibration of botsteps for all three axes and replacing XYZ motor cable, the warp issue remained.

- Increasing the number of shells (i.e. the outer covering of the model) from 2 to 500 (an arbitrarily high number), so that the print will consist entirely of shells. It was hoped that this change would enhance the solidity of the model while maintaining the 100% filling. Nevertheless, no obvious improvement was observed and this change significantly increased the printing time.

3.5 Dosimetric Verification

A series of measurements were conducted to acquire the CET value of manufactured bolus by replacing the solid water phantom by PLA slabs of varying thickness. CET value of bolus is given by:

$$z_{eff} - z_{real} = [CET(bolus) - 1] \times t \qquad \text{Eq. 3.5}$$

where t is the thickness of bolus slab. The shift $z_{eff} - z_{real}$ was determined by matching the location of minimum of chi-square (x^2) of two PDD curves[60], i.e. with/without PLA slabs added. PDD curves were measured with 10×10 cm^2 field size and 100 cm SSD using 6, 9, 12 and 16 MeV electron beams on a Varian 2100EX linear accelerator (Varian Medical, Inc., Palo Alto, CA). The Semiflex (31010, PTW, Freiburg, DE) ionization chamber and Exradin parallel plate chamber (A11, Standard Imaging, Inc., Middleton, WI) were used to detect the radiation. Three $12 \times 12 \times 1$ cm^3 PLA slabs were printed such that separate PDDs could be measured with either PLA or Solid Water comprising the superficial 3 cm of the phantom (Figure 3.10). The results of the same measurements were also compared to eMC calculations in the planning system.

Figure 3.10 Dosimetric verification of bolus material. PLA slabs replaced the superficial 1 cm of solid water.

3.6 Quality Assurance

As explained in Figure 3.1, after the bolus fabrication, a CT scan of patient (or phantom) with bolus added is acquired. The reasons for this step are i) to verify adequate fitting of the manufactured bolus and ii) to allow calculation of the final dose distribution, i.e. in case there are differences between the geometry of the calculated and

manufactured bolus. The same plan used for bolus optimization is applied to the CT image set with the manufactured bolus. If air gaps exist between the bolus and the patient, the effects of these can be assessed in this final calculation. In this section, we assessed the 2D agreement between the calculated doses for the idealized bolus relative to that for the manufactured bolus using the gamma evaluation method[61]. The gamma values are calculated in OmniPro I'mRT (IBA Dosimetry, Bartlett, TN) using acceptance criteria of 3% and 3 mm.

Chapter 4 RESULTS

4.1 Determination of CET Value

Figure 4.1a shows the shift $z_{eff} - z_{real}$ determined by the differences of CET value between PLA and water according to the measured PDD curves using ionization chamber. No obvious energy dependence is observed (Figure 4.1b). Therefore, these data are averaged over the four energies to provide a value for the measured CET of 1.13 ± 0.01. The uncertainty mainly results from the minimum thickness of solid water available for the measurement, i.e. 2 mm. This CET value agrees well with the calculated value 1.119 given by the density of the PLA. The measurement using a parallel plate chamber yielded the same result as that for cylindrical chamber, while the eMC simulation gives a prediction of 1.08 ± 0.01. The discrepancy is not expected to produce clinically significant errors in the resulting dose distribution. The coincidence of simulated PDD and measured PDD is shown in Figure 4.2.
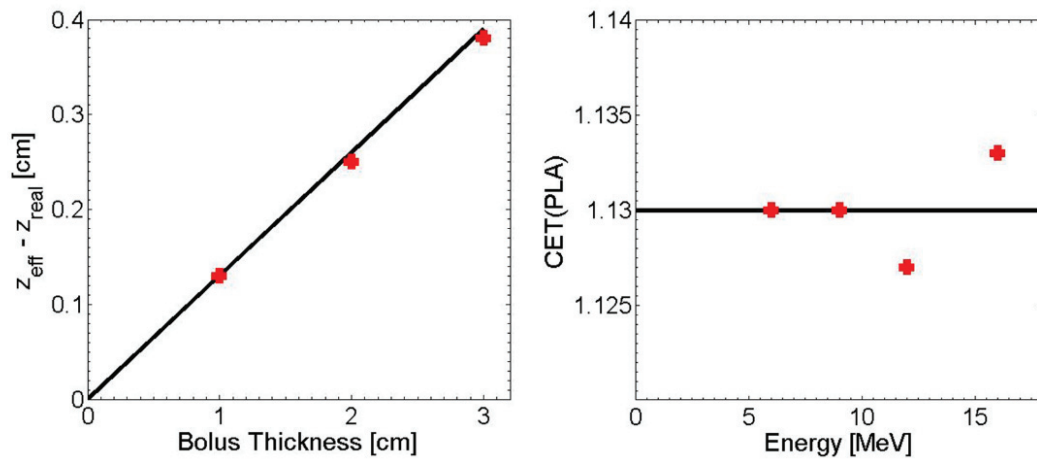

Figure 4.1 Measured shift $z_{eff} - z_{real}$ of PDD curves for a 12 MeV electron beam incident on a solid water phantom for 0, 1, 2 and 3 cm thicknesses of Solid Water replaced by PLA slabs (left). CET value of PLA versus incident energy of 6, 9, 12 and 16 MeV (right).
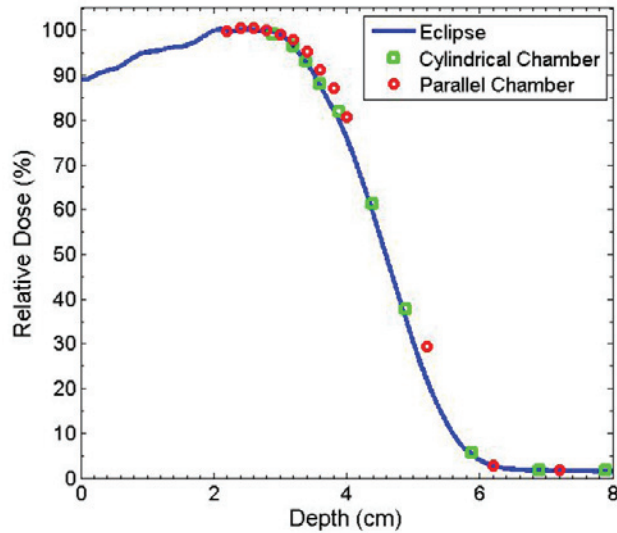
Figure 4.2 PDD curves for 12 MeV electron beam with 2 cm solid water replaced by PLA slabs

4.2 Bolus optimization and bolus fitting

4.2.1 Wedge target volume with heterogeneity

Several simulations were used to evaluate the algorithm. The first example included a wedge shaped PTV in a water phantom. As shown in Figure 4.3a, two inhomogeneity regions, assigned CT values of bone and air respectively, were added to the geometry distal to the PTV. A 12 MeV electron beam and 10×10 cm^2 applicator were used. With no bolus, the perturbation of the dose by the inhomogeneities as calculated by eMC, is apparent. As shown in Figure 4.3b, after one iteration of bolus optimization, the 90% isodose was almost symmetric about central axis with the 0 HU bolus, though deficiencies in conformity persist particularly proximal to the air inhomogeneity. This likely arises from the simplicity of the scaling provided by the CET method. However, a second iteration of the optimization further improves the conformity of the 90% isodose to the target volume. In practice, even in the presence of tissue

84

inhomogeneities, a conformal dose distribution usually can be achieved in one or two iterations of the algorithm.

In this example, while dose conformity increases, optimization of the bolus surface produced an inadvertent hot spot in the central volume of the PTV (Figure 4.3b and c). This was caused by the increase of electron scatter toward the midline by the thicker regions of the optimized bolus. This indicates that the conformity of the 90% isodose line to the target volume and the uniformity of dose distribution may not be achieved simultaneously. Figure 4.4 demonstrates that with successive iterations of the algorithm, the coverage of the PTV is not compromised while the sparing of distal regions (e.g. contoured bone and air volumes in this example) improves. Here, the maximum dose decreases from 98.8% to 79.5% and from 106.3% to 80.4%, for the bone and air inhomogeneities, respectively.
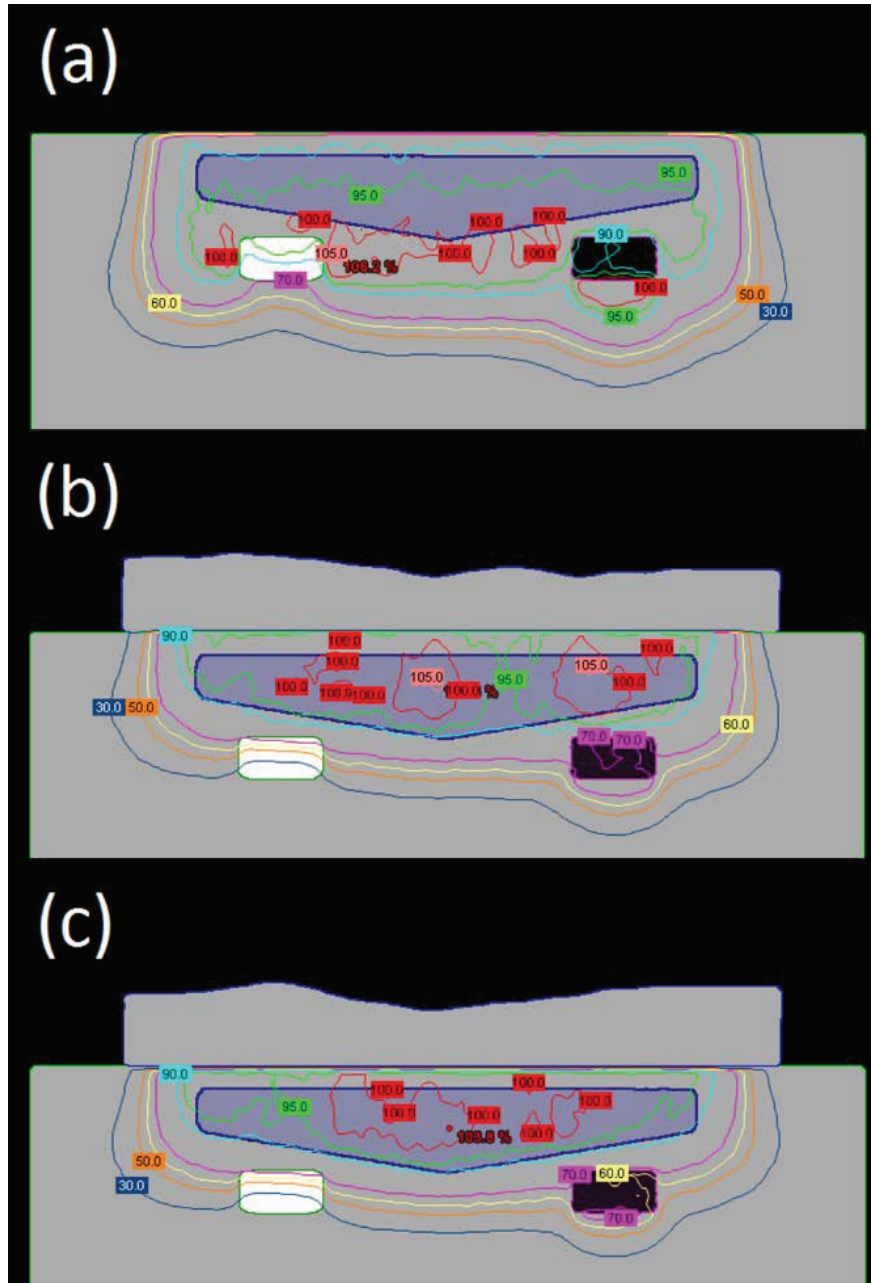
Figure 4.3 (a) Wedge-shaped PTV case where a $20 \times 20 \times 20$ cm^3 water phantom irradiated by 12 MeV with no bolus. Following (b) one and (c) two iterations of bolus optimization.
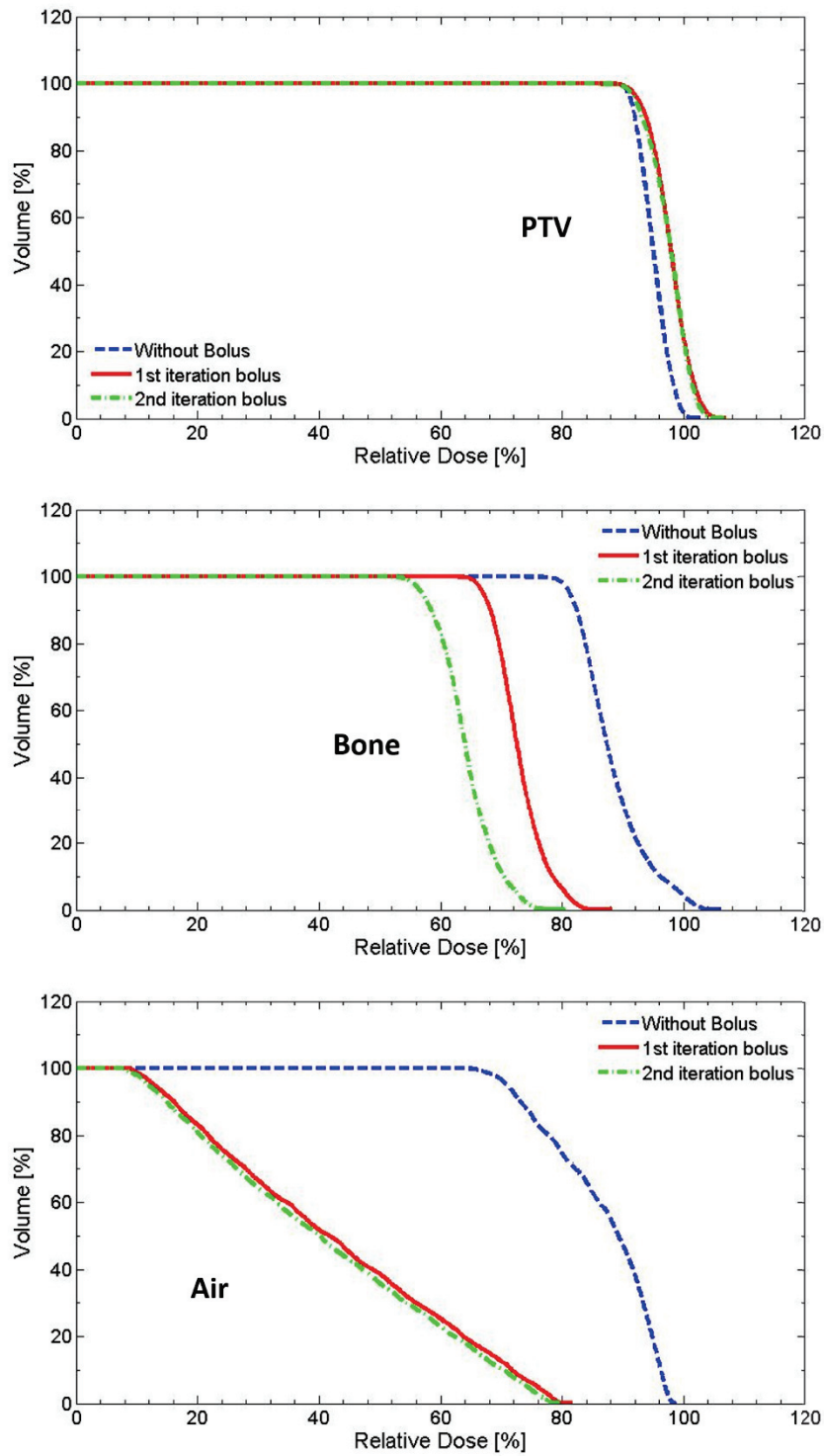
Figure 4.4 Cumulative DVH for the wedge PTV (top), bone slab (middle) and air cavity (bottom).

4.2.2 Foot Phantom

For a more realistic geometry, a foot phantom made of plaster was manufactured (Figure 4.5). This provides an anatomy that is reasonably complex with regard to the surface curvature, with a simulated PTV at the proximal aspect of the metatarsals. The initial plan used a 9 MeV electron beam with a 6×6 cm^2 applicator and 1 cm thick uniform bolus to achieve full coverage of the PTV (Figure 4.6a). The CT value of this bolus was assigned to 160 HU. Figure 10c shows the result of one iteration of bolus optimization. DVHs of the conventional (uniform bolus) and MERT plans are shown in Figure 4.7. The MERT plan gives 98.4% PTV coverage by the 90% dose level, with a maximum dose of 104.7%. This demonstrates the possibility of good conformity of the prescription dose surface while maintaining reasonable dose homogeneity.

Figure 4.5 Picture of foot phantom with bolus added on the surface

The printed bolus placed on the foot phantom was shown in Figure 4.5. We observed good agreement between dose distributions produced with the calculated and manufactured boluses (Figure 4.6b and c). Between 140 and 200 minutes were required to print the bolus for low and standard print profiles, respectively. Improved fitting and small air gaps between bolus and phantom surface were observed with the standard

profile and dose distributions were minimally affected. Gamma comparison (3%/5mm criteria) of dose distributions using planned bolus and fabricated bolus is displayed in Figure 4.8, indicating the discrepancies between the plans were acceptable. The high gamma region was attributed to the fact that Eclipse is unable to calculate the dose in a synthetic bolus, since the synthetic bolus is defined as a support structure with a density overrides.

Figure 4.6 Isodose plot of (a) conventional plan using 1 cm bolus, (b) MERT plan using optimized bolus and (c) MERT verification plan using bolus printed by the standard print profiles.

Figure 4.7 Cumulative DVH for PTV in the foot phantom using no bolus (conventional plan) planned bolus (MERT) and fabricated bolus (Verification).
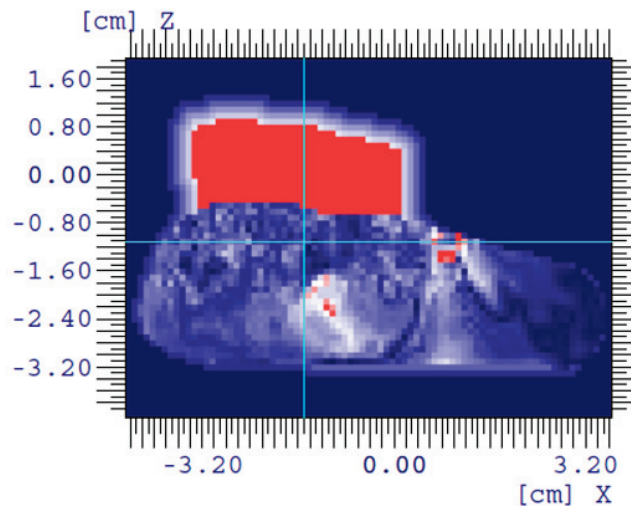
Figure 4.8 Gamma comparison of MERT using planned bolus and fabricated bolus for foot phantom.

4.2.3 Head Phantom

A head phantom case was chosen to provide a second assessment of the algorithm in addressing a realistic patient geometry. A simulated PTV was contoured in the head phantom (RANDO Phantoms, the Phantom Laboratory, Salem, NY) (Figure 4.9). The PTV was irradiated using a 9 MeV electron beam and 10×10 cm^2 applicator

incident with a gantry angle of 30 degrees. Note that the 'eyes' serve as distal organs at risk (despite their unrealistic due to the embedding of an actual skull within a tissue substitute mold to create the phantom). To represent a 'standard' approach, a 160 HU bolus was added to make an approximately flat surface (Figure 4.10a). The dose distribution of the initial and MERT plans are shown in Figure 4.10a and b, respectively. For the MERT plan, 90% dose covers 99.7% PTV and the mean dose for the left eye and left lens decrease from 41.7% to 23.1% and 83.3% to 62.2%, respectively (Figure 4.11). The fabricated bolus fitted to the surface is visible in Figure 13d. Though a small air gap was observed, the gamma evaluation suggested that the variation caused by air gap did not compromise agreement of the measured dose distribution (Figure 4.12). However, we notice discrepancy in DVH of synthetic bolus plan and printed bolus plan. This is attributed to some imprecision of the co-registration algorithm in Eclipse in co-registering the geometry of small size of lens and eyes. With regard to the occurrence of air gaps, the two phantom simulations likely represent a worst case scenario since both the anthropomorphic phantom and the bolus are composed of hard, non-malleable surfaces.

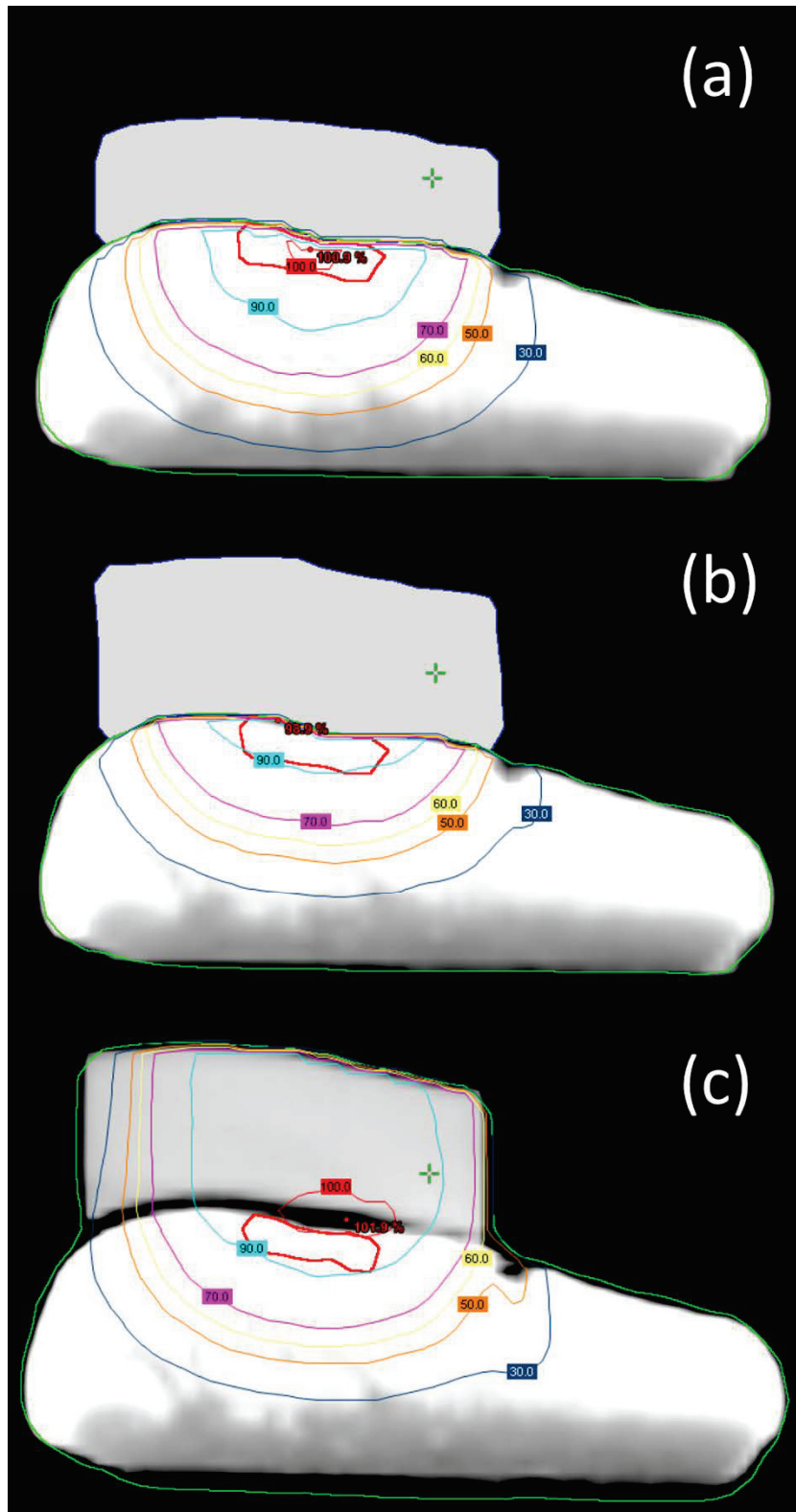Figure 4.9 Picture of head phantom with bolus added on the surface

Figure 4.10 Isodose plot of (a) conventional plan using flat bolus, (b) MERT plan using optimized bolus and (c) MERT verification plan using bolus printed by the standard print profiles.
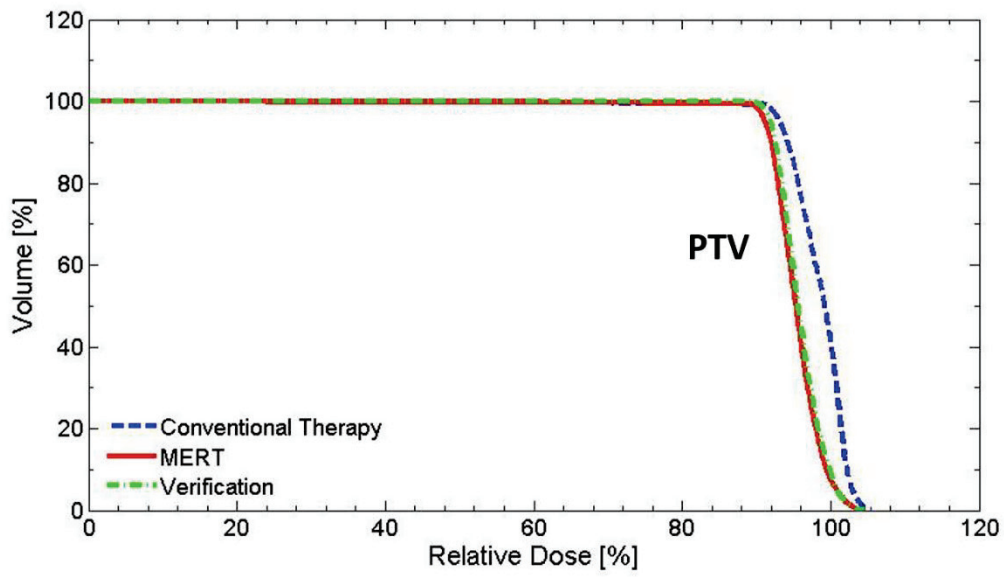
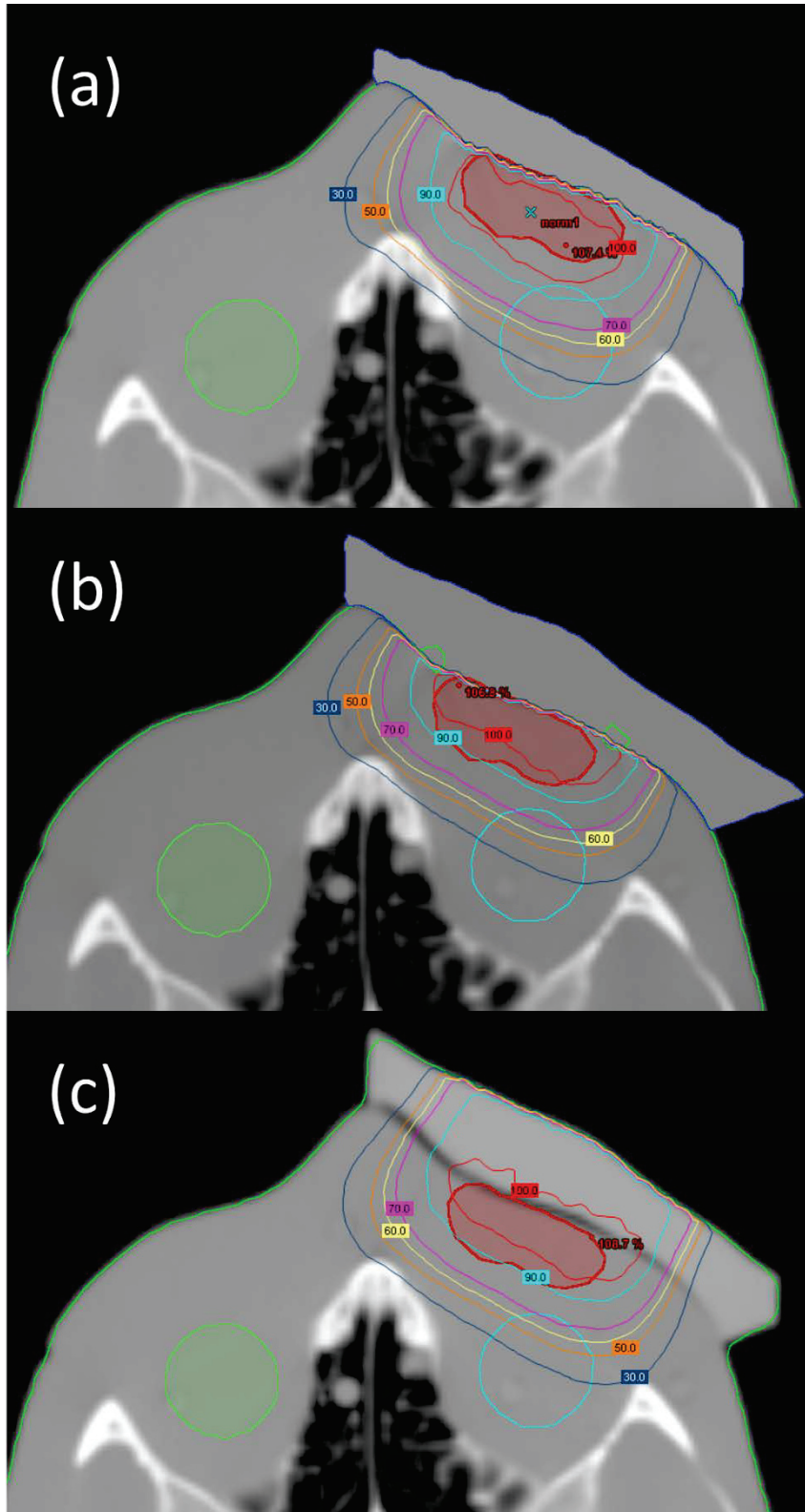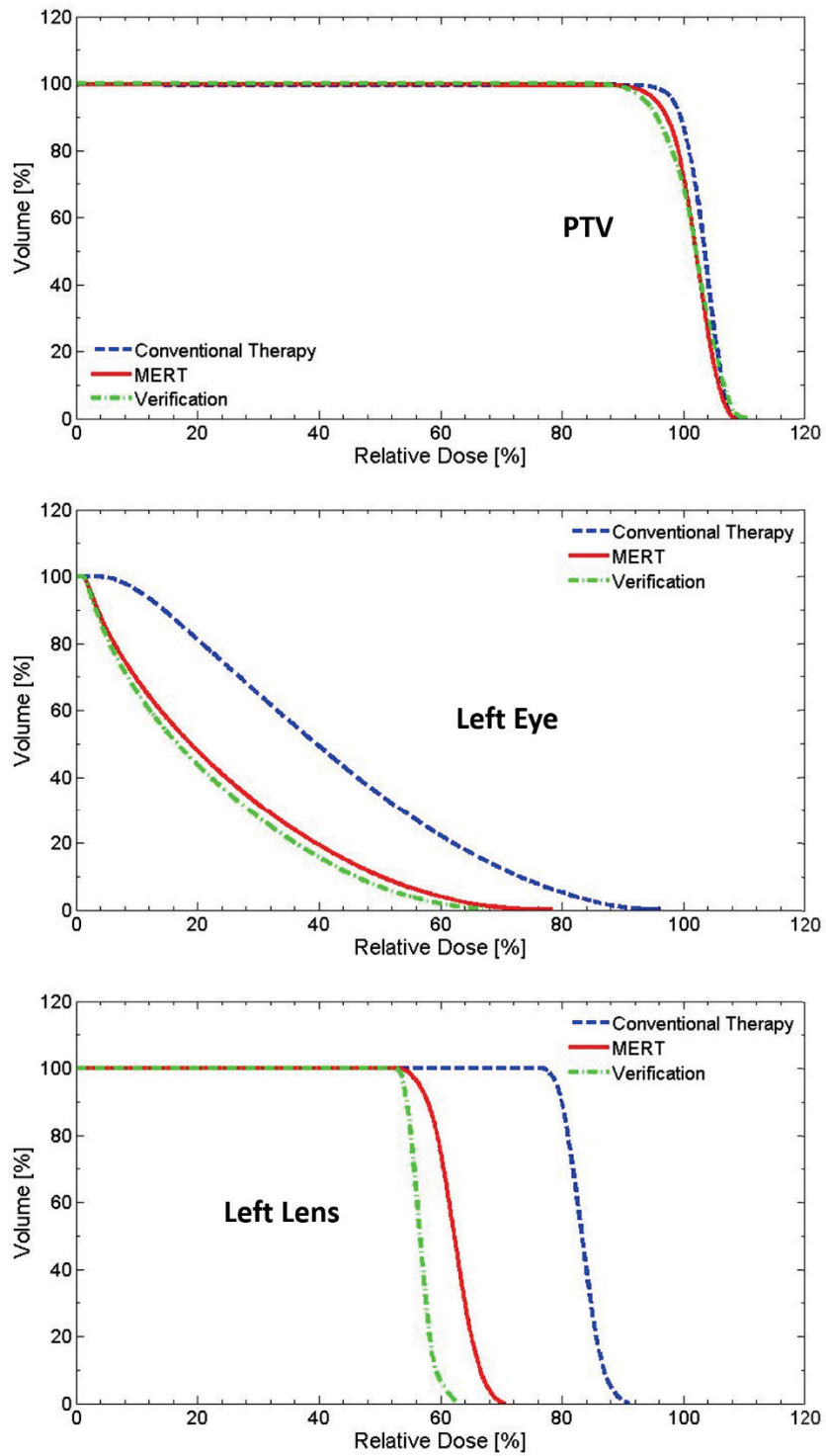Figure 4.11 Cumulative DVH for PTV (top), left eye (middle) and left lens (bottom) for head phantom case
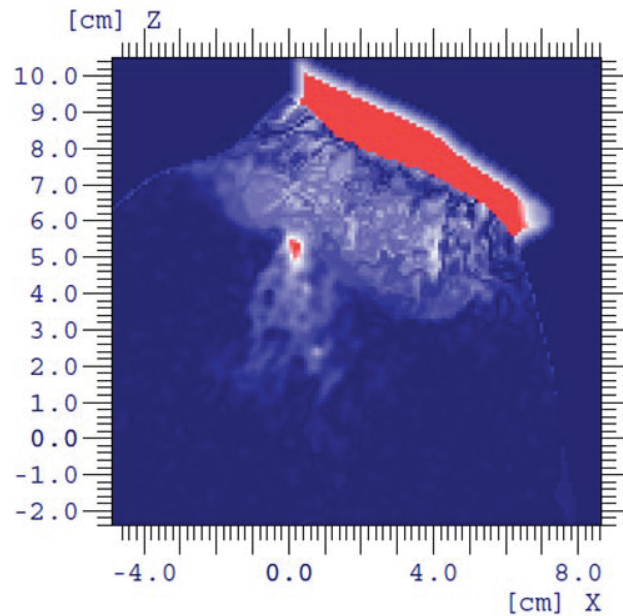
Figure 4.12 Gamma comparison of MERT using planned bolus and fabricated bolus for head phantom

4.2.4 Rhabdomyosarcoma Patient

Figure 4.13 shows an example of optimized bolus for a pediatric patient with a rhabdomyosarcoma tumour proximal to the left kidney and overlapping spine. Due to the depth of the PTV, a 16 MeV electron beam was used. 5040 cGy in 28 fractions was prescribed to the 90% isodose covering the PTV. A 15×15 cm^2 applicator and SSD of 105 cm were used. Figure 4.13a shows the result of three iterations of the bolus optimization algorithm plan, while Figure 4.13b demonstrates the dose distribution that would result from 1 cm thick uniform bolus. Though the dose homogeneity degraded in MERT plan, with a maximum dose of 5710 cGy, 98.1% of PTV was still covered by 90% isodose. The MERT plan allows a reduction of the mean dose of left kidney by 38.2% from 4586.7 to 2834.5 cGy (Figure 4.14), thus almost achieving the tolerance toxicity for kidney, i.e. 2800 cGy. While the 90% dose conformity is excellent for the MERT plan,

95

the shape of the bolus generates electron scatter that produces 110% hot spots in the PTV

(Figure 4.13a).
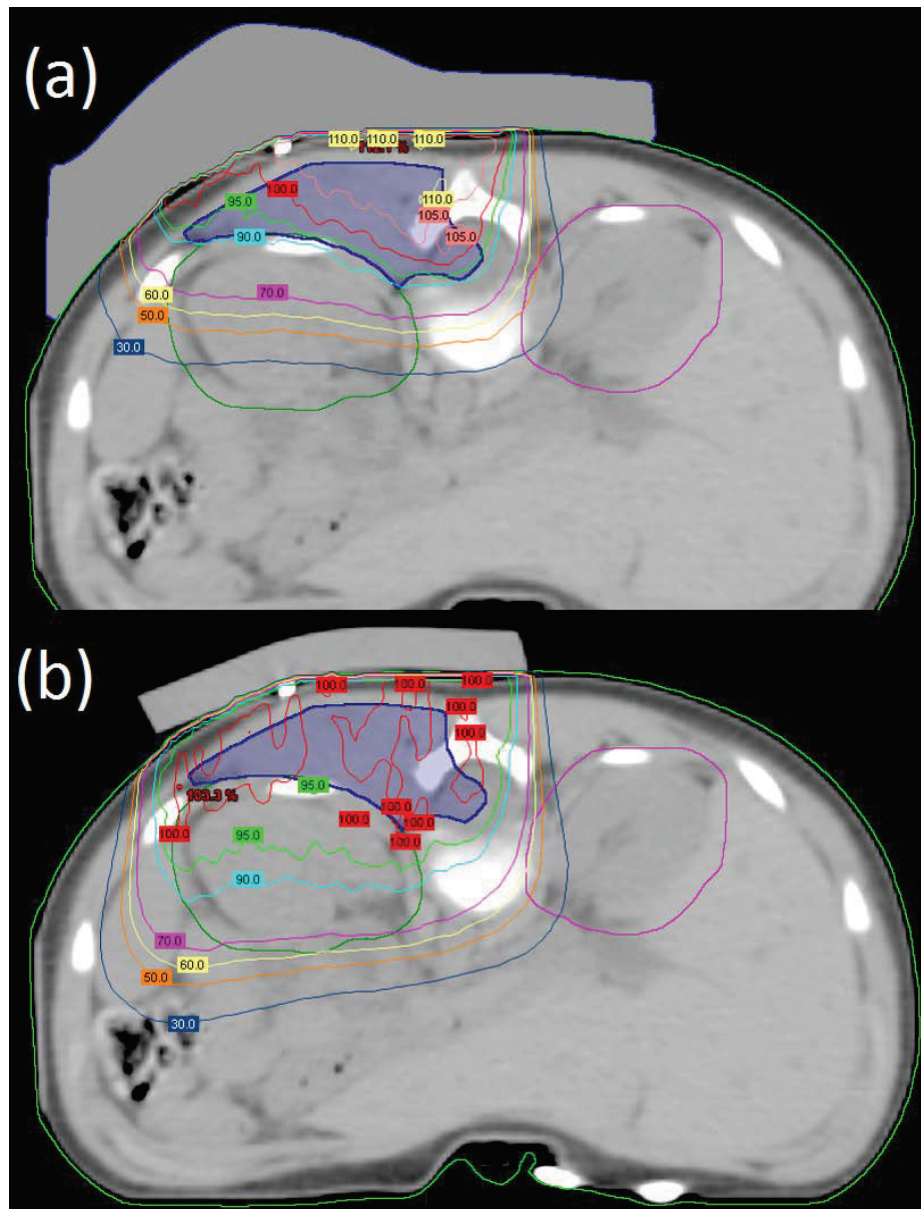
Figure 4.13 (a) Rhabdomyosarcoma patient using MERT with the algorithm applied for three times. (b) Conventional electron therapy with 1 cm custom bolus.
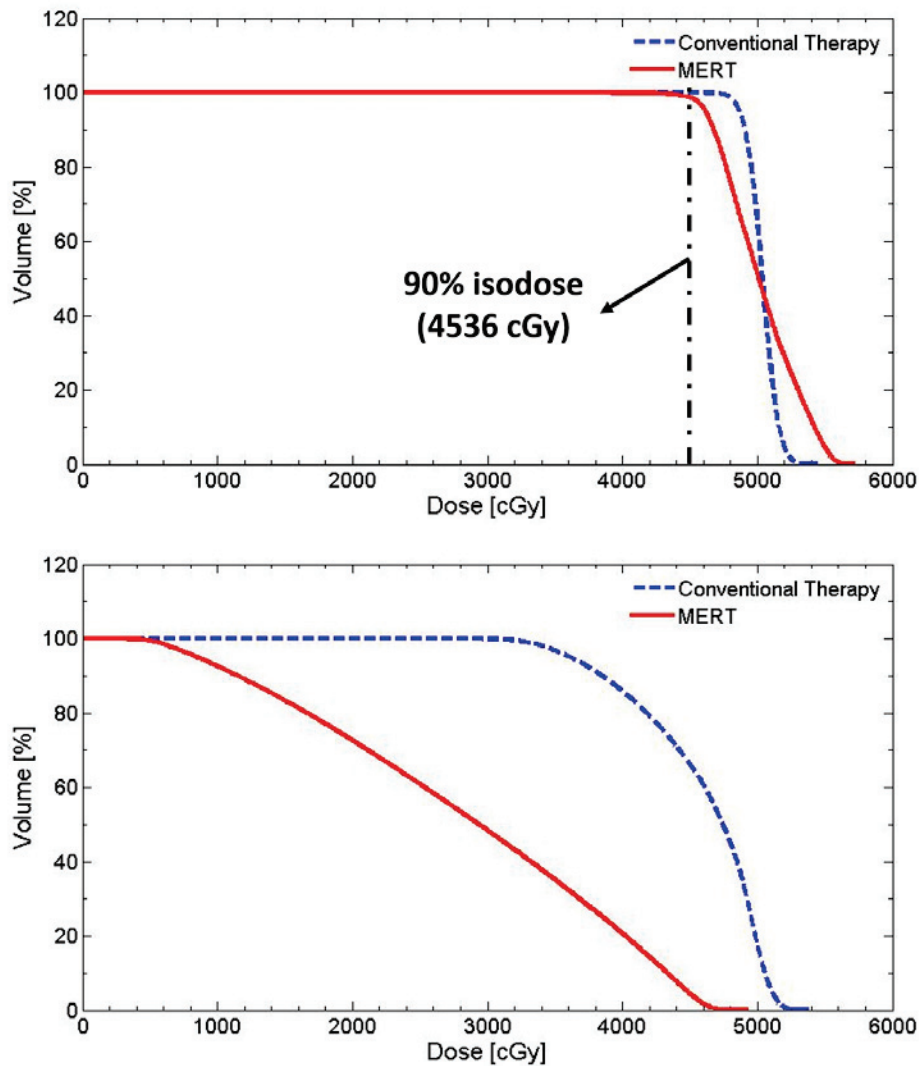
Figure 4.14 Cumulative DVH for PTV (top) and left kidney (bottom) for rhabdomyosarcoma patient

4.2.5 Chest Wall Patients

Two chest wall patients were simulated using MERT, where the goal was to deliver the prescription dose to a PTV derived from the lumpectomy cavity, i.e. a frequent indication for radiation therapy. Patient case #1 has a PTV with relative flat distal side (Figure 4.15a), while an irregular PTV is observed in the patient case #2 (Figure 4.16a). 1100 cGy was prescribed to both patients. In case #1, a 16 MeV electron beam and no bolus were used in the conventional plan; for the second case, the energy of

beam was 12 MeV and a 0.5 cm uniform bolus was added. However, due to the fact that not all part of both PTVs were covered by 90% isodose in both initial plans, the effectiveness of bolus optimization were degraded. The isodose lines for the two MERT plan are shown in Figure 4.15b and Figure 4.16b, respectively. We note that the discontinuities of bolus results from interpolation in Eclipse during the resampling of bolus structure. For the first patient, due to the flatness of the distal side of PTV, conventional therapy results in a plan matching the dosimetric quality of MERT with regard to the conformity, though a small part of PTV under-coverage was improved with MERT. The 90% coverage of PTV increases from 93.0% to 97.1% (Figure 4.17). On the other hand, due to the irregular shape of the PTV in second patient, the conventional therapy was not able to achieve appropriate coverage of PTV (i.e. 89.1%). With the utilization of MERT, the 90% dose coverage of PTV raised to 95.0% (Figure 4.18). In term of OARs, MERT predicted lower doses for both heart and lung in both plans. These two examples here demonstrate that MERT with 3D printed bolus may be used effectively in chest wall treatment, in terms of better target volume coverage at the expense of slightly more dose to the lung and heart.
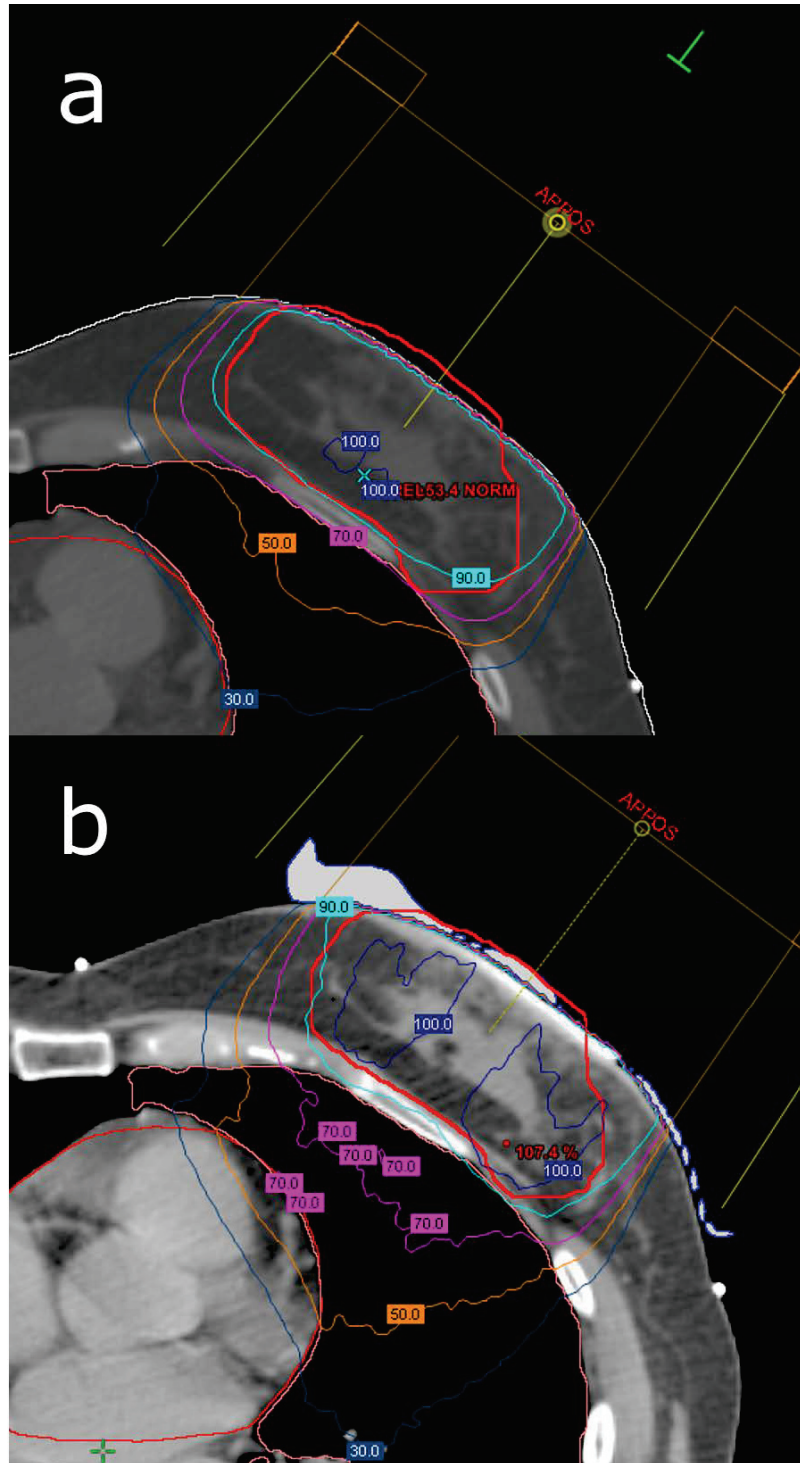
Figure 4.15 Isodose lines of (a) chest wall patient with regular PTV (case #1) using conventional with no bolus. (b) MERT with optimized bolus (Note that the discontinuities of bolus results from interpolation in Eclipse during the resampling of bolus structure). The 90% coverage isodose is shown in light blue.

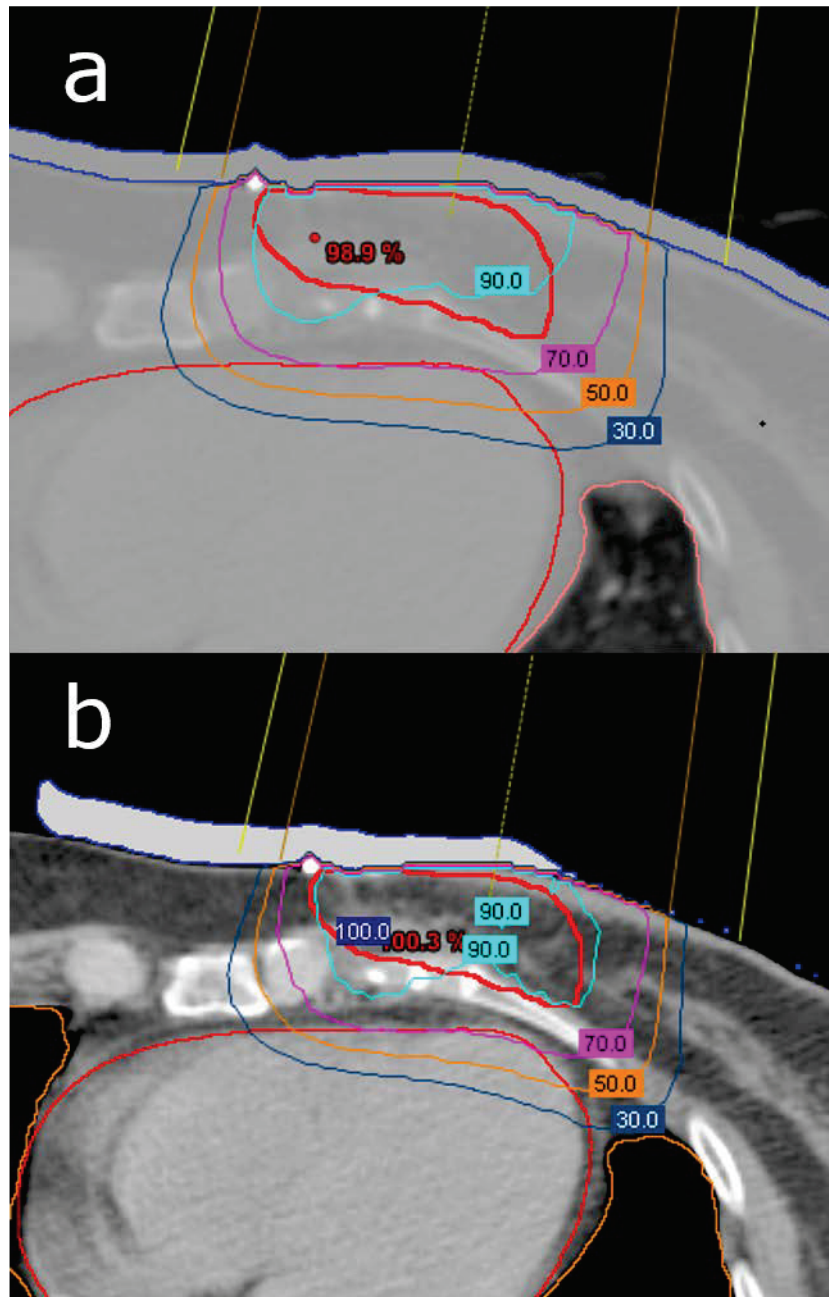Figure 4.16 Isodose lines of (a) chest wall patient with irregular PTV (case #2) using conventional with 0.5 cm uniform bolus. (b) MERT with optimized bolus. The 90% coverage isodose is shown in light blue.
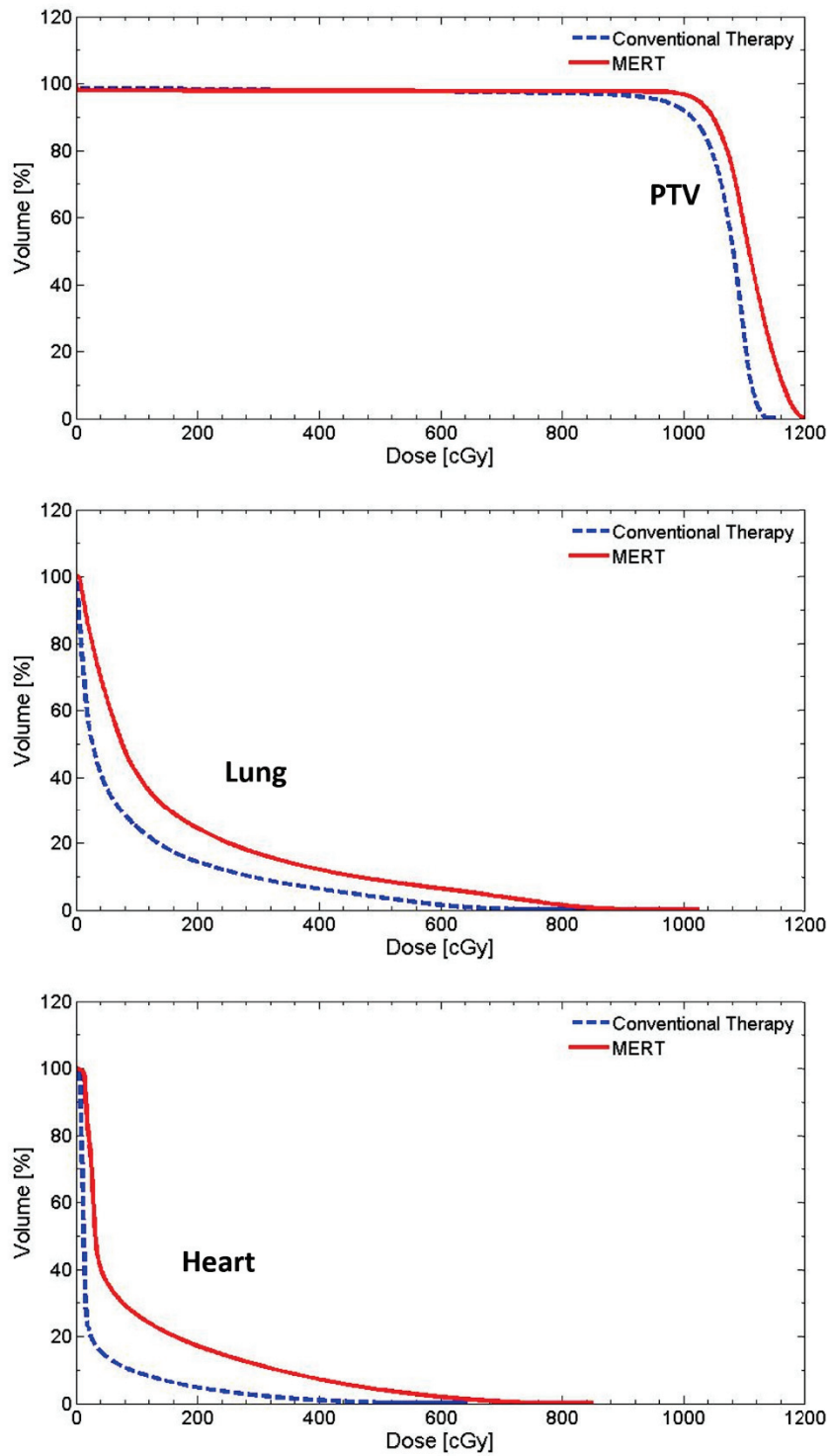
Figure 4.17 Cumulative DVH for PTV (top), lung (middle) and heart (bottom) for chest wall patient case #1.
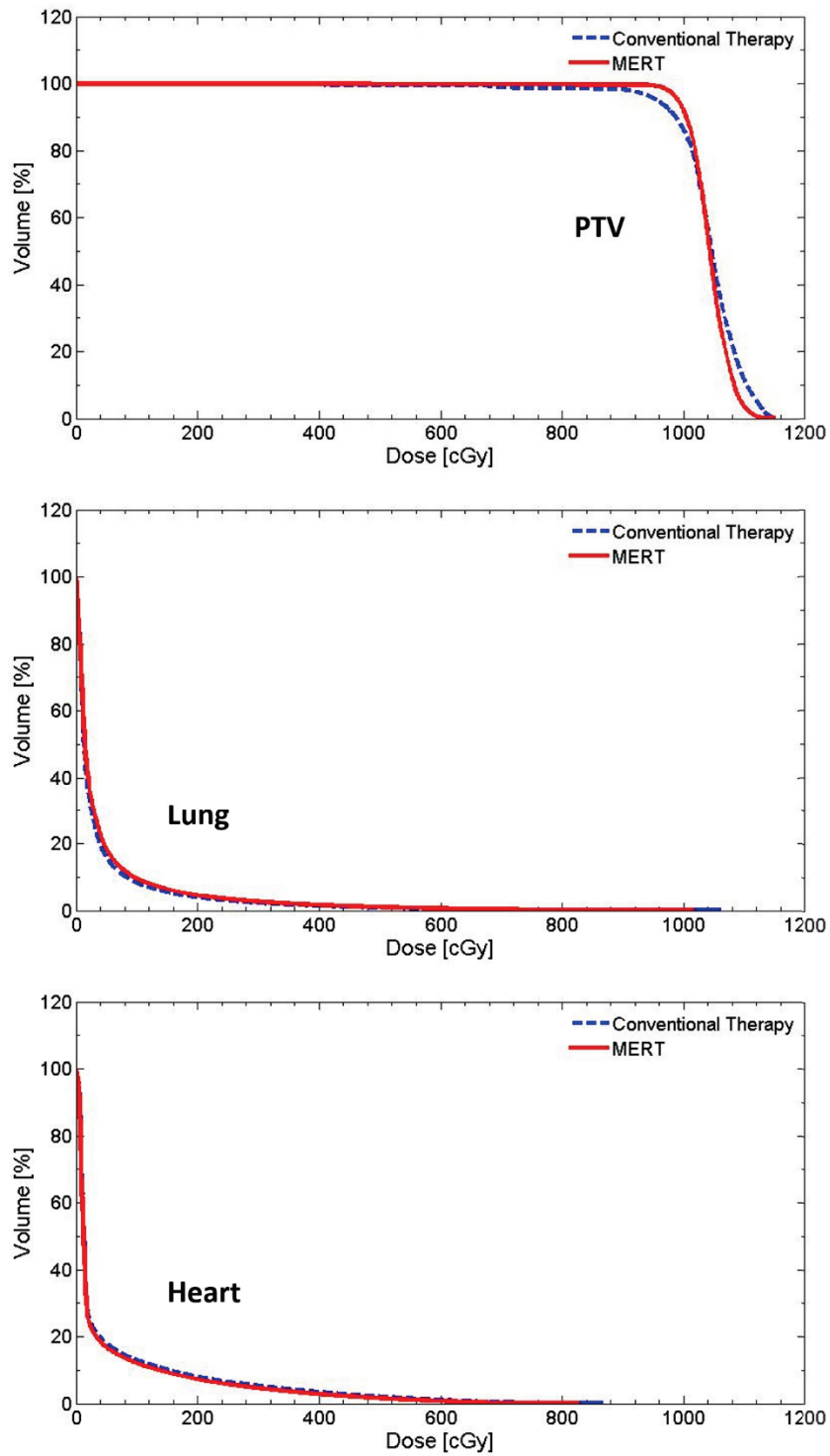
Figure 4.18 Cumulative DVH for PTV (top), lung (middle) and heart (bottom) for chest wall patient case #2.

4.2.6 Basal cell carcinoma (BCC) patient

To evaluate the bolus fitting on a real patient, a basal cell carcinoma (BCC) patient (Figure 4.19) was selected, which provided a quite complex geometry in terms of the surface irregularity. The patient was originally planned with a manually made bolus, i.e. using aquaplast beads to create a custom form. The 3D-printed bolus was contoured by removing the aquaplast bolus from the 3D CT set and adjusting the body contour. Patient consent for a second CT simulation with this customized bolus was obtained by the attending physician for quality assurance purposes. The setup of the bolus along with the patient is shown in Figure 4.20. The fitness was assessed through CT images and compared to that with the manually manufactured one (Figure 4.21). It can be observed that while the manually-produced aquaplast bolus leads to large air gaps between the bolus and patient surface, the printed bolus can effectively narrow these gaps and adequately fill the space behind the pinna. However, due to the fact that the printed bolus was contoured based on the CT images three weeks before the second scan (which means the patient geometry may have changed during the period) and the limited accuracy in contouring the bolus structure in planning system, small air gaps resulted.

Figure 4.19 Photo of BCC aspect of left ear.

Figure 4.20 Photos of 3D-printed bolus (left) and following positioning on the patient (right).

Figure 4.21 CT image of BCC patient with (a) aquaplast bolus and (b) 3D-printed bolus

Chapter 5 DISCUSSIONS

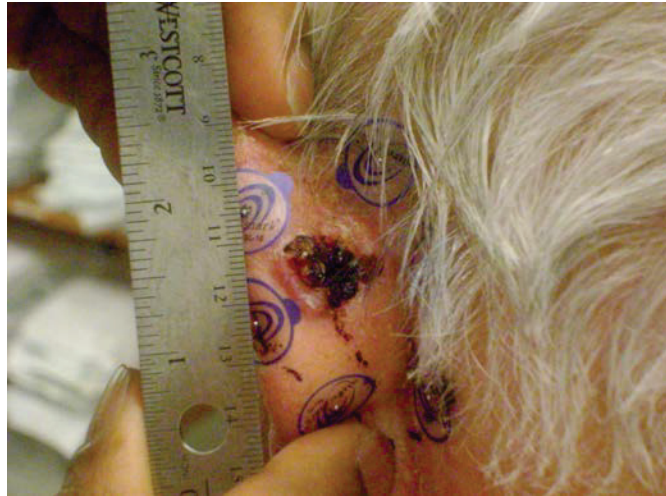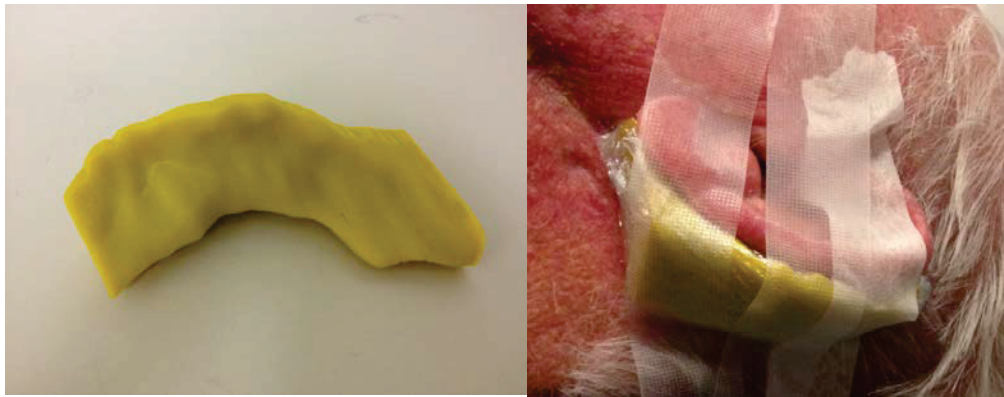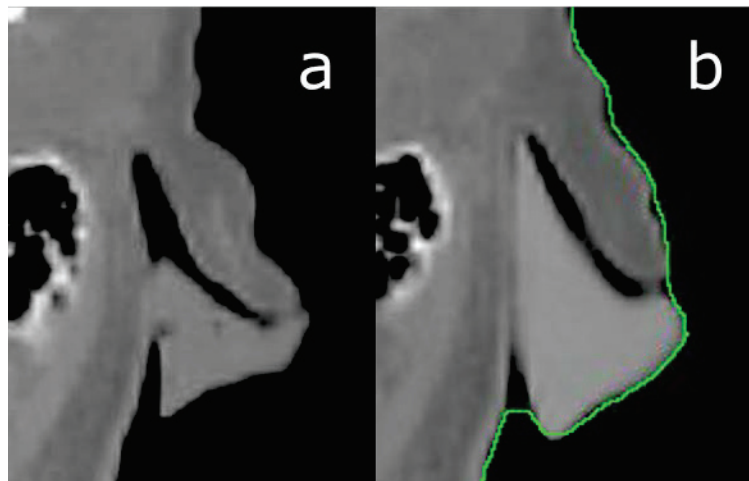The present work provides a Monte Carlo based algorithm that optimizes bolus design for conformation of the dose distribution to the PTV, addresses dose uniformity, and produces output that can be received by a 3D printer. In comparison to the pencil beam model approach, the eMC calculation used at each iteration will improve the accuracy of dose distribution in terms of the capability of handling the tissue heterogeneity and contour irregularity. The accuracy of eMC for calculation with PLA bolus has been demonstrated. The design algorithm itself does not require dose calculation and thus it would lend itself well to incorporation within a planning system; the output is provided in standard STL format, which is the standard for 3D printers, the cost of which has plummeted in recent years (i.e. about 2000 dollars for the printer and 50 dollars per roll of the material, while each roll may be used for up to 10 patients).

The ray line tracing method provides an initial approximation of bolus thickness adjustment at each iteration. However, without further modification it was found that the conformity is generally poor and PTV dose coverage requirements are not met. Accordingly, five regional modulation operators are applied, each solving a specific issue within the same iteration of bolus design. With these adjustments, existing hot spots can be reduced, better target coverage can be acquired and potential high doses can be avoided. Appropriate smoothing can be achieved with proper selection of smoothing factor (SF), thus controlling the balance between the dose conformity to the target volume and uniformity of dose distribution: while a larger SF brings about a smoother surface and naturally more homogeneity in the dose, a smaller SF leads to more sparing of the distal region. These operators perform on specific regions of interest that are

defined by specific criteria, which minimize the unwanted modification to the bolus shape and the corresponding side effect on dose distribution; this is in contrast with the approach of modification of the entire 'target volume less margin (TVLM)' as implemented by Low *et al*[25], which was a region on the bolus calculation plane corresponds to the entire target volume with a defined margin cropped. As a result, the modulation may cause unnecessary adjustment on bolus thickness to certain regions in TVLM, and consequently the nonessential changes to the dose distribution.

Both idealized and realistic target volumes for electron treatment cases demonstrate the efficacy of the technique. The simulation results of four phantom/patient studies show that the bolus design algorithm can address target volumes with variable shapes, location and proximity to organs at risk. The main advantage of MERT using optimized bolus over conventional electron therapy is a substantial reduction of the volume of normal tissues being irradiated. This will largely benefit patients who have organs at risk distal to PTVs, particular to those having irregular shape. On the other hand, for those cannot meet the demand of above 95% of PTV covered by 90% dose, patients can still profit from MERT in terms of better PTV coverage.

One concern of this methodology is the potential irregular bolus surface when the distal contour of PTV is extremely variable, which will inevitably result in local hot spots, and consequently, higher maximum dose. The employment of hot spot smoothing operator can alleviate this problem, but in some cases we found a tradeoff between dose uniformity and conformity.

The 3D printing approach allows accuracy in manufactured bolus at low cost and acceptable fitting to complex geometry. Compared to the standard process of defining a uniform bolus in the planning system, followed by application of generic bolus material,

the method allows for a high degree similarity between planned and actual bolus geometry. From the experience we gained from the real patient case, the printed bolus brings less pain to the patients since the bolus printing avoid the procedure of shaping the bolus material directly on patient/tumour. No additional information is required beyond the image set and the demands for both the staff and patient are reduced. In contrast to the manufacture using milling machine[26, 27], which may be completed outside hospital, a 3D printer can be easily installed in the cancer center, thus likely reducing cost and simplifying logistics of production.

Chapter 6 CONCLUSIONS AND FUTURE WORK

6.1 Summary of Work

In this work, we have investigated a practical approach, which is MERT employing optimized design and 3D printing of bolus. The method offers practical advantages in that neither patient nor staff must be present during the bolus fabrication process. In comparison to manual bolus fabrication, e.g., shaping of synthetic bolus sheets or moulding of wax or thermoplastics, the technique allows for optimization of bolus design with regard to dose conformity and homogeneity within the target volume. The algorithm takes advantage of the accuracy of electron Monte Carlo dose calculation to achieve accurate results, while successive iteration of the algorithm allows progressive improvement of dosimetric quality. Phantom and simulated patient studies demonstrate that the technique can achieve excellent dose conformity and acceptable dose homogeneity. The material for printing, PLA, can be appropriately taken into account in Eclipse TPS in term of dose calculation and the structure and shape of PLA may not be affected by the radiation, and thus is safe to be used in the radiation therapy.

6.2 Future Work

6.2.1 Clinical application of 3D-printed bolus

We expect to incorporate this methodology into our own clinical practice for a range of indications, including the optimization of bolus shape for electron therapy or the printing of uniform bolus for photon therapy. A specific planning guideline for MERT is in process, including patient selection, bolus optimization, use of printer software and transport of DICOM information, as well as generation of required output.

6.2.2 3D-printed bolus in small field electron therapy

Radiation therapy using small electron fields is challenging due to the loss of electronic equilibrium, which in turn affects both the lateral and longitudinal dose distributions. As discussed in section 2.5.6, an electron field is considered as small when the length of one side of the field decreases to below the R_p for the given energy. With the extra shielding for small field sizes, the PDD and the output factors are affected due to lack of lateral scatter, and thus degrades the uniformity of dose distribution: with decreasing field size, three distinct features can be observed: (1) decreased depth of dose maximum, (2) increased surface dose and (3) broader penumbrae (Figure 6.1a).

To study the feasibility of controlling dose homogeneity in such small field electron therapy, customized bolus was designed using the same concept discussed in section 3.3. As a preliminary investigation of this approach, BEAMnrc was used to simulate the linac electron beam line in accordance with the physical set-up of Varian 2100EX linear accelerator (Varian Medical, Inc., Palo Alto, CA) in the electron mode and DOSXYZnrc was employed for dose calculation.

The dose distribution with customized bolus added is shown in Figure 6.1b, where the thicker region of the bolus generates electron scatter and effectively compensates for the dose at edge of the field, thus increasing average dose within the target volume. However, this is achieved at a cost: the PDD curves (Figure 6.2) and the profiles (Figure 6.3) indicate a poorer uniformity. Given the potential utility of electron therapy, especially for facilities that do not offer superficial or orthovoltage photon therapy, this avenue may be worthy of further investigation, e.g., examination of improvement of dosimetry over a larger range of small field sizes and energies.

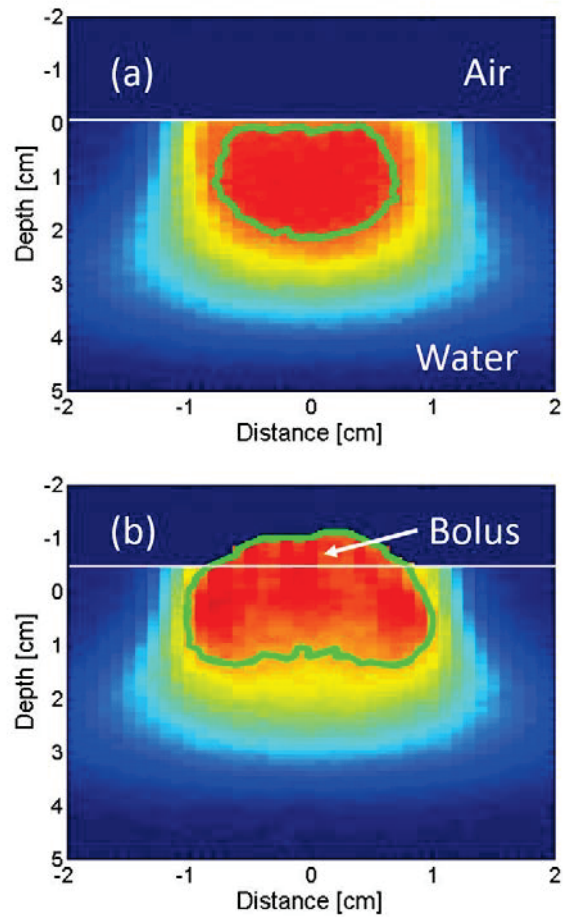Figure 6.1 Dose distribution of 2×2 cm^2 field size, 9 MeV electron beam without bolus (a) and with customized bolus (b). The green line contours the 90% isodose
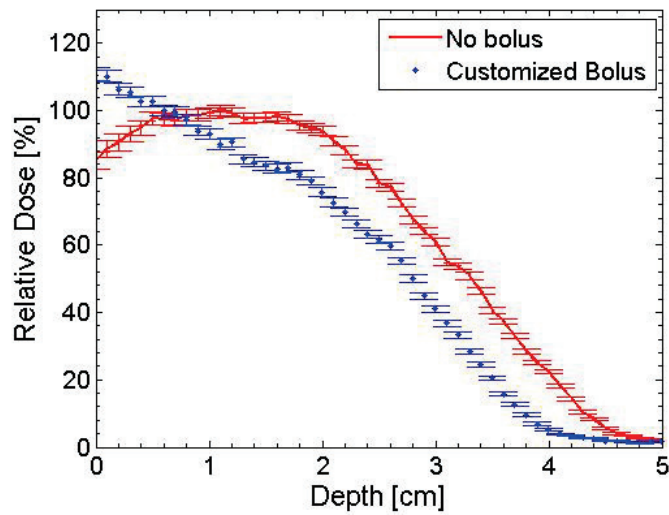

Figure 6.2 Central axis PDD curve of 2×2 cm^2 field size, 9 MeV electron beam without bolus and with customized bolus.
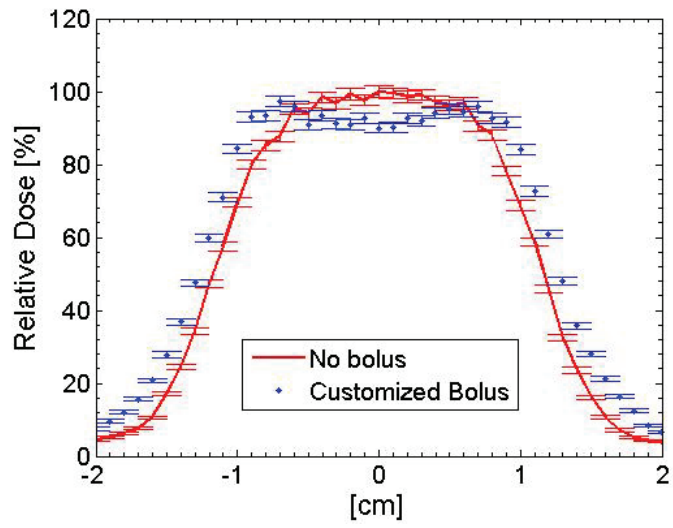
Figure 6.3 Profile at 1 cm depth of 2×2 cm^2 field size, 9 MeV electron beam without bolus and with customized bolus.

Bibliography

1. Canadian Cancer Society, Statistics Canada, Public Health Agency of Canada, "Canadian Cancer Statistics 2013," (2013).

2. G. Delaney, S. Jacob, C. Featherstone, and M. Barton, "The role of radiotherapy in cancer treatment: estimating optimal utilization from a review of evidence-based clinical guidelines," Cancer, 104(6), 1129-1137, (2005).

3. E.B. Podgorsak, *Radiation Oncology Physics: A Handbook for Teachers and Students* (International Atomic Energy Agency, 2005)

4. *Prescribing, Recording and Reporting Photon Beam Therapy,* Report 50, (ICRU, 1993).

5. *Prescribing, Recording and Reporting Photon Beam Therapy (Supplement to ICRU Report 50),* Report 62, (ICRU, 1999).

6. S. H. Lin, D. Latronico, T. Teslow, and G. K. Bajaj, "A Highly Reproducible Bolus Immobilization Technique for the Treatment of Scalp Malignancies", Med Dosim, 33, 30-35, (2008).

7. Hyödynmaa S, Gustafsson A and Brahme A, "Optimization of conformal electron beam therapy using energy- and fluence-modulated beams," Med. Phys. 23(5), 659-666, (1996).

8. Klein E, "Modulated electron beams using multi-segmented multileaf collimation," Radiother. Oncol. 48(3), 307-311, (1998).

9. Karlsson MG, Karlsson M and Ma CM, "Treatment head design for multileaf collimated high-energy electrons," Med. Phys. 26(10), 2161-67, (1999).

10. Blomquist M, Karlsson MG, Zackrisson B and Karlsson M, "Multileaf collimation of electrons--clinical effects on electron energy modulation and mixed beam therapy depending on treatment head design," Phys. Med. Biol. 47(7), 1013-1024, (2002).

11. Klein EE, Vicic M, Ma CM, Low DA and Drzymala RE, "Validation of calculations for electrons modulated with conventional photon multileaf collimators," Phys. Med. Biol. 53(5), 1183-1208, (2008).

12. Klein EE, Mamalui-Hunter M and Low DA, "Delivery of modulated electron beams with conventional photon multi-leaf collimators," Phys. Med. Biol. 54(2), 327–339, (2009).

13. Hogstrom KR, Almond PR, "Review of electron beam therapy physics," Phys. Med. Biol. 51(13), 455-489, (2006)

14. Jin L, Ma CM and Fan J, et al., "Dosimetric verification of modulated electron radiotherapy delivered using a photon multileaf collimator for intact breasts," Phys. Med. Biol. 53(21), 6009-6025 (2008).

15. du Plessis FC, Leal A, Stathakis S, Xiong W and Ma CM, "Characterization of megavoltage electron beams delivered through a photon multi-leaf collimator," Phys. Med. Biol. 51(8), 2113-2129, (2006).

16. Mu X, Olofsson L, Karlsson M, Sjögren R and Zackrisson B, "Can photon IMRT be improved by combination with mixed electron and photon techniques," Acta. Oncol. 43(8), 727-735, (2004).

17. Lee MC, Jiang SB and Ma CM, "Monte Carlo and experimental investigations of multileaf collimated electron beams for modulated electron radiation therapy," Med. Phys. 27(12), 2708–2718, (2000).

18. Hogstrom KR, Boyd RA, Antolak JA, Svatos MM, Faddegon BA and Rosenman JG, "Dosimetry of a prototype retractable eMLC for fixed-beam electron therapy," Med. Phys. 31(3), 443–462, (2004).

19. Ma CM, Pawlicki T, Lee MC et al., "Energy- and intensity-modulated electron beams for radiotherapy," Phys. Med. Biol. 45(8), 2293–2311, (2000).

20. Gauer T, Albers D, Cremers F, Harmansa R, Pellegrini R and Schmidt R, "Design of a computer-controlled multileaf collimator for advanced electron radiotherapy," Phys. Med. Biol. 51(23), 5987–6003, (2006).

21. Gauer T, Sokoll J, Cremers F, Harmansa R, Luzzara M and Schmidt R, "Characterization of an add-on multileaf collimator for electron beam therapy," Phys. Med. Biol. 53(4), 1071–1085, (2008).

22. Eldib AA, ElGohary MI, Fan J et al., "Dosimetric characteristics of an electron multileaf collimator for modulated electron radiation therapy," J Appl. Clin. Med. Phys. 11(2), 177-187, (2010).

23. Al-Yahya K, Hristov D, Verhaegen F and Seuntjens J, "Monte Carlo based modulated electron beam treatment planning using a few-leaf electron collimator—feasibility study," Phys. Med. Biol. 50(5), 847–857, (2005).

24. Connell T, Alexander A, Evans M and Seuntjens J, "An experimental feasibility study on the use of scattering foil free beams for modulated electron radiotherapy," Phys. Med. Biol. 57(11), 3259–3272, (2012).

25. Low DA, Starkschall G, Bujnowski SW, Wang LL and Hogstrom KR, "Electron bolus design for radiotherapy treatment planning: bolus design algorithms," Med. Phys. 19(1), 115-124, (1992).

26. Perkins GH, McNeese MD, Antolak JA, Buchholz TA, Strom EA and Hogstrom KR, "A custom three-dimensional electron bolus technique for optimization of postmastectomy irradiation," Int. J Radiat. Oncol. Biol. Phys. 51(4), 1142-1151, (2001).

27. Kudchadker RJ, Antolak JA, Morrison WH, Wong PF and Hogstrom KR, "Utilization of custom electron bolus in head and neck radiotherapy," J Appl. Clin. Med. Phys. 4(4), 321-333, (2003).

28. Low DA, Starkschall G, Sherman NE, Bujnowski SW, Ewton JR and Hogstrom KR, "Computer-aided design and fabrication of an electron bolus for treatment of the paraspinal muscles," Int. J Radiat. Oncol. Biol. Phys. 33(5), 1127-1138, (1995).

29. Kirova YM, Campana F, Fournier-Bidoz N et al., "Postmastectomy electron beam chest wall irradiation in women with breast cancer: a clinical step toward conformal electron therapy," Int. J Radiat. Onco. Biol. Phys. 69(4), 1139-1144, (2007).

30. Kim MM, Kudchadker RJ, Kanke JE, Zhang S and Perkins GH, "Bolus electron conformal therapy for the treatment of recurrent inflammatory breast cancer: a case report," Med. Dosim. 37(2), 208-213, (2012).

31. F. H. Attix, *Introduction to radiological physics and radiation dosimetry* (Wiley, 1986).

32. Robley Dunglison Evans, *The atomic nucleus* (McGraw-Hill, 1955)

33. National Institute of Standards and Technology, "Stopping power and ranges for electrons," (2014).

34. *Radiation dosimetry: Electron beams with energies between 1 and 50 MeV,* ICRU. Report 35, (ICRU, 1984).

35. E.B. Podgorsak, *Radiation Physics for Medical Physicist*, (Springer, 2006).

36. Gerbi BJ, Antolak JA, Deibel FC, et al., "Recommendations for clinical electron beam dosimetry: supplement to the recommendations of Task Group 25," Med. Phys. 36(7), 3239-3279 (2009).

37. Almond PR, Biggs PJ, Coursey BM, et al., "AAPM's TG-51 protocol for clinical reference dosimetry of high-energy photon and electron beams," Med. Phys. 26(9), 1847-70, (1999).

38. Gerbi BJ, Antolak JA, Deibel FC, et al., "Recommendations for clinical electron beam dosimetry: supplement to the recommendations of Task Group 25," Med. Phys. 36(7), 3239-79, (2009).

39. Almond PR, Xu Z, Li H, Park HC, "The calibration and use of plane-parallel ionization chambers for dosimetry of electron beams," Med. Phys. 22(8), 1307-1314, (1995).

40. AAPM report NO.87, "Diode in vivo dosimetry for patients receiving external beam radiation therapy", Report of Task Group 62 of the Radiation Therapy Committee, (2005).

41. L. Eyges, "Multiple scattering with energy loss," Phys. Rev. 74, 1534-1535, (1948)

42. Faiz Khan, *The Physics of Radiation Therapy*, third edition, (Lippincott Williams & Wilkins, 2003).

43. Hogstrom K R, Mills M D and Almond P R, "Electron beam dose calculations" Phys. Med. Biol. 26, 445–459 (1981).

116

44. Brahme A, "Current algorithms for computed electron beam dose planning," Radiother. Oncol. 3, 347–362, (1985).

45. R. L. Ford and W. R. Nelson, "The EGS Code System (Version 3)," SLAC Rep. 210 Stanford University, Stanford, California, (1978)

46. M. J. Berger, "Monte Carlo calculation of the penetration and diffusion of fast charged particles," Methods Comput. Phys. 1, 135-215 (1963)

47. Neuenschwander H, Mackie TR and Reckwerdt PJ, "MMC--a high-performance Monte Carlo code for electron beam treatment planning," Phys. Med. Biol. 40(4), 543-574, (1995).

48. Ding GX, Duggan DM, Coffey CW, Shokrani P and Cygler JE, "First macro Monte Carlo based commercial dose calculation module for electron beam treatment planning–new issues for clinical consideration," Phys. Med. Biol. 51(11), 2781–2799, (2006).

49. Popple RA, Weinber R and Antolak JA, et al., "Comprehensive evaluation of a commercial macro Monte Carlo electron dose calculation implementation using a standard verification data set," Med. Phys. 33(6), 1540–1551, (2006).

50. Xu Z, Walsh SE, Telivala TP, Meek AG and Yang G, "Evaluation of the eclipse electron Monte Carlo dose calculation for small fields," J Appl. Clin. Med. Phys. 10(3), 2834, (2009).

51. Fearon T, Xie H, Cheng JY, Ning H, Zhuge Y and Miller RW, "Patient-specific CT dosimetry calculation: a feasibility study," J Appl. Clin. Med. Phys. 12(4), 3589, (2011).

52. Winslow M, Xu XG and Yazici B, "Development of a simulator for radiographic image optimization," Comput Methods Programs Biomed. 78(3), 179-190, (2005).

53. Chetty IJ, Curran B, Cygler JE, et al., "Report of the AAPM Task Group No. 105: Issues associated with clinical implementation of Monte Carlo-based photon and electron external beam treatment planning," Med Phys. 34(12), 4818-4853, (2007).

54. Teke T, Bergman AM, Kwa W, Gill B, Duzenli C and Popescu IA, "Monte Carlo based, patient-specific RapidArc QA using Linac log files," Med. Phys. 37(1), 116-123, (2010).

55. Rogers DW, Faddegon BA, Ding GX, Ma CM, We J, Mackie TR, "BEAM: a Monte Carlo code to simulate radiotherapy treatment units," Med Phys. 22(5), 503-524, (1995).

56. Kawrakow I, "Accurate condensed history Monte Carlo simulation of electron transport. I. EGSnrc, the new EGS4 version," Med Phys. 27(3), 485-498, (2000).

57. B. R. B. Walters, Kawrakow, D. W. O. Rogers, "History by history statistical estimators in the BEAM code system", Med. Phys. 29 (12), 2745-2752, (2002).

58. Tomas Moller and Ben Trumbore, "Fast, minimum storage ray-triangle intersection," Journal of Graphic Tools, 2(1), 21-28, (1997).

59. Holt JG, Mohan R, Caley R, et al. Memorial electron beam AET treatment planning system. In: Orton CG, Bagne F, eds. *Practical aspects of electron beam treatment planning*, NY, Institute of Physics, 1978.

60. Low DA and Hogstrom KR, "Determination of the relative linear collision stopping power and linear scattering power of electron bolus material," Phys. Med. Biol, 39(6), 1063-1068, (1994).

61. Low DA, Harms WB, Mutic S, Purdy JA. "A technique for the quantitative evaluation of dose distributions," Med. Phys. 25(5), 656-661 (1998).